

**MODIFICATION OF A COMPUTATIONAL FLUID
DYNAMICS MODEL (ANSYS-FLUENT) FOR THE
PURPOSE OF RIVER FLOW AND SEDIMENT
TRANSPORT MODELING**

**A Thesis Submitted to
the Graduate School of Engineering and Sciences of
İzmir Institute of Technology
in Partial Fulfillment of the Requirements for the Degree of
MASTER OF SCIENCE
in Civil Engineering**

**by
Hüseyin Burak EKMEKÇİ**

July, 2015

İZMİR

We approve the thesis of **Hüseyin Burak EKMEKÇİ**

Examining Committee Members:

Assoc. Prof. Dr. Şebnem ELÇİ

Department of Civil Engineering, İzmir Institute of Technology

Prof. Dr. Gökmen TAYFUR

Department of Civil Engineering, İzmir Institute of Technology

Prof. Dr. Sevinç ÖZKUL

Department of Civil Engineering, Dokuz Eylül University

23 July 2015

Assoc. Prof. Dr. Şebnem ELÇİ

Supervisor, Department of Civil Engineering

İzmir Institute of Technology

Prof. Dr. Gökmen TAYFUR

Head of the Department of Civil Engineering

Prof. Dr. Bilge KARAÇALI

Dean of the Graduate School of
Engineering and Sciences

ACKNOWLEDGEMENTS

Prima facie, I would like to thank to my advisor Assoc. Prof. Dr. Şebnem ELÇİ to provide all necessary facilities for the thesis. She always shares her valuable time when there is a need of me. I am really grateful for her support, encouragement and constant guidance. Also, I would like to indicate that I appreciate Prof. Dr. Gökmen TAYFUR and Prof. Dr. Sevinç ÖZKUL for agreeing to be on my thesis committee.

This study would not be possible without the support of Dr. Aslı BOR. Her help was about not only field measurement but also numerical modeling at many points. Every time that I need help, she never refused me and gave her patience.

Thanks research assistant at İzmir Institute of Technology Department of Mechanical Engineering for their help on using of Fluent Solver.

I would like to extend a note of thanks to beautiful-good person Muradiye DAĞCI. Thanks to her endless support and help in any case.

Also I would like to thank members of my family, my father Osman EKMEKÇİ, my mother Şengül EKMEKÇİ and my sister Ece EKMEKÇİ for all their encouragement. They are always with me in sunshine and in storm.

ABSTRACT

MODIFICATION OF A COMPUTATIONAL FLUID DYNAMICS MODEL (ANSYS-FLUENT) FOR THE PURPOSE OF RIVER FLOW AND SEDIMENT TRANSPORT MODELING

Precise estimation of the sediment transport and settling velocity of particle in turbulent flows is required for many engineering applications including modeling of the transport of suspended sediments and the transport of particle pollutants. This study presents an approach for modification of an existing CFD Model for sediment transport in turbulent flow based on field measurements.

In the first part, synchronized 3-D velocity and temperature time series were monitored at Büyük Menderes River in Turkey where the data were utilized to characterize the turbulence characteristics and model particle – fluid interaction. Sieve and hydrometer analysis were obtained from earlier studies to understand and modify sediment transport under different conditions via ANSYS Fluent programme.

The second part of the study involved numerical modeling of hydrodynamics via 3D CFD model in the selected portion of a river body through use of field measurements conducted at the study site. The $k-\omega$ turbulence model found to be the best suited when such flow around a structure as piers or flow through a water intake is considered. Effect of particle size, concentration and modeling approach for particle motion are also investigated and Rossin Rammler Logarithmic Distribution and multiphase modeling approach was the most appropriate methods. This study involved development of an approach to modify drag force on sediment particles using turbulence characteristics in the Fluent solver as well.

ÖZET

BİR HESAPLAMALI AKIŞKANLAR DİNAMIĞI MODELİNİN (ANSYS-FLUENT) NEHİR AKIM VE SEDİMENT TAŞINIMI MODELLENMESİNDE KULLANILMAK ÜZERE DEĞİŞTİRİLMESİ

Türbülanslı akım içerisinde bulunan parçacık çökme hızı ve sediment taşınımının hassas tahmini askıdaki ve kirletici parçacık taşınımını da içerisinde barındıran bir çok mühendislik uygulaması için gereklidir. Bu çalışma, ölçümlerden elde edilen arazi verilerinden faylanarak, varolan bir CFD Modeli'nde, türbülanslı akım içerisindeki sediment taşınımı üzerinde değişiklik yaklaşımı sunmaktadır.

Çalışmanın ilk bölümünde, türbülansı karakterize edebilme ve parçacık - akışkan etkileşimini modelleyebilmek için Büyük Menderes Nehri'nde eş zamanlı 3 boyutlu hız ve sıcaklık zaman serileri ölçülmüştür. ANSYS Fluent programı kullanılarak farklı şartlar altındaki sediment taşınımını düzenlemek ve anlamak amacı ile önceki çalışmalardan elde edilen elek ve hidrometre analizlerine ulaşılmıştır.

Çalışmanın ikinci bölümünde, CFD model yardımı ile arazi çalışmasının yapıldığı belli bir nehir bölgesinin sayısal hidrodinamik modellemesi yapılmıştır. $K-\omega$ türbülans modelinin, su alma yapıları ve köprü ayakları gibi bölgelerde en uygun sonucu verdiği görülmüştür. Aynı zamanda parçacık boyutu, konsantrasyonu ve modellemesi de bu çalışmada incelenmiştir ve Rossin Rammler Logarithmic Dağılımı (RRLD)'nin çok fazlı parçacık tanımlamalarında en uygun sonucu verdiği görülmüştür. Bu çalışma aynı zamanda, Fluent çözücüsü ile türbülans karakteristiklerinden faydalanarak, sediment parçacıkları üzerindeki sürüklenme kuvvetini düzenleme yaklaşımının geliştirilmesini içermektedir.

TABLE OF CONTENTS

LIST OF FIGURES	ix
LIST OF TABLES	xiv
CHAPTER 1. INTRODUCTION	1
CHAPTER 2. LITERATURE REVIEW	4
CHAPTER 3. METHODOLOGY	8
3.1. Available Turbulence Models in Fluent	8
3.1.1. Fluent in General	8
3.1.2. Turbulence in General	10
3.1.3. Turbulence Modeling in General.....	11
3.1.3.1. Classification of Turbulent Models	13
3.1.3.1.1. Algebraic (Zero-Equation) Models.....	13
3.1.3.1.2. One-Equation Models	13
3.1.3.1.2.1. Spalart–Allmaras Turbulence Model.....	14
3.1.3.1.3. Two-Equation Models	15
3.1.3.1.3.1. Standard k- ϵ Model.....	16
3.1.3.1.3.2. Standard (Wilcox) k- ω Model	17
3.1.3.1.3.3. Shear Stress Transport (SST).....	18
3.1.3.1.4. Second-Order Closure Models.....	20
3.1.3.1.4.1. Reynolds Stress Equation Model	21
3.1.3.1.4.1.1. Advantages and Disadvantages of RMS	22
3.1.3.1.4.2. Large Eddy Simulation (LES)	22
3.1.4. Available Turbulent Models in Fluent	24
3.2. Multiphase Particle Modeling in Fluent	25
3.2.1. Euler-Lagrange Approach	26
3.2.1.1. Discrete Element Model	26
3.2.2. Euler-Euler Approach.....	26

3.2.2.1. VOF Model	27
3.2.2.2. Mixture Model	27
3.2.2.3. Eulerian Model	28
3.3. Models Utilized in Modeling of Flow and Sediment Transport in This Study.....	28
CHAPTER 4. MONITORING FIELD DATA	30
4.1. Field Data Monitoring	30
4.1.1. Study Site.....	30
4.1.2. Instrumentation.....	31
4.1.3. Simultaneous Deployment of Acoustic Doppler Current Profiler and Thermistor Chain	33
4.2. Analysis of Field Data	35
CHAPTER 5. CFD MODELING OF THE FLOW	40
5.1. Computational Domain.....	40
5.1.1. Generating Geometry	40
5.1.2. Generating Mesh.....	44
5.1.2.1. Mesh application on B. Menderes River geometry	47
5.2. Initial and Boundary Conditions.....	51
5.2.1. Simulation of a Simple Water Column without Sediment Layer in Order to Analyze Different Turbulent Models.....	51
5.2.2. Simulation of Flow in B. Menderes River without Sediment Layer in Order To Analyze Different Turbulent Models	58
5.2.2.1. Results of Constant Flow Discharge.....	58
5.2.2.2. Results of Hydrograph	65
5.2.3. Modeling of Particle Motion in a Simplified Model Domain	70
5.2.3.1. Particle Motions Considering Uniform Diameter Distribution k- ϵ Turbulence Model with Standard Wall Function vs k- ω Turbulence Model with Standard Wall Function)	71

5.2.3.2. Particle Motions Considering Eulerian Multiphase DPM Injection with Rossin Rammler Logarithmic distribution versus Eulerian Multiphase DPM Injection with Uniform Diameter Having 0,003 mm	79
5.2.3.3. DPM Injection with Rossin Rammler Logarithmic Distribution Using Eulerian Multiphase versus Single Phase	81
CHAPTER 6. MODIFICATION OF RIVER FLOW AND SEDIMENT TRANSPORT MODELING IN CFD.....	84
6.1. How to Compile a User Define Function Consisting Of Modified Drag Law Codes	84
6.2. Comparison of Sediments Motions Simulated By Eulerian DPM Method via Modified Drag Law Versus via Non-Modified Drag Law	87
CHAPTER 7. DISCUSSION AND CONCLUSIONS	92
REFERENCES	95
APPENDICES	
APPENDIX A. UDF (HYDROGRAPH)	98
APPENDIX B. UDF (DEFINED DRAG FORCE)	100

LIST OF FIGURES

<u>Figure</u>	<u>Page</u>
Figure 1.1. A view from B. Menderes River	2
Figure 3.1. A view from a “solution setup” within Fluent.	8
Figure 3.2. A view from “pause command” within Fluent.	9
Figure 3.3. A view from “Post Processing” within Fluent.	9
Figure 3.4. Flow characteristics respect to Reynolds Number [12].....	10
Figure 3.5. Energy cascade [12]	11
Figure 3.6. Instantaneous velocity contours (left one) and time-averaged velocity (right one) [12]	12
Figure 4.1. B. Menderes Bridge (Old Aydın Bridge) and B. Menderes River	30
Figure 4.2. View of Ruskin Programme	31
Figure 4.3. Screenshot of ViewADP ADCP file information screen	33
Figure 4.4. View of ADCP	33
Figure 4.5. Simultaneous measurement of temperature and velocity	34
Figure 4.6. Cell size selected during the measurement.....	34
Figure 4.7. A view from the measurements.....	35
Figure 4.8. Observed water temperature along the water column	36
Figure 4.9. Monitored flow velocities during the measurement campaign (above) and instantaneous flow velocity while measurement (below)	36
Figure 4.10. 1 minute time averaged 3D flow velocities (u,v,w) measured by the ADCP during the field campaign	37
Figure 4.11. Variation of the time averaged flow velocity with respect to depth.	37
Figure 4.12. Variation of the time averaged flow velocity with respect to depth.	38
Figure 4.13. Comparison between measured settling velocity via ADCP and calculated turbulence characteristics	39
Figure 5.1. Google Earth view of simulation area	41
Figure 5.2. Bottom surface of B. Menderes River in ANSYS before merging	41
Figure 5.3. 3D body of B. Menderes River in ANSYS	42
Figure 5.4. Generating of sediment body	42
Figure 5.5. Generating of bridge piers	43
Figure 5.6. Merging of bottom surface in main domain	43

Figure 5.7. Named selection of main geometry in geometry window.....	44
Figure 5.8. Different 3D mesh types [14].....	45
Figure 5.9. Quality scale of mesh [29].....	45
Figure 5.10. Prism / Hex Element shapes (left one) and a sweepable body (right one). 46	
Figure 5.11. Source and target faces for sweep method in main geometry	46
Figure 5.12. Automatic method for sediment layer	47
Figure 5.13. Named Selection for main geometry	48
Figure 5.14. B. Menderes river domain in ANSYS.....	48
Figure 5.15. Water and sediment bodies.....	49
Figure 5.16. Mesh quality on main domain	49
Figure 5.17. Sectional View of meshing.....	50
Figure 5.18. Tahtalı model domain utilized in ANSYS programme	52
Figure 5.19. A Google Earth view from the Tahtalı model domain selected.....	53
Figure 5.20. Comparison of velocities simulated using different turbulence models at the intake (at the left side) and 1 m far away from the intake (at the right side).....	54
Figure 5.21. Velocities at different distances from the intake (Reynolds turbulence model).....	54
Figure 5.22. Velocities at different distances from the intake (k- ϵ and k- ω turbulence models).	55
Figure 5.23. TKE/u ² values for k- ϵ , k- ω and Reynolds turbulence models.....	56
Figure 5.24. Difference of nondimensionalized turbulent kinetic energy values simulated by k- ϵ and Reynolds models (standard wall function) at the intake.....	57
Figure 5.25. Difference of nondimensionalized turbulent kinetic energy values simulated by k- ϵ (standard wall function) and k- ω turbulence models at the intake.....	57
Figure 5.26. Investigated line and point on main domain	59
Figure 5.27. Longitudinal velocities on investigated line for both k- ϵ and k- ω turbulence models.	59
Figure 5.28. Lateral velocities on investigated line for both k- ϵ and k- ω turbulence models.	60

Figure 5.29. Depth-averaged velocities on investigated line for both k- ϵ and k- ω turbulence models.	60
Figure 5.30. Velocity magnitude at investigated point for both k- ϵ and k- ω turbulence models.	61
Figure 5.31. Longitudinal velocity contours on investigated planes for both k- ϵ (above) and k- ω (below) turbulence models.	62
Figure 5.32. Volume rendering of Longitudinal velocities for both k- ϵ (left) and k- ω (right) turbulence models.....	62
Figure 5.33. TKE contours on investigated planes for both k- ϵ (above) and k- ω (below) turbulence models.	63
Figure 5.34. Volume rendering of TKE for both k- ϵ (left) and k- ω (right) turbulence models	64
Figure 5.35. A view of turbulence effect of piers on B. Menderes River.....	64
Figure 5.36. Longitudinal velocities on investigated line for both k- ϵ and k- ω turbulence models (hydrograph)	65
Figure 5.37. Lateral velocities on investigated line for both k- ϵ and k- ω turbulence models (hydrograph)	66
Figure 5.38. Depth-averaged velocities on investigated line for both k- ϵ and k- ω turbulence models (hydrograph)	66
Figure 5.39. Velocity magnitude at investigated point for both k- ϵ and k- ω turbulence models (hydrograph)	67
Figure 5.40. TKE contours on investigated planes for both k- ϵ (above) and k- ω (below) turbulence models.	68
Figure 5.41. Volume rendering of TKE for both k- ϵ (left) and k- ω (right) turbulence models.	68
Figure 5.42. Volume rendering of TKE for both k- ϵ (left) and k- ω (right) turbulence models.	69
Figure 5.43. Volume rendering of Longitudinal velocities for both k- ϵ (left) and k- ω (right) turbulence models.....	69
Figure 5.44. Longitudinal velocity contours on investigated planes for both k- ϵ (above) and k- ω (below) turbulence models.	70
Figure 5.45. Investigated plane in the simplified domain.....	72
Figure 5.46. Particle motion (median diameter: 0,003 mm; total mass 22,62 kg)	72

Figure 5.47. Particle motion (median diameter : 0,003 mm ; total mass 11,31 kg)	73
Figure 5.48. Area weighted settling velocity simulated using k- ϵ turbulence model at the selected plane given in Figure 5.45.....	74
Figure 5.49. Particle settling time simulated using k- ϵ turbulence model at the all body	75
Figure 5.50. Area weighted settling velocity simulated using k- ω turbulence model at the selected plane given in Figure 5.45.....	75
Figure 5.51. Particle settling time simulated using k- ω turbulence model at the all body	76
Figure 5.52. Total particle mass settled down respect to time for both k- ϵ and k- ω turbulence models	76
Figure 5.53. Total particle mass accumulated on bottom surface respect to time for both k- ϵ and k- ω turbulence models	77
Figure 5.54. Area weighted settling velocity (d=0.003 mm) simulated using k- ω turbulence model at the selected plane given in Figure 5.45 with respect to different concentrations	78
Figure 5.55. Particle settling time (d=0.003 mm) simulated using k- ω turbulence model at the selected plane given in Figure 5.45 with respect to different concentration	78
Figure 5.56. Comparison of volume renderings plots of uniform (d=0.003 mm) and RRLD applied sediment distributions	80
Figure 5.57. Comparison of area-weighted settling velocities for uniform (d=0,003 mm) and RRLD distributions at the selected plane given in Figure 5.45	80
Figure 5.58. Comparison of sedimentation times for uniform (d=0,003 mm) and RRLD distributions at the selected plane given in Figure 5.45	81
Figure 5.59. Comparison of particle mass concentrations for RRLD sediment considering single and multiphase cases	82
Figure 5.60. Comparison area-weighted settling velocities for RRLD sediment distributions considering single and multiphase cases at the investigated plane.	83
Figure 5.61. Comparison sedimentation times between RRLD with single and multiphase.	83
Figure 6.1. SDK Comment prompt page and solution files.....	85

Figure 6.2. Fluent Launcher window	85
Figure 6.3. Main Discrete Phase Model window.....	86
Figure 6.4. Particle mass concentrations simulated using the original drag forces	88
Figure 6.5. Particle mass concentrations simulated using the modified drag forces	89
Figure 6.6. Comparison of sedimentation times simulated using the original and modified drag forces.....	89
Figure 6.7. Investigated planes for Figure 6.8 and Figure 6.9	90
Figure 6.8. Settling Velocities of injected particles on different planes (nonmodified simulation).	90
Figure 6.9. Settling Velocities of injected particles on different planes (modified simulation).	91

LIST OF TABLES

<u>Figure</u>	<u>Page</u>
Table 3.1. Turbulence models in Fluent solver	25
Table 5.1. Geometry and mesh properties for the main domain.....	51

CHAPTER 1

INTRODUCTION

It is known that turbulence is a very important and complicated situation in nature. In general, this complicated situation is produced by mean shear due to changes in kinetic energy generated by winds or tides and by unstable stratification due to changes in potential energy. Owing to turbulence, settling velocity that is the terminal velocity of particle (or floc) settling down when the fluid drag force equal to downward gravity force [1, 2] is important as well. It is possible to deduce about water quality and flooding by understanding relation between turbulence mechanism and sediment transport because sediment which is directly affected by turbulence is a physical pollutant for water and can lead to increasing flooding. Penetration of sunlight into the water column is limited by high level of turbidity, therefore it causes limiting or prohibiting growth of algae and rooted aquatic plants. On the other hand, high levels of sedimentation in rivers lead to physical disruption of the hydraulic characteristics of the channel. This can cause reduction in depth of the channel, and can lead to increased flooding because of reductions in capacity of the river channel. Figure 1.1 was taken from B. Menderes River and shows the turbidity in water. As can be inferred from the Figure 1.1, the river bed is invisible due to turbidity.

In nature, it is possible to say that water almost always flow turbulent. However Stokes' Settling Velocity is used for laminar flow. The main goal of this thesis was to investigate ways to modify settling velocity in a numerical model (Fluent) via "user defined function" to estimate the settling velocity of particles in turbulent flow more accurately. For application, part of B. Menderes River located in Aydın was selected. Field data were collected and main simulation was created for a small part (180 m length) of B. Menderes River located near Old Aydın Bridge. Piers of old Aydın Bridge generated turbulence which fit to our goals in this study.

The complexities of the turbulent flow in a river suggest the use of numerical modeling approaches to provide and infer accuracy of modified settling velocity and applicability of different turbulent models in nature. Fluent which is a solver of ANSYS programme was used for this thesis. It is possible to create a simulation consisting of

3-D water body with suspended sediment and bed sediment load. However, it can be time consuming for large bodies. In this thesis, total length of simulated body was 180 m, therefore it was important to get results in sufficient time with acceptable mesh quality and elements numbers.



Figure 1.1. A view from B. Menderes River

In the literature, research on understanding of turbulence simulations and effects of different particle concentration in water include numerical, analytical, and field studies (mainly in rivers or reservoirs). In these studies, not only effects of particle character on settling velocity in different turbulent conditions were analyzed, but also Lagrangian approach with discrete phase method (DPM) in different flow conditions was investigated. However, Stokes' settling velocity which is defined for laminar flow and the modified versions of this equation which relate settling velocity to particle diameter were used in these studies, although turbulent flow was analyzed.

This thesis consists of six chapters. Chapter 1 aims to present a brief introductory background to the research subjects. Previous relevant studies regarding numerical modeling of reservoirs are reviewed in Chapter 2. In Chapter 3, not only available turbulence models in Fluent are investigated but also methods of different simulations conditions are described. Data obtained from the field measurements were presented as well. In Chapter 5, simulation of flow and sediment transport for different flow conditions via Fluent Solver are discussed. Modification of settling velocity in

Fluent solver via user defined function is described in Chapter 6. The main results and the conclusions of the study are summarized in Chapter 7.

CHAPTER 2

LITERATURE REVIEW

The phenomenon of sediment transport is quite complicated and a sound understanding is necessary for almost all topics related to river engineering, design of water intakes and sedimentation problems in reservoirs and in irrigation canal systems. Sediment settling velocity is obtained from the balance of gravitational, buoyancy and drag forces theoretically and Stokes' law is considered in many studies regardless of its assumptions. Although formulations considered drag coefficient as a function of Reynolds number, the settling velocity was related to sediment diameter alone in many studies.

Turbulence in a sediment laden flow affects the settling velocity of the particles in different ways. Fluctuations in the flow cause varying external forces on sediment particles. They do not constitute a stable settling due to rotating eddies in turbulent flow. Also fluctuating flow may result in the acceleration or deceleration of the sediment particles settling. The separation point on the surface of the particle would also be affected by turbulence.

Although one can find studies related characterizing of turbulent characteristics in the literature, there are only a few studies investigating the effect of turbulence on sediment transport and settling velocity. The settling of activated sludge flocs under turbulent conditions were studied experimentally in this study. The measurements of settling velocities of particles were achieved by the Particle Image Velocimeter (PIV) technique. Results showed that higher turbulence intensity led to lower settling velocity. Vesilind formula that is an empirical formula and describes relation between zone settling velocity and sludge concentration was modified, to account for turbulence intensity, particle diameter and sludge concentration to obtain settling velocity through experiments. It was also observed that under the same turbulence intensity, particle that has large diameter tends to have higher settling velocity, but this tendency decreases when turbulence intensity gets higher. It was concluded that the presented modified Vesilind formulation can be used to estimate the minimal turbulence needed to keep

flocs in suspension so that more precisely predict flow field in a reactor can be predicted [3].

In another study, the relations between the coherent structure of the flow and particle concentration were examined. The magnitude of turbulence stresses were related to particle size and it was found that turbulence is enhanced in the case of larger particles than a critical diameter correlated with the Kolmogoroff microscale and it is suppressed when particle diameter is less than it. Simultaneous measurements of fluid velocity and particle velocity and local concentration by the discriminator combination of particle image Velocimeter (PIV) and particle tracking Velocimeter (PTV) in sediment-laden open-channel flows led investigation of effects of ejection and sweep motions. It was observed that the strength of the ejections and sweeps changed by suspended sediment. Ejection motion enhanced the sediment concentration by 20-40% and sweep motion decreased it about 10-30% [4].

The effects of turbulence and suspended sediment concentration on settling velocity of cohesive sediments were investigated via laboratory experiments. Acoustic Doppler Velocimeter was used in the experiments. The shear stress which was linked to turbulent kinetic energy was artificially changed and when shear stress was higher than approximately 0,14 Pa, they observed that the floc size and the settling velocity decreased. This was attributed to the fact that turbulence could produce more frequent collisions of suspended particles which result in forming larger flocs. It was stated that ADV is a vital tool and can be used not only to measure instantaneous 3-D flow velocities but also to measure the suspended sediment concentration and w_s in turbulence-dominant environments without breaking up flocs and seriously disturbing ambient flow [5].

In another work, Fluent model was used to investigate the interaction between the particles and fluid for the design of trap shape in a sewer. Lagrangian approach was used and the RNG k- ϵ model was applied for turbulence closure. As boundary conditions, a velocity-inlet condition for inlet and pressure outlet was considered for outlet boundary condition. For the discrete phase model, velocity inlet and pressure outlet was prescribed as an 'escape' meaning that the particle is reported as having escaped when it encounters the boundary in question, 'trap' (for trap base) and 'reflect' (for channel and trap walls) were used for DPM boundary conditions. Results of 2D simulation were compared with the 3D simulation and it was stated that absence of

lateral flow led lack of generation of eddies –that creates turbulence- via presence of walls and edges, and resulted in higher TKE. It was concluded that 3D simulation was required for the accurate prediction of the interaction between the particles and the flow structure [6].

In another study, Fluent model was again used to model the flow structure in a sedimentation tank and to investigate the interaction between the particles and fluid. A series of numerical simulations of flow in a sedimentation tank were performed where the effect of particle size and volume fraction on the flow properties were investigated. Lagrangian approach was utilized and the RNG k- ϵ model was applied for turbulence closure. The Lagrange method was preferred since the equation that describes the particle motion is solved for each particle moving through the field of random fluid eddies. As boundary conditions, velocity-inlet condition was considered for inlet and pressure outlet was considered for outlet boundary condition. For the discrete phase model, velocity inlet and pressure outlet was prescribed as an “escape” condition. The results of this study showed that in general influence of particles on fluid phase was higher when particle size and volume fraction increased [7].

A new boundary condition was obtained in order to simulate sedimentation processes better in this investigation. Fluent solver was used to simulate Djargo Reinhardt basin. Due to its large body, steady state was simulated instead of transient state. Inlet condition was chosen as "velocity inlet" and outlet condition was chosen as "pressure outlet". k- ω turbulent model was used for turbulence condition. Eulerian-Lagrangian method was used as well. Volume of Fluid was chosen as multiphase method and Discrete Phase Method (DPM) was chosen to inject particles. 20000 particles were injected by DPM and upper limit of convergence criterion was 10^{-4} . The main purpose of this study was to define bed boundary condition. Although, the escape and reflect conditions were chosen for particles on inlet and side walls, combination of trap and reflect with developed “user defined function” (UDF) was used for bed of basin. A threshold Turbulent Kinetic Energy (TKE) was calculated for bed boundary condition and added it to Fluent via UDF. If the local bed TKE was less than the threshold, the particle would settle at the bottom; if not, the particles reflected back into the water column. Results showed that there were some differences between simulation and experimental results. Geometrical differences between field and simulation could cause it. In this study bottom shape was hard to simulate. Owing to hardness of large

bodies' simulations, steady state solution was used instead of transient solution. This also could cause these differences. To sum up, in this study, a threshold TKE was calculated and sedimentation process was simulated. It was seen that, it is possible to change bed boundary condition and particle motions on bottom [8].

In another study, sweep and ejection motion were examined to understand genesis of turbulence, and using the logarithmic law of wall and Reynolds stress distribution curve with an acceptable 8% difference bed skin friction velocity was calculated. In sediment laden rectangular water channel, Acoustic Doppler Velocimeter profiler was used and median diameter for particle was chosen as 15 mm. Reynolds number was 1×10^5 which means turbulent flow and discharge was 251,4 lt/s. Clauser method, applicable near the bottom [9], was used to calculate friction velocity and it was found as 4,22 cm/s. By using Reynolds stress distribution it was found as 3,86 cm/s. When Reynolds stress friction velocity (u^*_{RS}) and logarithmic friction velocity (u^*_{LOG}) were compared there was a little differences (8%) and it was acceptable. The first result showed that Reynolds stress that is computed via instantaneous velocities measured by ADV is important to calculate friction velocity and there is a strong relation between Clauser Method and the other result showed that the suspended particles are lifted up and Reynolds stress fluctuations become large positive values in ejections, and large negative ones in sweeps due to ejection motions. It is easy to say that after these experimental results, there is a strong relation between ejection / sweep motions, turbulence structures and Reynolds shear stress. From this study, it was inferred that for reformulation of settling velocity in turbulent flow Reynolds shear stress must be considered [10].

CHAPTER 3

METHODOLOGY

3.1. Available Turbulence Models in Fluent

3.1.1. Fluent in General

Fluent is a solver in ANSYS programme related to fluid dynamics. It has a lot of features such as modeling flow, turbulence, heat transfer and reactions for industrial applications (Figure 3.1).

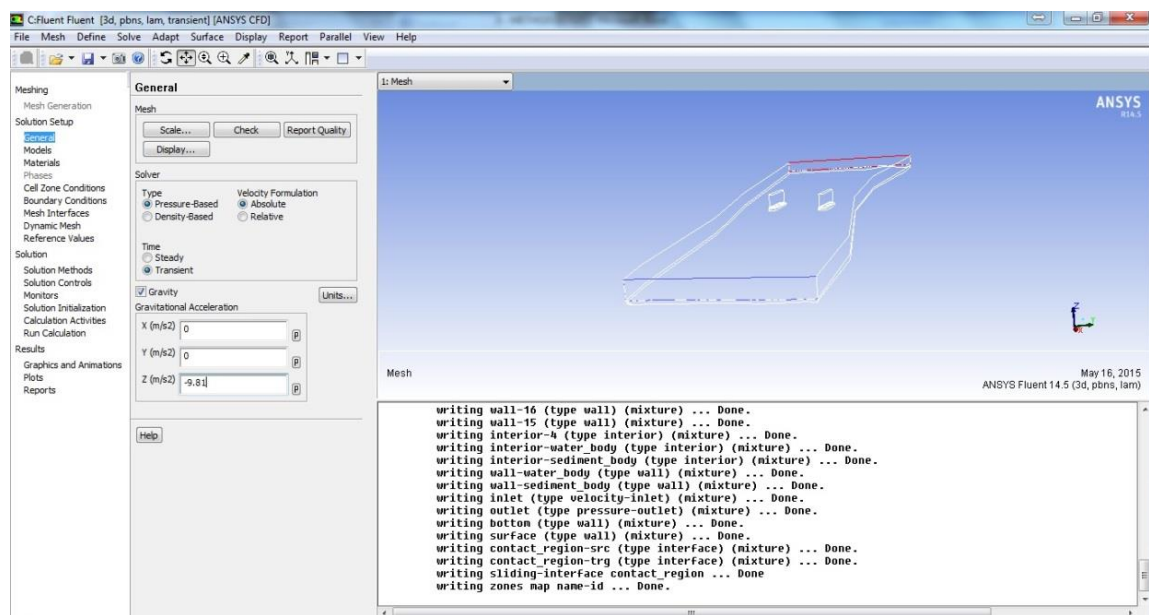


Figure 3.1. A view from a “solution setup” within Fluent.

Nowadays, many companies in the world utilize Fluent solver as an integral part of the design and optimization phases of their product development. Accurate and fast CFD results, flexible moving and deforming meshes and superior parallel stability can be provided owing to advanced solver technology of this solver. It is possible to pause it easily to change flow conditions while programme is running within a single application (Figure 3.2).

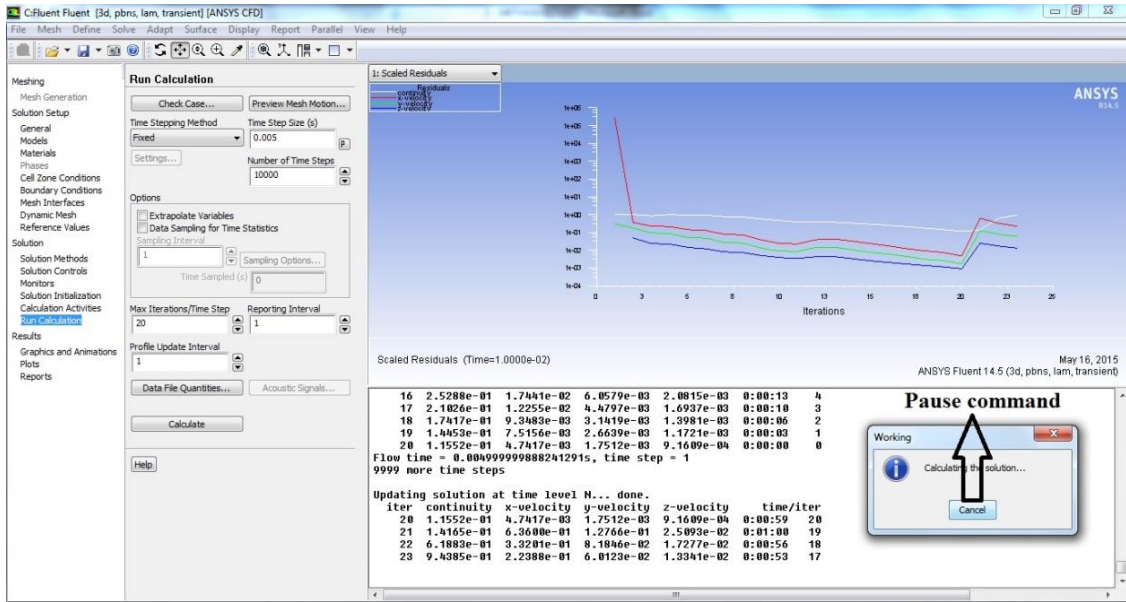


Figure 3.2. A view from “pause command” within Fluent.

After the simulation is complete, ANSYS CFD-Post enables further analysis with advanced post-processing tools. Case and data files can be read into ANSYS CFD-Post easily (Figure 3.3).

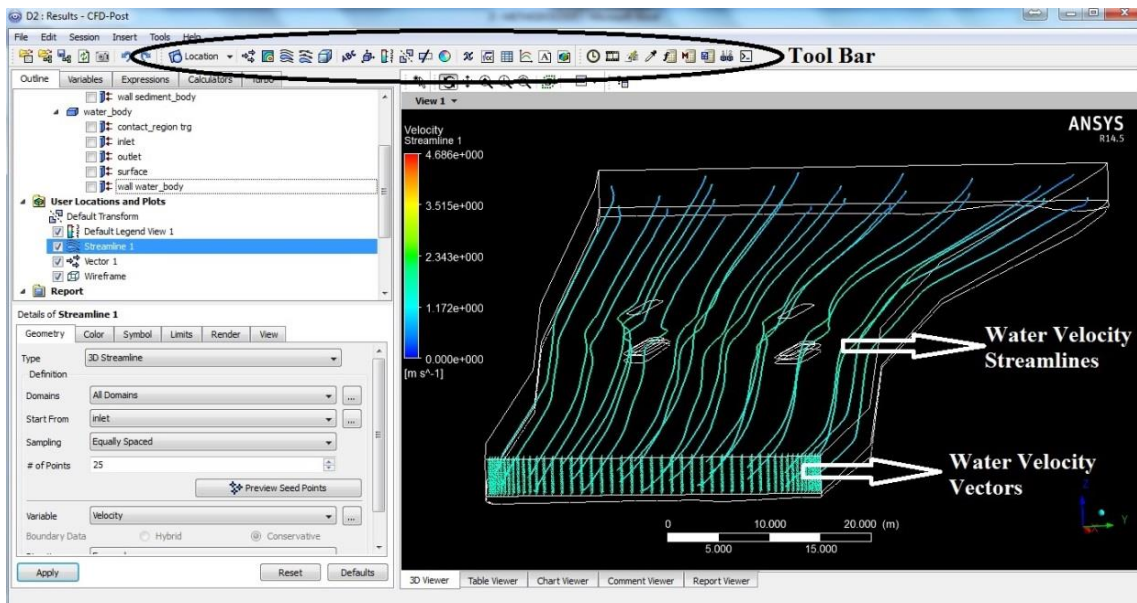


Figure 3.3. A view from “Post Processing” within Fluent.

3.1.2. Turbulence in General

One of the most important phenomena related to the flow dynamics is turbulence. Turbulence in general is produced by mean shear owing to changes in kinetic energy generated by winds or tides and by unstable stratification due to changes in potential energy. Turbulent flows are characterized by their unsteady, irregular, seemingly random and chaotic variation of fluid velocity and pressure in space and time. Greater amount of convective transport and mixing of the fluid occur in turbulence flow than in laminar flows owing to these turbulent fluctuations. Osborne Reynolds (1842-1912) found the non-dimensional Reynolds number that is a measure of the ratio of inertial forces to viscous forces. This invention made the understanding of turbulence flow easier than before. Reynolds number is used to characterize different flow regimes, e.g. in the Reynolds' pipe-flow experiment the flow is turbulent for $Re > 4000$ (Figure 3.4). For high Reynolds numbers the Navier-Stokes equations are very sensitive even to small perturbations and result therefore in chaotic, turbulent solutions. On the contrary, for small Reynolds numbers steady solutions, as a consequence of damping due to viscosity, are achieved. These flows are referred to as laminar [11]. Figure 3.5 shows energy cascade.







$Re < 5$		Creeping flow (no separation)
$5 - 15 < Re < 40$		A pair of stable vortices in the wake
$40 < Re < 150$		Laminar vortex street
$150 < Re < 300000$		Laminar boundary layer up to separation point, turbulent wake
$300000 < Re < 3500000$		Boundary layer transition to turbulent
$Re > 3500000$		Turbulent vortex street, but the separation is narrower than the laminar case

Figure 3.4. Flow characteristics respect to Reynolds Number [12]

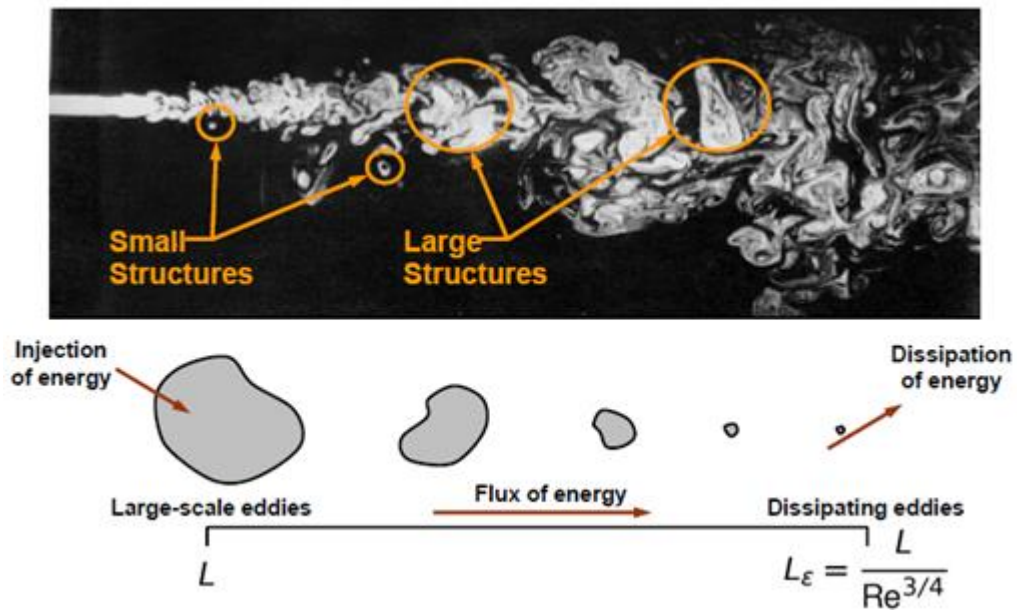


Figure 3.5. Energy cascade [12]

3.1.3. Turbulence Modeling in General

Asking the famous question of “why do we need turbulence modeling?” could be convenient to start. There are two different approaches to answer this question. The first one includes the physical answer, whereas the other one looks into the problem in a more mathematical manner. A fluid flow could be described in several ways. It could be compressible or incompressible, viscous or inviscid, laminar or turbulent. If the last two definitions of flow are investigated in detail, certain parameters to decide on the type of flow whether it is laminar or turbulent could be found. It is likely true to say that one of the most important parameter is the Reynolds number as mentioned. For different types of flow (namely, flow in a pipe, flow over in a channel) different Reynolds numbers of transition from laminar to turbulent flow are defined. If they were a property of a fluid, it is possible to measure the quantities of them; “how turbulent or how laminar flow is?” So here comes the answer to the question about the reason for modeling turbulence; since the presence of a turbulent media is a property flow, it should be modeled.

On the other hand, from a mathematical perspective, Navier-Stokes equations could include the turbulent motion. As mentioned before, statistical methods are used to average the fluctuating properties of flow in the turbulent case. Certain averaging techniques such as spatial, time and ensemble averaging are used to obtain the mean

values of these properties. Homogenous turbulence, that is the averaged turbulent flow uniform in all directions, spatial averaging is used whereas, for stationary turbulence which, on the average, does not vary with time, time averaging is used. But ensemble averaging is the most suitable averaging for flows decaying in time. For the flows that engineers mostly deal with, time averaging is used. Time averaging yields an average and a fluctuating part for a certain variable. These parts could be represented as the part of the instantaneous parameter, say velocity. Figure 3.6 shows both instantaneous velocity contours and time-averaged velocity contours.

$$U_i(x, t) = U_i(x) + u_i'(x, t) \quad (3.1)$$

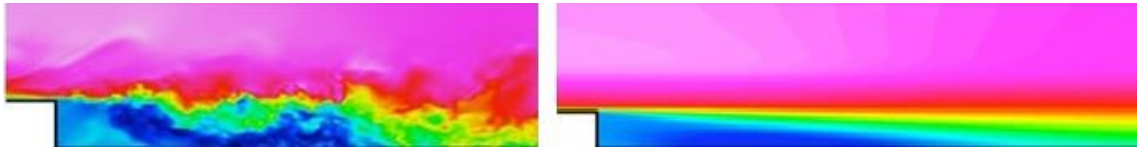


Figure 3.6. Instantaneous velocity contours (left one) and time-averaged velocity (right one) [12]

If this instantaneous velocity term ($u_i(x, t)$) is added into the Navier-Stokes equations so called another well-known equations Reynolds Averaged Navier-Stokes (RANS) are obtained.

$$\rho \cdot \frac{\partial U_i}{\partial t} + \rho \cdot U_j \cdot \frac{\partial U_i}{\partial x_j} = - \frac{\partial P}{\partial x_i} + \frac{\partial}{\partial x_j} \left(2 \cdot \mu \cdot S_{ji} - \rho \cdot \overline{u_j' \cdot u_i'} \right) \quad (3.2)$$

$$R_{ij} = -\rho \begin{pmatrix} \overline{u'u'} & \overline{u'v'} & \overline{u'w'} \\ \overline{v'u'} & \overline{v'v'} & \overline{v'w'} \\ \overline{w'u'} & \overline{w'v'} & \overline{w'w'} \end{pmatrix} \quad (3.3)$$

The quantity $-\rho \cdot \overline{u_j \cdot u_i}$ is known as the Reynolds-stress tensor [12]. It is necessary to understand and find the value of Reynolds stress tensor to determine the mean-flow properties of the turbulent flow. This tensor is a symmetric, second-order tensor; it comes from averaging the convective acceleration term in the momentum equation. Owing to this result it provides averaged effect of turbulent (randomly fluctuating) convection, which is highly diffusive. The mean flow variables could be

solved in the same way as Navier-Stokes equations however the last term of RANS must be modeled [13].

3.1.3.1. Classification of Turbulent Models

Turbulence models are generally classified depending on which governing equations they were applied to (e.g. Reynolds-averaged Navier-Stokes or Large Eddy Simulation equations). Within these broader categories, they are further broken down by the number of additional transport equations which must be solved in order to compute the model contributions.

3.1.3.1.1. Algebraic (Zero-Equation) Models

The simplest (and least computationally expensive) models are the algebraic in other words zero-equation models. They do not solve an additional transport equation in order to predict the contributions of the turbulence. These models are very simple with the advances in computer technologies; they are not used much anymore. Although they can be applied easily since they do not include any transport equations, usually not preferred with the numeric models [14].

3.1.3.1.2. One-Equation Models

One level up in the turbulence modeling system is the one-equation model. These models solve a single transport equation for a quantity which is used to obtain the turbulent viscosity.

Currently, the most popular one-equation model is the Spalart-Allmaras model. This model has been shown to give acceptable results for a wide variety of situations and is known for its stability. Other one-equation models that are available in production codes include the Baldwin-Barth model and the Goldberg point wise model.

It can be considered as an advantage that Goldberg model does not require the calculation of the distance from each field point to the nearest wall. This makes it easier to implement than many other models. However, Goldberg model's results are not as good as Spalart model when wall distance calculation is necessary [15].

3.1.3.1.2.1. Spalart–Allmaras Turbulence Model

This model is a one equation model for turbulent viscosity and it solves just one transport equation for viscosity [16].

The turbulent eddy viscosity is given by

$$\nu_t = \tilde{\nu} f_{\nu 1} \quad (3.4)$$

$$f_{\nu 1} = \frac{X^3}{X^3 + C_{\nu 1}^3} \quad (3.5)$$

$$X := \frac{\tilde{\nu}}{\nu} \quad (3.6)$$

$$\frac{\partial \tilde{\nu}}{\partial t} + u_j \frac{\partial \tilde{\nu}}{\partial x_j} = C_{b1} [1 - f_{t2}] \tilde{S} \tilde{\nu} + \frac{1}{\sigma} \{ \nabla \cdot [(\nu + \tilde{\nu}) \nabla \tilde{\nu}] + C_{b2} |\nabla \mathbf{v}|^2 \} \quad (3.7)$$

$$- \left[C_{\omega 1} f_{\omega} - \frac{C_{b1}}{k^2} f_{t2} \right] \left(\frac{\tilde{\nu}}{d} \right)^2 + f_{t1} \nabla U^2$$

$$\tilde{S} \equiv S + \frac{\tilde{\nu}}{k^2 d^2} f_{\nu 2} \quad (3.8)$$

$$f_{\nu 2} = 1 - \frac{X}{1 + X f_{\nu 1}} \quad (3.9)$$

$$f_{\omega} = g \left[\frac{1 + C_{\omega 3}^6}{g^6 + C_{\omega 3}^6} \right]^{1/6} \quad (3.10)$$

$$g = r + C_{\omega 3} (r^6 - r) \quad (3.11)$$

$$r \equiv \frac{\tilde{\nu}}{\tilde{S} k^2 d^2} \quad (3.12)$$

$$f_{t1} = C_{t1} g_t \exp \left(-C_{t2} \frac{\omega_t^2}{\Delta U^2} [d^2 + g_t^2 d_t^2] \right) \quad (3.13)$$

$$f_{t2} = C_{t3} \exp(-C_{t4}X^2) \quad (3.14)$$

$$S = \sqrt{2\Omega_{ij}\Omega_{ij}} \quad (3.15)$$

The rotation tensor is given by

$$\Omega_{ij} = \frac{1}{2} \frac{\partial u_i}{\partial x_j} - \frac{\partial u_j}{\partial x_i} \quad (3.16)$$

And d is the distance from the closest surface.

Constants are below;

$$C_{b1} = 0,14 \quad C_{b2} = 0,62 \quad k = 0,41 \quad C_{\omega1} = \frac{C_{b1}}{k^2} + \frac{1 + C_{b2}}{\sigma} \quad C_{\omega2} = 0,3 \quad C_{\omega3} = 2 \quad C_{v1} = 7,10 \quad C_{t1} = 1,00 \quad C_{t2} = 2,00 \quad C_{t3} = 1,10 \quad C_{t4} = 2,00$$

3.1.3.1.3. Two-Equation Models

As their name implies, these models require the solution of two additional governing equations in order to compute the contributions of turbulence to the mean flow. Along with the Spalart-Allmaras model, two-equation models make up the bulk of the turbulence models used for production CFD. Two of the most common models are the shear stress transport (SST) model and the k-ε model; however there are many other models in this caption.

The SST model is a blend of a k-ω model, which is used near walls, and a k-ε model, which is used in regions far from walls. This model is fairly advantageous and generally performs well near solid boundaries. It could be helpful to capture re-circulation regions than other models.

The k-ε model would more properly be called a family of models. Specialized versions have been developed for so many specific flow configurations. Some of the more common variants include the Jones-Launder, Chien, and RNG k-ε models.

Besides all these information about models, it could be confusing “low Reynolds number” models applied to obviously high Reynolds number situations. The "low Reynolds number" designation means that the model can be used throughout boundary layers and beyond. A model that is not "low Reynolds number" requires additional wall functions in order to correctly handle the effect of viscous walls [17].

3.1.3.1.3.1. Standard k-ε Model

K-ε turbulence model is the most common model used in Computational Fluid Dynamics (CFD) to simulate mean flow characteristics for turbulent flow conditions. It is a two equation model which gives a general description of turbulence by means of two transport equations (PDEs). The original impetus for the k-ε model was to improve the mixing-length model, as well as to find an alternative to algebraically prescribing turbulent length scales in moderate to high complexity flows. It should be also known that the ratio between Reynolds stress and mean rate of deformations is the same in all directions. The first transported variable determines the energy in the turbulence and is called turbulent kinetic energy (k). The second transported variable is the turbulent dissipation (ε) which determines the rate of dissipation of the turbulent kinetic energy.

Owing to consisting of many unknown and immeasurable term, the standard k-ε turbulence model (Launder and Spalding, 1974) is used which is based on our best understanding of the relevant processes, therefore minimizing unknowns and presenting a set of equations which can be applied to a large number of turbulent applications.

For turbulent kinetic energy (k);

$$\frac{\partial(\rho k)}{\partial t} + \frac{\partial(\rho k u_i)}{\partial x_i} = \frac{\partial}{\partial x_j} \left[\frac{\mu_t}{\sigma_k} \frac{\sigma_k}{\partial x_j} \right] + 2\mu_t E_{ij} E_{ij} - \rho \epsilon \quad (3.17)$$

For dissipation ε;

$$\frac{\partial(\rho \epsilon)}{\partial t} + \frac{\partial(\rho \epsilon u_i)}{\partial x_i} = \frac{\partial}{\partial x_j} \left[\frac{\mu_t}{\sigma_\epsilon} \frac{\sigma_\epsilon}{\partial x_j} \right] + C_{1\epsilon} \frac{\epsilon}{k} 2\mu_t E_{ij} E_{ij} - C_{2\epsilon} \rho \frac{\epsilon^2}{k} \quad (3.18)$$

Putting into words last to equation can be useful to understand. Total rate of change of k or ϵ , transport of k or ϵ by convection and rate of destruction of k or ϵ is equal to total transport of k or ϵ by diffusion and rate of production of k or ϵ .

Where;

u_i represents velocity component in corresponding direction

E_{ij} represents component of rate of deformation

μ_{ij} represents eddy viscosity

$$\mu_t = \rho C_\mu \frac{k^2}{\epsilon} \quad (3.19)$$

$\sigma_k, \sigma_\epsilon, C_{1\epsilon}$ and $C_{2\epsilon}$ are also known as other unknowns. The values of these constants have been arrived at by numerous and many iterations of data fitting for a wide range of turbulent flows. Finally it could be possible to accept them as below[17]:

$$C_{1\epsilon} = 1.44 \quad C_{2\epsilon} = 1.92 \quad C_\mu = 0.09 \quad C_k = 1.0 \quad C_\epsilon = 1.3$$

3.1.3.1.3.2. Standard (Wilcox) k- ω Model

The other common and simplest model is k- ω model. It provides better modeling of the turbulent boundary layer than the standard k- ϵ model, however is more sensitive to the free-stream turbulence levels [14].

This model is a common two-equation turbulence model that is used as a closure for the Reynolds-averaged Navier–Stokes equations (RANS equations). The model attempts to predict turbulence by two partial differential equations for two variables, k and ω , with the first variable being the turbulence kinetic energy (k) while the second (ω) is the specific rate of dissipation (of the turbulence kinetic energy k).

The eddy viscosity ν_T , as needed in the RANS equations, is given by: $\nu_T = k/\omega$, while the evolution of k and ω is modeled as:

$$\frac{\partial(\rho k)}{\partial t} + \frac{\partial(\rho u_j k)}{\partial x_j} = \tau_{ij} \frac{\partial u_i}{\partial x_j} - \beta \rho \omega k + \frac{\partial}{\partial x_j} \left[\left(\mu + \sigma_k \frac{\rho k}{\omega} \right) \frac{\partial k}{\partial x_j} \right] \quad (3.20)$$

$$\begin{aligned} & \frac{\partial(\rho \omega)}{\partial t} + \frac{\partial(\rho u_j \omega)}{\partial x_j} = \\ & \frac{\gamma \omega}{k} \left(\tau_{ij} \frac{\partial u_i}{\partial x_j} \right) - \beta \rho \omega^2 + \frac{\partial}{\partial x_j} \left[\left(\mu + \sigma_\omega \frac{\rho k}{\omega} \right) \frac{\partial \omega}{\partial x_j} \right] + \frac{\rho \sigma_d}{\omega} \frac{\partial k}{\partial x_j} \frac{\partial \omega}{\partial x_j} \end{aligned} \quad (3.21)$$

Where;

$$\tau_{ij} = \mu_t \left(2S_{ij} - \frac{2}{3} \frac{\partial u_k}{\partial x_k} \delta_{ij} \right) - \frac{2}{3} \rho k \delta_{ij} \quad (3.22)$$

$$S_{ij} = \frac{1}{2} \left(\frac{\partial u_i}{\partial x_j} + \frac{\partial u_j}{\partial x_i} \right) \quad (3.23)$$

And the turbulent eddy viscosity is computed from;

$$\mu_t = \frac{\rho k}{\hat{\omega}} \quad (3.24)$$

Where;

$$\hat{\omega} = \max \left[\omega, C_{lim} \sqrt{\frac{\overline{S_{ij} 2S_{ij}}}{\beta^*}} \right] \quad (3.25)$$

$$\overline{S_{ij}} = S_{ij} - \frac{1}{3} \frac{\partial u_k}{\partial x_k} S_{ij} \quad (3.26)$$

and ρ is the density and μ is the molecular dynamic viscosity [18].

3.1.3.1.3.3. Shear Stress Transport (SST) Model

Shear stress transport (SST) model is another important turbulence model in system since it combines advantages of both standard k- ϵ model and k- ω model. SST

model automatically switches to the k- ω Model in the near region and the Standard k- ϵ Model away from the walls.

It was introduced to deal with the strong free stream sensitivity of the k- ω turbulence model and improve the prediction of adverse pressure gradients. Over the last two decades the model has been altered to more accurately reflect certain flow conditions. The Reynolds Averaged Eddy-viscosity is a pseudo-force and not physically present in the system. The two variables calculated are usually interpreted so “k” is the turbulent kinetic energy and “ ω ” is the rate of dissipation of the eddies [19]. Formulation of this system is;

$$\frac{\partial(\rho k)}{\partial t} + \frac{\partial(\rho u_j k)}{\partial x_j} = \tau_{ij} \frac{\partial u_i}{\partial x_j} - \beta^* \rho \omega k + \frac{\partial}{\partial x_j} \left[(\mu + \sigma_k \mu_t) \frac{\partial k}{\partial x_j} \right] \quad (3.27)$$

$$\begin{aligned} \frac{\partial(\rho \omega)}{\partial t} + \frac{\partial(\rho u_j \omega)}{\partial x_j} &= \frac{\gamma}{\vartheta_t} (\tau_{ij} \frac{\partial u_i}{\partial x_j}) - \beta \rho \omega^2 + \frac{\partial}{\partial x_j} \left[(\mu + \sigma_\omega \mu_t) \frac{\partial \omega}{\partial x_j} \right] \\ &+ 2(1 - F_1) \frac{\rho \sigma_{\omega 2}}{\omega} \frac{\partial k}{\partial x_j} \frac{\partial \omega}{\partial x_j} \end{aligned} \quad (3.28)$$

Where;

$$\tau_{ij} = \mu_t \left(2S_{ij} - \frac{2}{3} \frac{\partial u_k}{\partial x_k} \delta_{ij} \right) - \frac{2}{3} \rho k \delta_{ij} \quad (3.29)$$

$$S_{ij} = \frac{1}{2} \left(\frac{\partial u_i}{\partial x_j} + \frac{\partial u_j}{\partial x_i} \right) \quad (3.30)$$

$$\mu_t = \frac{\rho a_1 k}{\max(a_1 \omega, \Omega F_2)} \quad (3.31)$$

$$\vartheta = F_1 \vartheta_1 + (1 - F_1) \vartheta \quad (3.32)$$

$$F_1 = \tanh(\arg_1^4) \quad (3.33)$$

$$\arg_1 = \min \left[\max \left(\frac{\sqrt{k}}{\beta^* \omega d}, \frac{500 \vartheta}{d^2 \omega} \right), \frac{4 \rho \sigma_{\omega 2} k}{CD_{k\omega} d^2} \right] \quad (3.34)$$

$$CD_{k\omega} = \max\left(2\rho\sigma_{\omega 2} \frac{1}{\omega} \frac{\partial k}{\partial x_j} \frac{\partial \omega}{\partial x_j}, 10^{-20}\right) \quad (3.35)$$

$$F_2 = \tanh(\arg_2^2) \quad (3.36)$$

$$\arg_2 = \max\left(\frac{\sqrt{k}}{\beta^* \omega d}, \frac{500\theta}{d^2 \omega}\right) \quad (3.37)$$

Constants are below;

K- ω Closure

$$\sigma_{k1} = 0.85, \quad \sigma_{\omega 1} = 0.65, \quad \beta_1 = 0.075$$

K- ε Closure

$$\sigma_{k2} = 1.00, \quad \sigma_{\omega 2} = 0.856, \quad \beta_2 = 0.0828$$

SST Closure Constants

$$\beta^* = 0.09\alpha_1 = 0.031$$

3.1.3.1.4. Second-Order Closure Models

Owing to the increased complexity of this class of turbulence models, second-order closure models do not share the same wide use as the more popular two-equation or algebraic models. Donaldson and Rosenbaum (1968), Daly and Harlow (1970), and Launder, Reece, and Rodi (1975) were so determined to develop this class of models. The latter has become the baseline second-order closure model, with more recent contributions made by Lumley (1978), Speziale (1985, 1987a), Reynolds (1987), and many other thereafter, who have added mathematical rigor to the model formulation [15].

3.1.3.1.4.1. Reynolds Stress Equation Model

Reynolds stress equation model (RSM), also known as second order or second moment closure model is the nearly most complex classical turbulence model. Several shortcomings of k- ϵ turbulence model were observed when it was attempted to predict flows with complex strain fields or substantial body forces. The Reynolds averaged momentum equations for the mean velocities are:

$$\frac{\partial U_i}{\partial t} + \frac{\partial(\rho u_i u_j)}{\partial x_j} - \frac{\partial}{\partial x_j} \left[\mu \left(\frac{\partial U_i}{\partial x_t} + \frac{\partial U_j}{\partial x_i} \right) \right] = -\frac{\partial p''}{\partial x_i} - \frac{\partial(\rho \overline{u_i u_j})}{\partial x_j} + S_{M_i} \quad (3.38)$$

Where p'' is a modified pressure, S_{M_i} is the sum of body forces and the fluctuating Reynolds stress contribution is $-\rho \overline{u'_i u'_i}$. Unlike eddy viscosity models, the modified pressure has no turbulence contribution and is related to the static (thermodynamic) pressure by:

$$p'' = p + \frac{2}{3} \mu \frac{\partial U_k}{\partial x_k} \quad (3.39)$$

In the differential stress model, $-\rho \overline{u'_i u'_i}$ is made to satisfy a transport equation. A separate transport equation must be solved for each of the six Reynolds stress components of $-\rho \overline{u'_i u'_i}$. The differential equation Reynolds stress transport is:

$$\begin{aligned} \frac{\partial(\rho \overline{u_i u_j})}{\partial t} + \frac{\partial(U_k \rho \overline{u_i u_j})}{\partial x_k} - \frac{\partial}{\partial x_t} \left[\left(\delta_{kl} \mu + \rho C_s \frac{k}{\epsilon} \overline{u_k u_l} \right) \frac{\partial(\overline{u_i u_j})}{\partial x_l} \right] \\ = P_{ij} - \frac{2}{3} \delta_{ij} \rho \epsilon + \Phi_{ij} + P_{ij,b} \end{aligned} \quad (3.40)$$

Where P_{ij} and $P_{ij,b}$ are shear and buoyancy turbulence production terms of the Reynolds stresses respectively Φ_{ij} is the pressure-strain tensor, and C is a constant. Buoyancy turbulence terms $P_{ij,b}$ also take the buoyancy contribution in the pressure strain term into account and are controlled in the same way as for the k- ϵ and k- ω turbulence models.

It could be considered using a Reynolds Stress model in the following types of flow such as: free shear flows with strong anisotropy, like a strong swirl component (flows in rotating fluids), flows with sudden changes in the mean strain rate, flows where the strain fields are complex, and reproduce the anisotropic nature of turbulence itself, flows with strong streamline curvature, secondary flow and buoyant flow.

3.1.3.1.4.1.1. Advantages and Disadvantages of RSM

When advantages of RSM are considered owing to use of an isotropic eddy viscosity, it is simpler than k - ϵ model. In many cases, it is the most general of all turbulence models and work reasonably well. Only the initial and/or boundary conditions are necessary. It can selectively damp the stresses owing to buoyancy, curvature effects etc. This is because it does not need to model the production term.

Main disadvantage of RSM is that they require a lot of computation time. K - ϵ and mixing length models are more validated than RSM. Owing to identical problems with the ϵ -equation modeling, it performs just as poorly as the k - ϵ model in some problems. In order to predict normal stresses RSM is not a good model owing to being isotropic. It is not able to account for irrotational strains neither [20].

3.1.3.1.4.2. Large Eddy Simulation (LES)

Large eddy simulation (LES) is a mathematical model for turbulence used in computational fluid dynamics. It was initially proposed in 1963 by Joseph Smagorinsky to simulate atmospheric air currents, and many of the issues unique to LES were first explored by Deardorff (1970). LES grew rapidly beginning with its invention in the 1960s and is currently applied in a wide variety of engineering applications, including combustion, acoustics, and simulations of the atmospheric boundary layer. LES operates on the Navier–Stokes equations to reduce the range of length scales of the solution, reducing the computational cost.

The principal operation in large eddy simulation is low-pass filtering. This operation is applied to the Navier–Stokes equations to eliminate small scales of the solution. This reduces the computational cost of the simulation. The governing equations are thus transformed, and the solution is a filtered velocity field.

Large eddy simulation resolves large scales of the flow field solution allowing better fidelity than alternative approaches such as Reynolds-averaged Navier–Stokes (RANS) methods. It also models the smallest (and most expensive) scales of the solution, rather than resolving them as direct numerical simulation (DNS) does. This situation can cause the computational cost for practical engineering systems with flow configurations or complex geometry, such as vehicles, pumps and turbulent jets. In contrast, direct numerical simulation, which resolves every scale of the solution, is prohibitively expensive for nearly all systems with complex geometry or flow configurations.

A filtered variable is denoted in the following by an overbar and is defined by

$$\Phi(\mathbf{x}) = \int_D \Phi(\mathbf{x}')G(\mathbf{x}; \mathbf{x}')d\mathbf{x}' \quad (3.41)$$

Where D is the fluid domain and G is the filter function that determines the scale of the resolved eddies. The unresolved part of a quantity ϕ is defined by

$$\Phi' = \Phi - \bar{\Phi} \quad (3.42)$$

It should be noted that the filtered fluctuations ($\bar{\Phi}$) are not zero. The discretization of the spatial domain into finite control volumes implicitly provides the filtering operation:

$$\Phi(\mathbf{x}) = \frac{1}{V} \int_V \Phi(\mathbf{x}')d\mathbf{x}' \quad ; \quad \mathbf{x}' \in V \quad (3.43)$$

Where V is the control volume. The filter function $G(\mathbf{x}; \mathbf{x}')$ implied here is then

$$G(\mathbf{x}; \mathbf{x}') = \begin{cases} \frac{1}{V} & , \quad \mathbf{x}' \in V \\ 0 & , \quad \text{otherwise} \end{cases} \quad (3.44)$$

Filtering the Navier-Stokes equations leads to additional unknown quantities. In the following the theory will be outlined for the incompressible equations. The filtered incompressible momentum equation can be written in the following way:

$$\frac{\partial \bar{U}_i}{\partial t} + \frac{\partial (u_i u_j)}{\partial x_j} = -\frac{1}{\rho} \frac{\partial \bar{p}}{\partial x_i} + \frac{\partial}{\partial x_j} \left[\nu \left(\frac{\partial \bar{U}_i}{\partial x_j} + \frac{\partial \bar{U}_j}{\partial x_i} \right) \right] = -\frac{\partial \tau_{ij}}{\partial x_j} \quad (3.45)$$

Where τ_{ij} denotes the subgrid-scale stress. It includes the effect of the small scales and is defined by

$$\tau_{ij} = \overline{u_i u_j} - \bar{U}_i \bar{U}_j \quad (3.46)$$

The large scale turbulent flow is solved directly and the influence of the small scales is taken into account by appropriate subgrid-scale (SGS) models. In ANSYS CFX an eddy viscosity approach is used which relates the subgrid-scale stresses τ_{ij} to the large-scale strain rate tensor \bar{S}_{ij} in the following way:

$$-\left(\tau_{ij} - \frac{\delta_{ij}}{3} \tau_{kk} \right) = 2\nu_{sgs} \bar{S}_{ij} \quad (3.47)$$

$$\bar{S}_{ij} = \frac{1}{2} \left(\frac{\partial \bar{U}_i}{\partial x_j} + \frac{\partial \bar{U}_j}{\partial x_i} \right) \quad (3.48)$$

Unlike in RANS modeling, where the eddy viscosity ν_{sgs} represents all turbulent scales, the subgrid-scale viscosity only represents the small scales [21].

3.1.4. Available Turbulent Models in Fluent

In Fluent Solver, there are many turbulence models to be utilized (Table 3.1). Standard k- ϵ model and SST k- ω models are applied for the modeling purposes in this thesis.

Table 3.1. Turbulence models in Fluent solver

Turbulence Models In Fluent Solver	Number of Equations Used
Spalart-Allmaras (Vorticity-Based)	1
Spalart-Allmaras (Strain/Vorticity-Based)	1
Standard k- ϵ	2
Renormalization-group (RNG) k- ϵ	2
Realizable k- ϵ model	2
Standard k- ω	2
SST k- ω	2
Transition k-k1- ω	3
Transition SST	4
Reynolds Stress Linear Pressure-Strain	7
Reynolds Stress Quadratic Pressure-Strain	7
Reynolds Stress - ω	7
Scale-Adaptive Simulation (SAS)	-
Detached Eddy Simulation (DES)	-
Large Eddy Simulation (LES)	-

3.2. Multiphase Particle Modeling in Fluent

Multiphase modeling consists of simultaneous flow of materials with different states or phases (i.e. gas, liquid or solid) or different chemical properties but in the same state or phase (i.e. liquid-liquid systems such as oil droplets in water). The primary and secondary phases should be known and applied correctly as well. One of the phases is continuous (primary) while the other(s) (secondary) are dispersed within the continuous phase. In this thesis, primary phase is considered as water and secondary phases are specified as sediment. The sediment properties such as concentration and diameter were obtained by field monitoring conducted at B. Menderes River in order to simulate the sediment laden flow. Additionally, the mean diameter has to be assigned for each secondary phase to calculate its interaction (drag) with the primary phase and a

secondary phase with a particle size distribution is modeled by assigning a separate phase for each particle diameter.

3.2.1. Euler-Lagrange Approach

The Lagrangian discrete phase model in ANSYS FLUENT follows the Euler-Lagrange approach. The fluid phase is treated as a continuum by solving the Navier-Stokes equations, while the dispersed phase is solved by tracking a large number of particles, bubbles, or droplets through the calculated flow field. The dispersed phase can exchange momentum, mass, and energy with the fluid phase.

This approach is made considerably simpler when particle-particle interactions can be neglected, and this requires that a low volume fraction is occupied by the dispersed second phase, even though high mass loading ($m_{\text{particles}} > m_{\text{fluid}}$) is acceptable. During the fluid phase calculation, the droplet or particle trajectories are computed individually at specified intervals. This situation makes the model appropriate for the modeling of particle-laden flows, but inappropriate for the modeling of fluidized beds, liquid-liquid mixtures or any application where the volume fraction of the second phase cannot be neglected. Particle-particle interactions can be included using the Discrete Element Model for applications such as these [22].

3.2.1.1. Discrete Element Model

The discrete element method is suitable for simulating granular matter (such as gravel, coal, beads of any material). Such simulations are characterized by a high volume fraction of particles, where particle-particle interaction is important. It is likely true to say that interaction with the fluid flow may or may not be important. Typical applications include risers, fluidized beds, hoppers, packed beds and pneumatic transport [14].

3.2.2. Euler-Euler Approach

In this approach, different phases are treated mathematically and phase volume fraction is defined in the model. It is assumed that volume fractions are continuous

functions of time and space and their sum is equal to one. In order to obtain a set of equations, conservation equations for each phase are derived, which have similar structure for all phases. These equations are closed by providing constitutive relations obtained from in the case of sediment-laden flows, or, empirical information by application of kinetic theory.

In ANSYS Fluent, three different Euler-Euler multiphase models are available. They are the volume of fluid (VOF) model, the mixture model, and the Eulerian model [14].

3.2.2.1. VOF Model

The Volume of Fluid model is a surface-tracking technique applied to a fixed Eulerian mesh. It is designed for two or more immiscible fluids where the position of the interface between the fluids is of interest. In the VOF model, a single set of momentum equations is shared by the fluids, and the volume fraction of each of the fluids in each computational cell is tracked throughout the domain. Applications of the VOF model include stratified flows, free-surface flows, filling, sloshing, the motion of large bubbles in a liquid, the motion of liquid after a dam break, the prediction of jet breakup (surface tension), and the steady or transient tracking of any liquid-gas interface [14].

3.2.2.2. Mixture Model

The mixture model is designed for two or more phases (fluid or particulate). As in the Eulerian model, the phases are treated as interpenetrating continua. The mixture model solves the mixture momentum equation and prescribes relative velocities to describe the dispersed phases. Applications of the mixture model include particle-laden flows with low loading, bubbly flows, sedimentation, and cyclone separators. The mixture model can also be used without relative velocities for the dispersed phases to model homogeneous multiphase flow [14].

3.2.2.3. Eulerian Model

The most complex of multiphase models is the Eulerian model in ANSYS FLUENT. Continuity and momentum equations are solved for each phase in this model. Pressure and interphase exchange coefficients are used in the coupling process. This coupling is handled depending on the phases involved; only fluid flows are handled differently than fluid-solid flows. For fluid-solid flows, the properties are obtained from kinetic theory. Type of mixture being modeled is also important for momentum exchange between the phases. “User defined function” (UDF) allows users to modify the calculation of the momentum exchange in many cases. Applications of the Eulerian multiphase model involve fluidized beds, sediment-laden flow and air bubble water columns [14, 23].

3.3. Models Utilized in Modeling of Flow and Sediment Transport in This Study

In the first phase of this study, effects of turbulence model (standard k- ϵ , standard k- ω and Reynolds models) were investigated through modeling of flow in front of the intake structure located at Tahtalı Reservoir. Total length of the model domain in these simulations was 200 m, where total width and water depth were 100 m and 30,5 m, respectively. Sides of the model domain were defined as symmetry and there was a circular withdrawal point having 2 meter diameter at 9 meters below the surface. Water was withdrawn from sides to outlet with constant discharge. In order to obtain constant discharge and withdraw water, constant water velocity was defined in reverse direction (-x) by using velocity inlet boundary condition for inlet surface.

Based on the findings of the previous simulations, standard k- ϵ and SST k- ω turbulence models were used to model flow in B. Menderes River for the second phase of this study. Since the interest was only to investigate the effect of turbulence models, only water phase was considered in the model and sediment layer having irregular bottom shape was suppressed from the simulation domain to overcome time-consuming effects of it. Total length of the model domain in these simulations was selected as 180 meters, where total width and water depth were 40 m and 3.7 m respectively. Sides of

water column were defined as wall and there were inlet and outlet surfaces defined as “velocity inlet” and “pressure outlet”. Discharge was defined at a constant rate.

In the third phase, the Eulerian - Lagrangian method was used in a simple geometry being alternative geometry of B. Menderes River in order to understand effects of k- ϵ turbulent model on sediment particles having different median diameters. Realizable wall function boundary condition was applied for turbulent model because it is more effective in “discrete phase method” simulations. Eulerian multiphase method was chosen to simulate bed load and Discrete Phase Method (DPM) was used to simulate suspended particles. In order to simulate bed load, three phases having different median diameters were utilized and three different simulations with different median diameters under the same conditions were compared.

In these simulations discharge was again constant. Next, the comparison of two turbulence models; of k- ϵ and k- ω turbulence models on simulation of sediment particles were discussed.

The fourth phase involved the repetition of the third step using a varying hydrograph rather than using a constant discharge rate as achieved in the third step.

In the fifth phase, sediment laden flow in B. Menderes River was simulated and trajectory of sediment particles was discussed using Eulerian-Lagrangian method. In order to inject particles, Rosin Rammler logarithmic distribution was used with respect to sediment data obtained from field monitoring earlier. Flow data used in the simulations were obtained from the monitored data during our field campaign and inlet velocity was defined as 1.4 m/s based on our measurements.

Once numerical modeling of flow in B. Menderes River was completed, an approach on modification of settling velocity with turbulence characteristics was developed. For this purpose, we focused on the utilization of user defined function (UDF) of drag force on a particle and modified the settling velocity using turbulence characteristics.

CHAPTER 4

MONITORING FIELD DATA

4.1. Field Data Monitoring

4.1.1. Study Site

The observations were conducted in B. Menderes River, Turkey to monitor synchronized velocity and temperature time series data, and sediment data. Certain location near B. Menderes Bridge with coordinates of $37^{\circ}46'56.82''N$ and $27^{\circ}50'23.56''E$ is chosen.

B. Menderes River originates in west central of Turkey near Dinar, Afyon and flows through Lake Işıklı. After passing Adıgüzel and Cindere Dam and Söke, Aydın, it drains into the Aegean Sea. Total length of the river is 548 km and total basin area is 25000 km² [24].

B. Menderes Bridge, also known as Old Aydın Bridge is an historical bridge. In order to obtain turbulent conditions, it is a suitable location for field data (Figure 4.1). Old Aydın Bridge has expanding cylindrical piers. During the field observations, as a result of changing weather and ambient conditions, only two piers were in water and these were considered in the model domain.



Figure 4.1. B. Menderes Bridge (Old Aydın Bridge) and B. Menderes River

4.1.2. Instrumentation

Bathymetry used for simulation of B. Menderes River bottom shape was monitored via Echo Sounder instrument.

Echo sounder produced by Knudsen is an instrument to measure depth of water via sending ultrasonic sound waves. Echo sounder uses ultrasonic waves owing to easy spreading in water column. It sends 14-200 kHz ultrasonic sound waves into the water from surface to bottom and these ultrasonic waves reflect back to the surface after clash. B. Menderes River bathymetry was obtained by applying this method throughout the river for the selected portion of it.

For suspended sediment, sediment data collected and analyzed by sieve and hydrometer analysis obtained from an earlier study [25] was used and for bed sediment, sediment data collected from the bottom surface of field site earlier by Dr. Bor (unpublished data) was used.

Temperature data was measured by thermistor chain composed of RBR temperature sensors at the study site. The sensors have accuracy of ± 0.002 and can measure temperature for a range of -5 - 35 °C. The main reason why this instrument was used is that it has high accuracy.

RBR is easy to use and require minimal service intervention. It needs low power to deploy. After measurement, it has to be connected to PC or Mac via a connection cable and it is easy to display results via Ruskin software that manages your RBR loggers (Figure 4.2). It provides a graphical user interface to be used easily. Via this software, it is possible to configure enable multiple loggers and schedule, download data after logging, export data in various formats and change the calibration coefficients for logger.

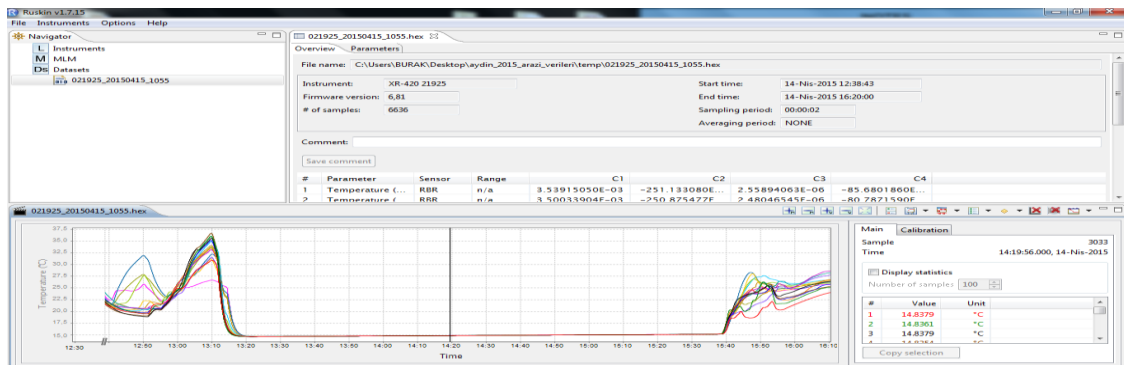


Figure 4.2. View of Ruskin Programme

Water velocity data were obtained via Acoustic Doppler Current Profiler (ADCP), which uses active acoustics to measure current throughout the water column [26].

Acoustic Doppler Current Profiler (ADCP) is an instrument which measure velocity of the water in 3D via triceps sensors [27]. It is easy to use gives accurate and reliable results to obtain turbulent characteristics. State-of-the-art transducers and electronics are used by ADCP. Thanks to these benefits, side-lobe interference problems that plague other current profilers could be reduced easily. This allows this instrument to make the very near-boundary (bottom or surface) current measurements critical to shallow water applications. When sensitivity of ADCP is considered, maximum profiling range is 1500 KHz for distance from 15 m to 25 m, velocity range is between ± 10 m/s, velocity resolution is 0,1 cm/s and velocity accuracy is $\pm 1\%$ of measured velocity ± 5 cm/s.

The main principle of this instrument is to be accomplished by transmitting a sound pulse at a fixed frequency and listening for the Doppler shift in echoes returned from sound scatters in the water column. The difference between the frequency which is transmitted and the frequency which is reflected off of a moving particle back to the source is main procedure of ADCP. Due to this convenience, particle velocities could be directly measured rather than estimating indirectly from balance between settling and diffusive flux gradients [26].

After measurement, it has to be connected to PC or Mac via a connection cable and it is easy to display results via “Deploy ADP” or “SunUTILS” software that manages your ADCP loggers. It is possible to download field velocity measurements by using these programs as “.ve” format. After download, View ADP should be used to view downloaded data. At input screen of View ADP, not only profiles that were desired to be shown can be selected, but also it is possible to get average values (Figure 4.3). At the main screen of software, x y z directions of water velocity can be displayed (Figure 4.4).

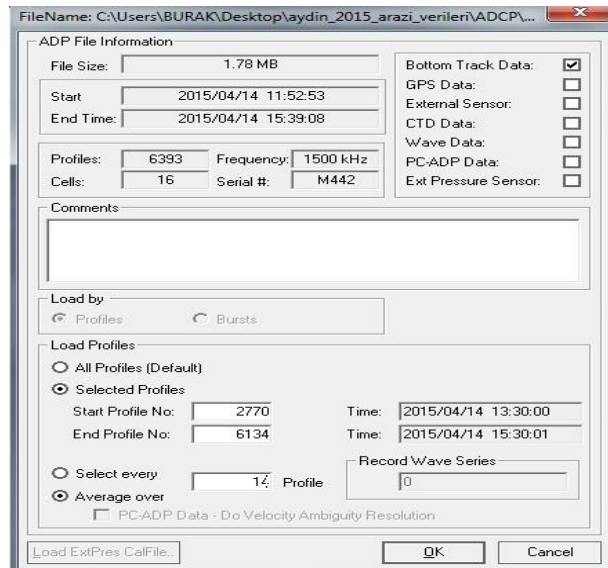


Figure 4.3. Screenshot of ViewADP ADCP file information screen

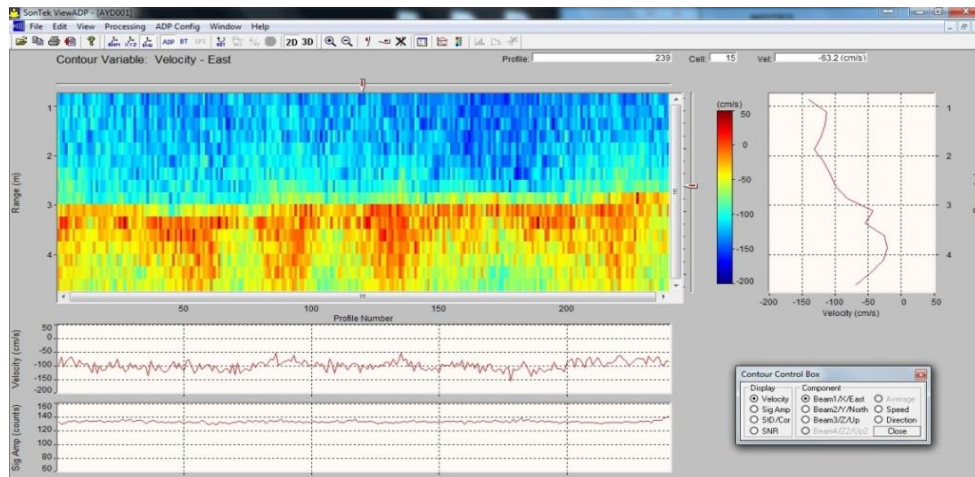


Figure 4.4. View of ADCP

4.1.3. Simultaneous Deployment of Acoustic Doppler Current Profiler and Thermistor Chain

The purpose of the deployment was to collect synchronized 3-D velocity and temperature time series data and for this purpose a 1,5 MHz Acoustic Doppler current Profiler was mounted to a buoy in down-looking mode (Figure 4.5).



Figure 4.5. Simultaneous measurements of temperature and velocity

Blanking distance of the ADCP is defined as 62.5 cm, so that velocity measurements in the vertical were recorded at the same locations with the temperature measurements recorded by the sensors of the thermistor chain. Vertical resolution of both velocity and temperature measurements were 25 cm. The measurements extended for 16 cells corresponding to 4 m of depth. A thermistor chain having 16 thermistors placed 25 cm apart on a cable was used and mounted on the same buoy. Total amount of cells of ADCP and RBS were the same (16) and first temperature sensor was superposed to first ADCP velocity cell considering blanking distance (Figure 4.6). As mentioned, thermistors deployed for this study are produced by RBR and have accuracy of $\pm 0.002^{\circ}\text{C}$. Sampling was made at 1 second frequency.

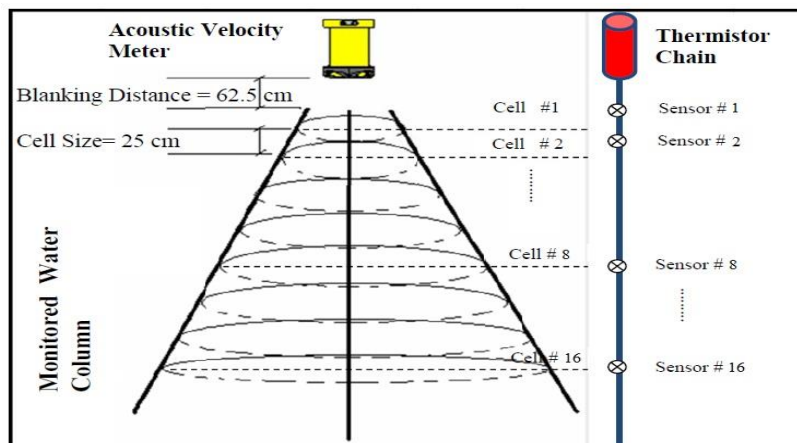


Figure 4.6. Cell size selected during the measurement

4.2. Analysis of Field Data

Instantaneous 3-D velocity and temperature values were monitored at Aydın Bridge on Büyük Menderes River using ADCP for velocity and thermistor chain for temperature measurements. Figure 4.7 shows a view during the field measurements. Both instruments were deployed on a boat and tied to the railings on the bridge where the boat was fixed on the water surface via three ropes.

Monitoring achieved in March 2015 and data for collected for two hours used in the analysis. Figure 4.8 shows the water temperature monitored with respect to water depth during the measurement period. Figure 4.9 shows monitored flow velocities for every second and Figure 4.10 shows flow velocities in 3-D of which 1 minute averaging is applied respectively. When measured velocity magnitude was taken averaged respect to depth, Figure 4.11 was obtained. Maximum velocity magnitude was 1,4 m/s and this value was used for all simulations.



Figure 4.7. A view from the measurements

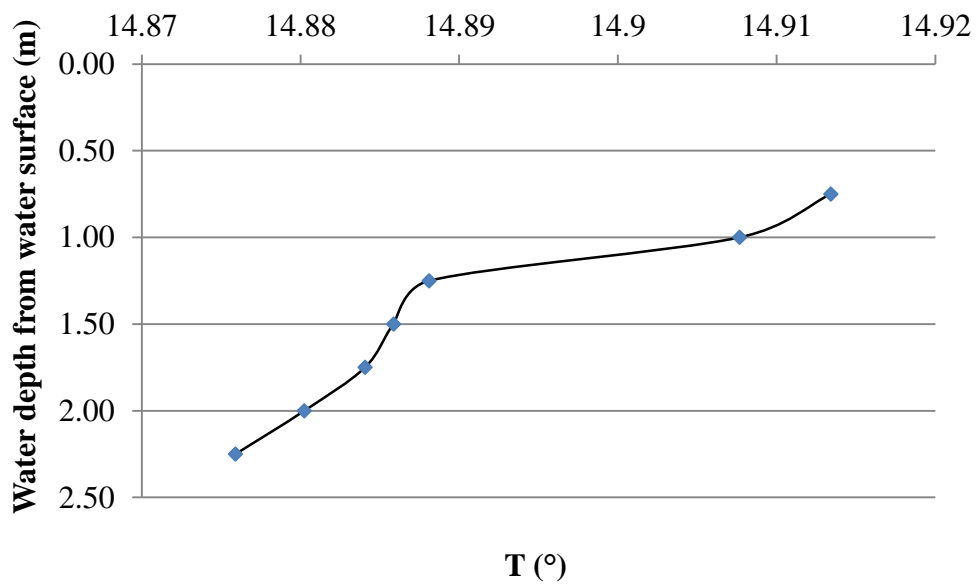


Figure 4.8. Observed water temperature along the water column

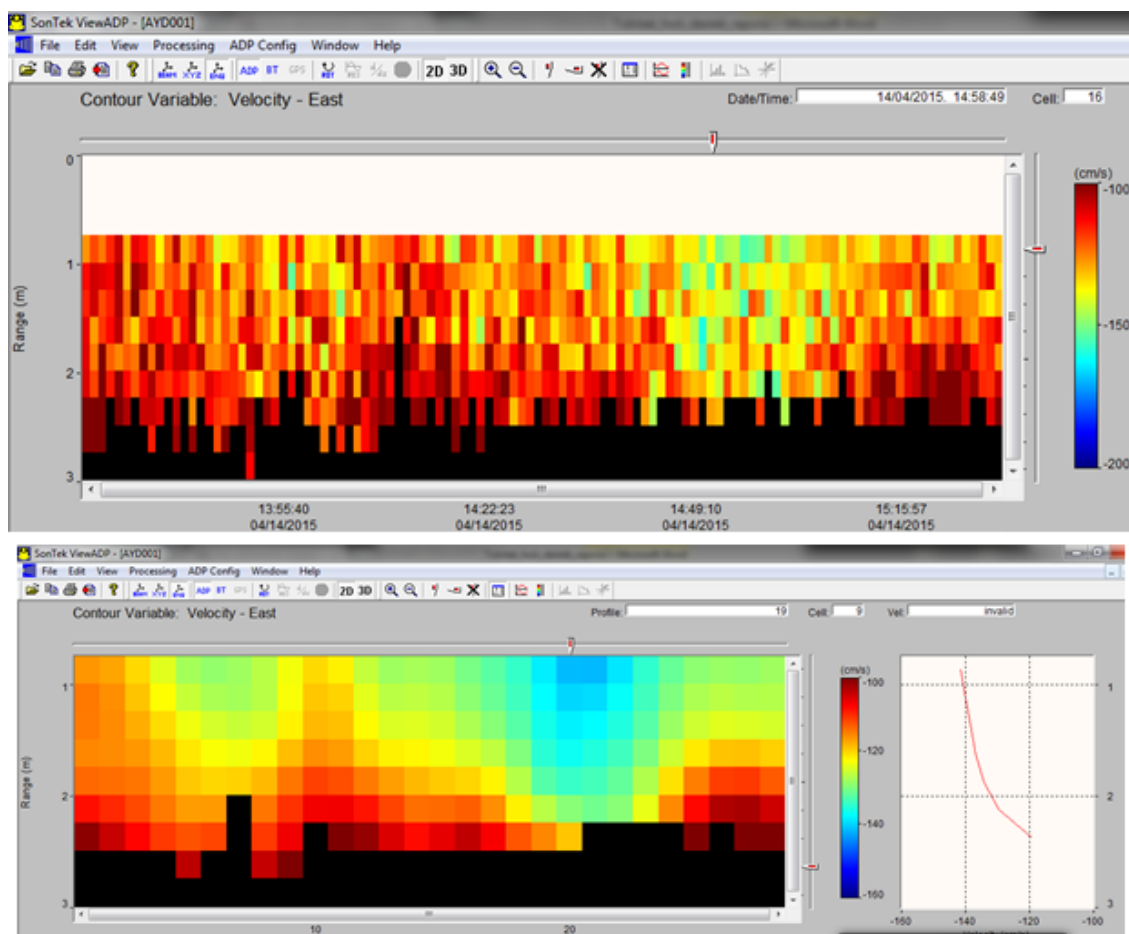


Figure 4.9. Monitored flow velocities during the measurement campaign (above) and instantaneous flow velocity while measurement (below)

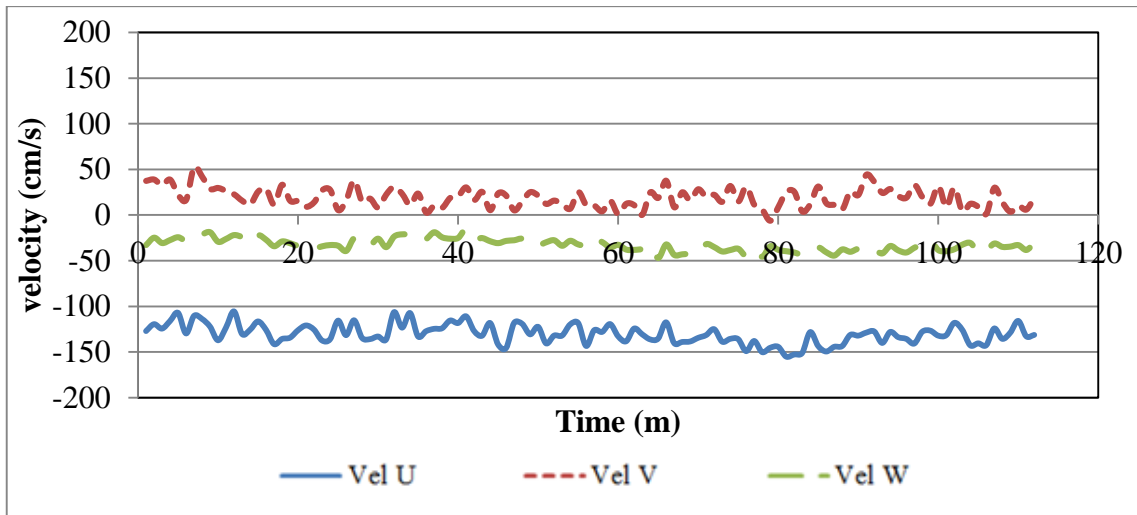


Figure 4.10. 1 minute time averaged 3D flow velocities (u,v,w) measured by the ADCP during the field campaign

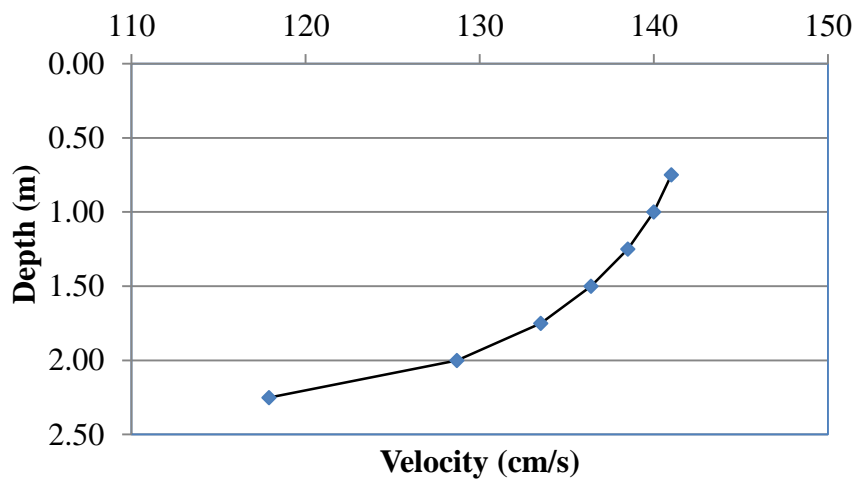


Figure 4.11. Variation of the time averaged flow velocity with respect to depth.

Figure 4.12 shows sieve and hydrometer analysis of the sediment collected at B. Menderes River earlier [25]. Fine sediments observed were used as a reference to represent suspended sediment at the study site simulates interaction between sediment particles and water. Median diameter of fine sediments observed at the study site was 0,003 mm, minimum diameter was 0,001 mm and maximum diameter was 0,005 mm.

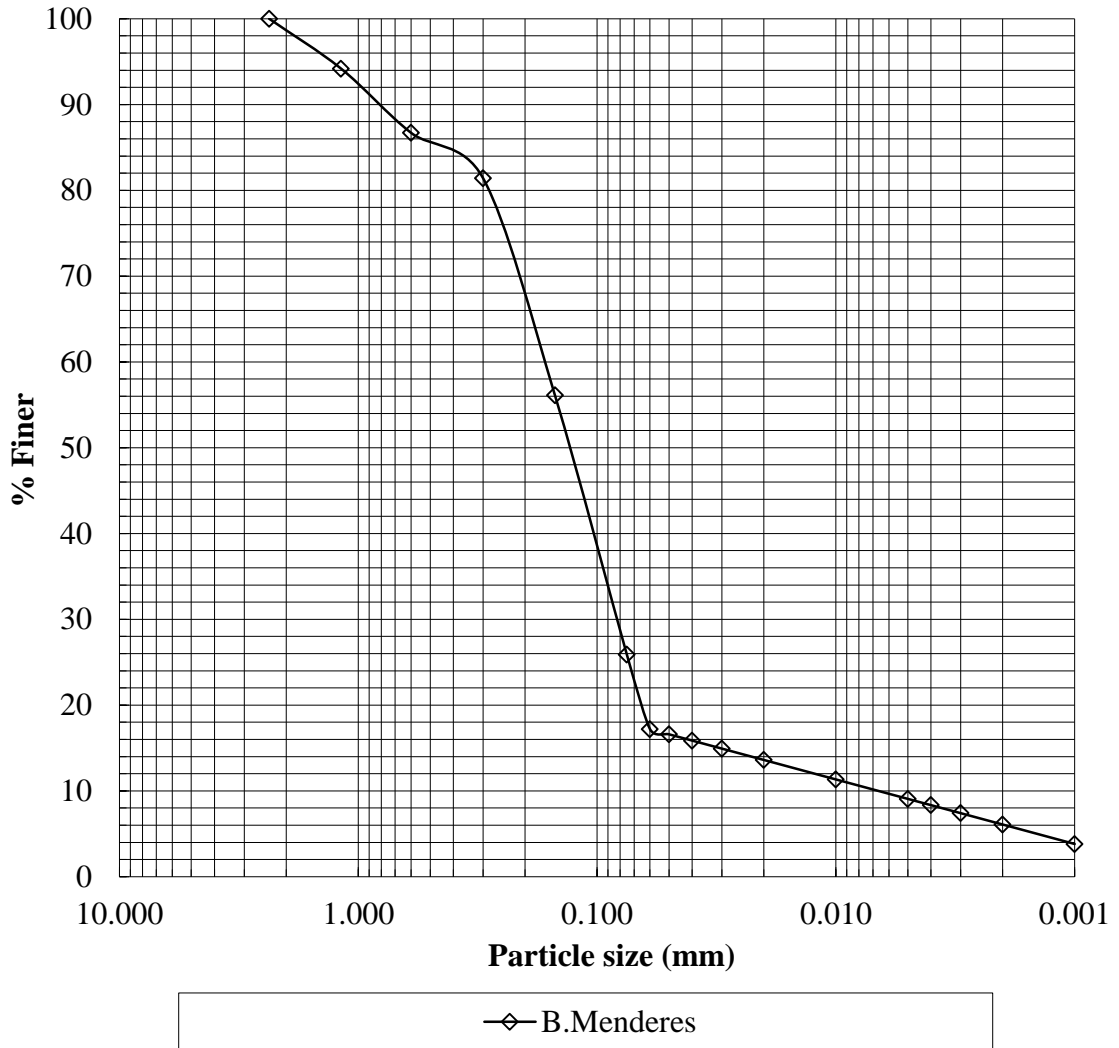


Figure 4.12. Variation of the time averaged flow velocity with respect to depth.

Figure 4.13 was obtained from field work in Tahtalı Reservoir which was given in the next topic as first CFD simulation and it is easy to say that there is a considerable amount of turbulence effects on settling velocity in turbulent flow. When calculated turbulence intensity (w'/w) and sediment settling velocity (w) were plotted together, settling velocity -in other words sediment transport- was changing with respect to turbulence intensity considerably. This information is utilized to create a new UDF for Fluent Solver for reformulation of the settling velocity. This UDF was applied for B. Menderes domain as will be explained in Chapter 6.

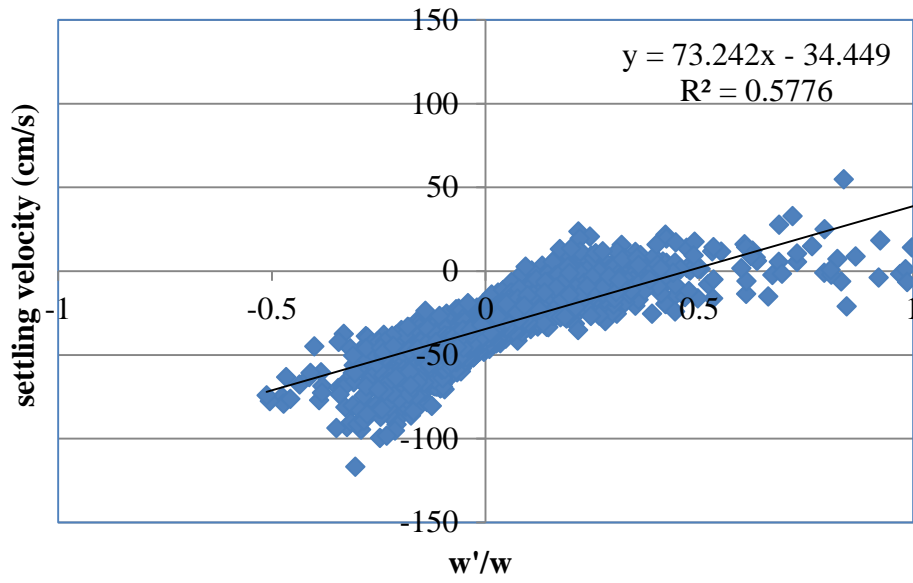


Figure 4.13. Comparison between measured settling velocity via ADCP and calculated turbulence characteristics

CHAPTER 5

CFD MODELING OF THE FLOW

5.1. Computational Domain

Although the main purpose of this study was to simulate flow and sediment transport in the selected portion of B. Menderes River, numerical modeling study achieved in this thesis consisted of various computation domains (simple and main domains). The reason for the selection of these domains in investigation of various parameters was the extensive computation time (several weeks) required for modeling of the main domain.

5.1.1. Generating Geometry

The main domain was selected such that it included the piers of the Old Aydın Bridge in the center of 180 m of river portion B. Menderes (Figure 5.1). It is hard to create exact geometry of the river due to irregular bottom shape and sides. However, in order to obtain best geometry, “.sat” file was created by entering all measured points at the field via AutoCAD Civil 3D. Many ANSYS users prefer importing related geometry from outside instead of generating it via ANSYS due to difficulty of usage and inadequacy to generate hard geometries. This 3D geometry which was generated by AutoCAD Civil 3D was imported to ANSYS (Figure 5.2).



Figure 5.1. Google Earth view of simulation area

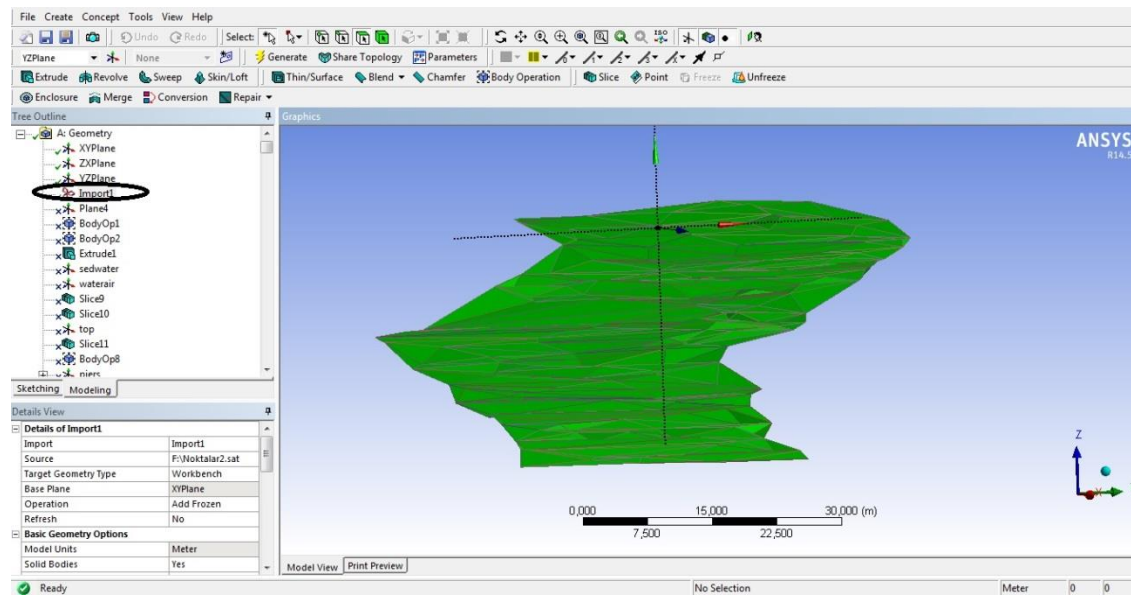


Figure 5.2. Bottom surface of B. Menderes River in ANSYS before merging

Imported surface was sewed and extruded in Z direction via “body operation” command (Figure 5.3). Depth of water was selected 4,5 m by obtained from field measurements.

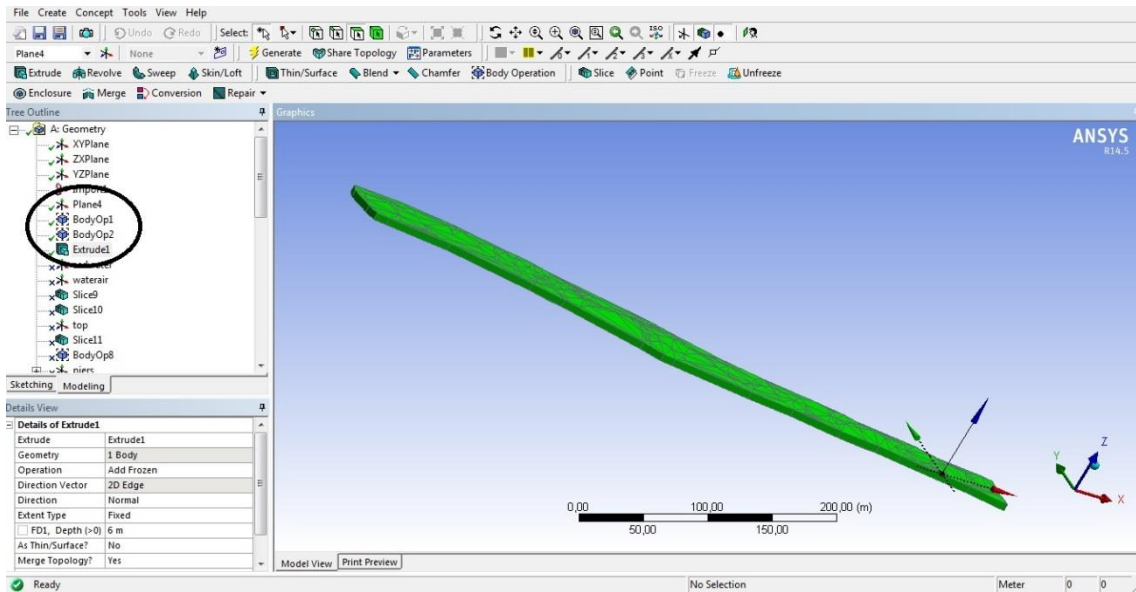


Figure 5.3. 3D body of B. Menderes River in ANSYS

After generating 3D geometry, sediment layer was cut via “slice” command through XY plane direction. Maximum total depth of sediment layer was taken as 0,8 m, however it depends on bottom surface roughness and amount of irregularity. While at some points depth of sediment layer is as low as 2-3 cm, it could be 0,7-0,8 m at other locations (Figure 5.4).

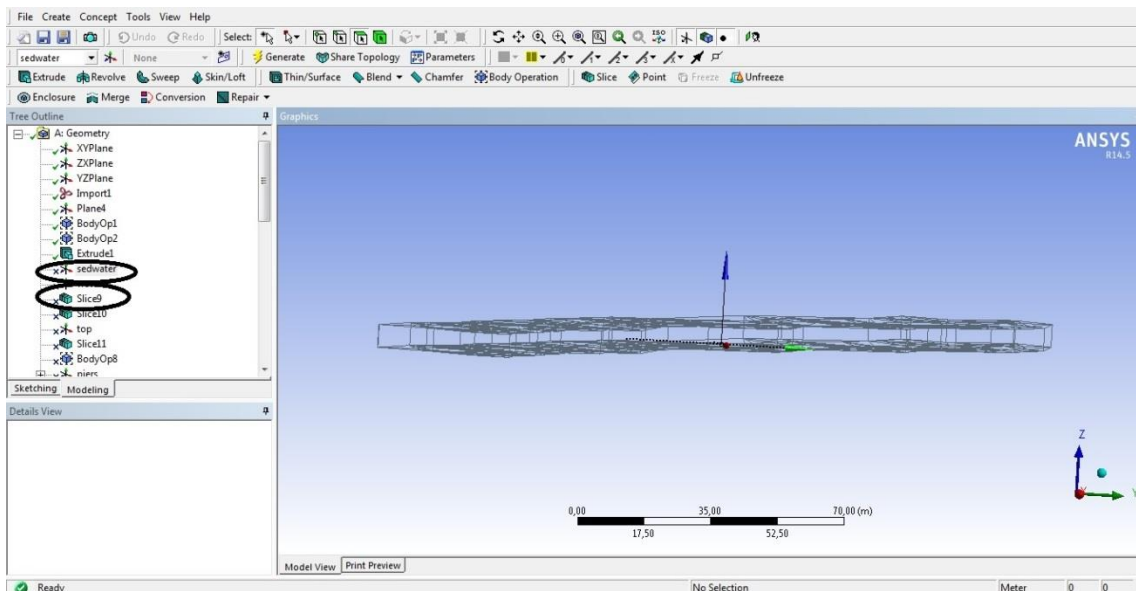


Figure 5.4. Generating of sediment body

Piers were generated via “delete” command. Pier walls were defined such that no fluid existed at the piers. Exact piers coordinates were put into place based on bridge data obtained from the State Hydraulic Works. B. Menderes. (Figure 5.5).

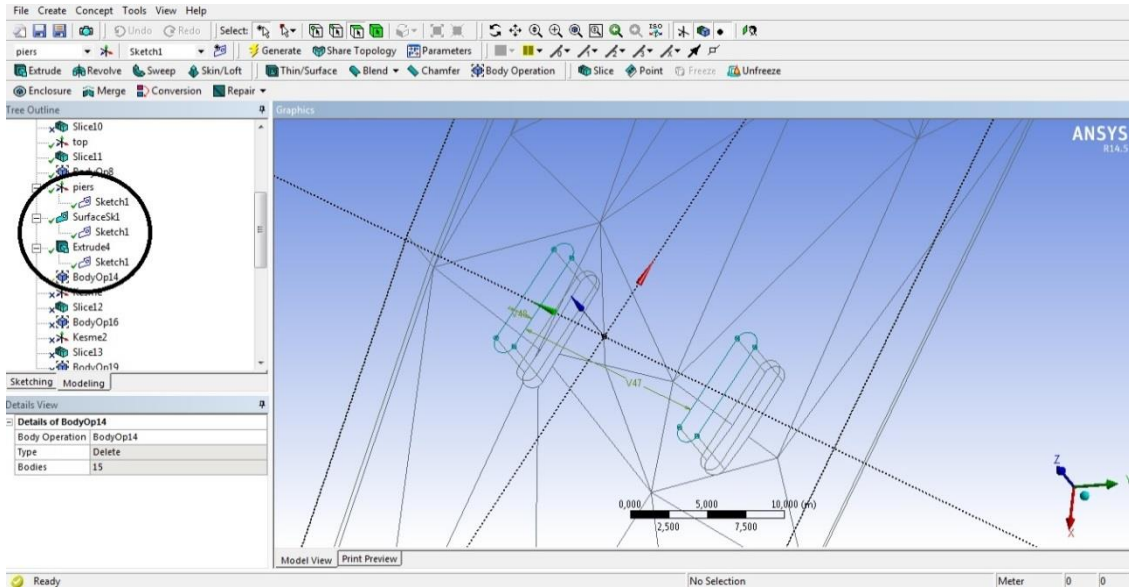


Figure 5.5. Generating of bridge piers

Finally, in order to overcome difficulties of meshing, acute angled triangles which are from 0,1 to 20 degree were suppressed via “repair sharp angle” command and short edges from 5 cm to 50 cm were fixed via “repair edge” command. After repairing angles and edges, all triangles were merged in the manner of soft via “merge” command (Figure 5.6).

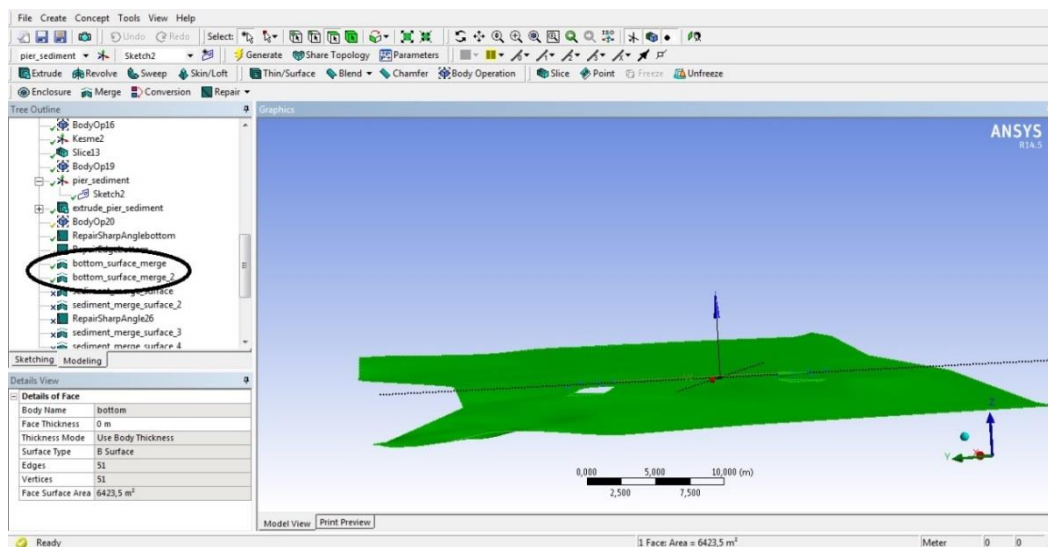


Figure 5.6. Merging of bottom surface in main domain

In Fluent solver, names of layers (water layer, sediment layer etc.) must be described along the creation of geometry and nodes. Otherwise, program cannot differentiate between the sediment layer and water layer and it causes vital problems. In order to prevent this, sediment layer and water layer were described and these two layer were combined by using “take part” command to provide connection between to layer while initial and boundary conditions were described (Figure 5.7).

To sum up, geometry was created via import and repair commands. Total width of geometry was nearly 40 m and total length of it was nearly 180 m. In order to mesh the geometry well and obtain adequate quality, total depth of sediment body was chosen as 0,8 m and total depth of water body was chosen as 3,7 m. Otherwise, the total depth of sediment layer becomes too low to mesh it easily and it becomes hard to obtain adequate quality. Further information about this issue will be provided later within the thesis.

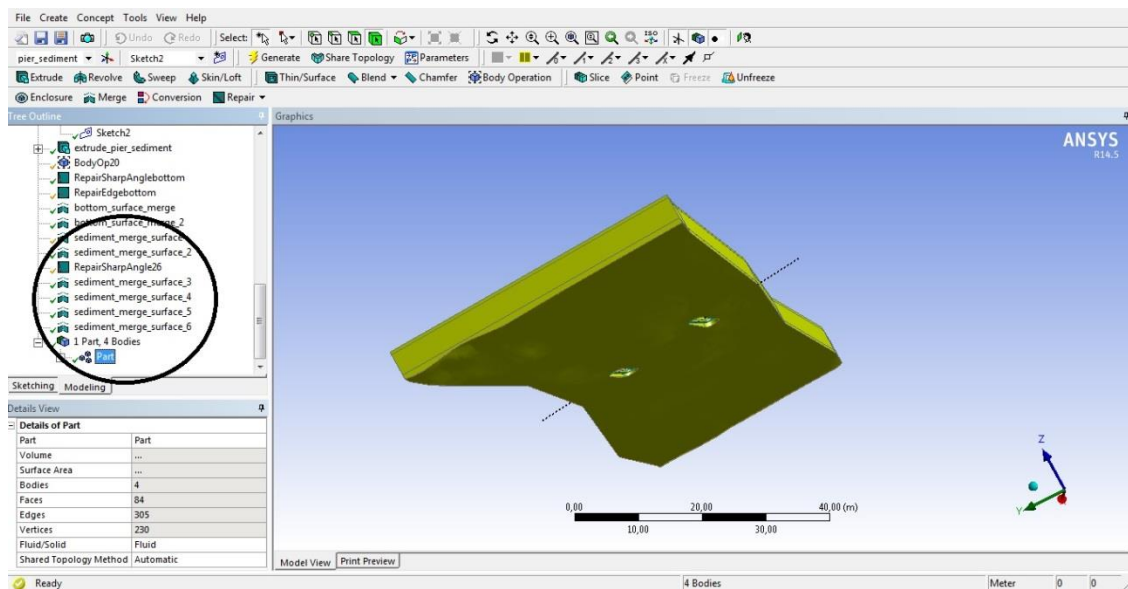


Figure 5.7. Named selection of main geometry in geometry window

5.1.2. Generating Mesh

The purpose of meshing is to separate the domain into a convenient number locations for obtaining accurate results. There are some different basic building-blocks of 3D mesh as given in Figure 5.8. Having appropriate mesh system is a convenience to solve the problem accurately, even if greater number of elements might require more

computational resources such as memory and processing time. The main aim should be to have sufficient number of elements to be solved in a desired time.

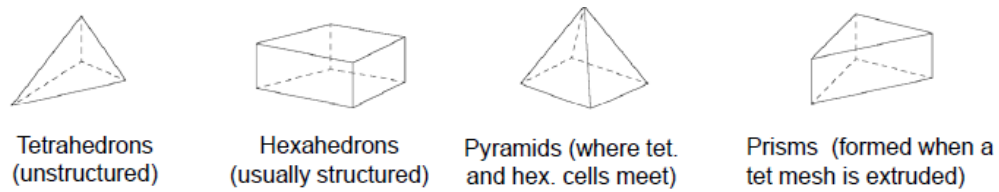


Figure 5.8. Different 3D mesh types [14].

As mentioned earlier, in complex geometrical bodies, mesh elements can be poor and it may cause poor quality results. Quality of mesh can be measured via “skewness”. Skewness is known as a measure of the relative distortion of an element compared to its ideal shape. It is scaled from 0 (excellent) to 1 (unacceptable) (Figure 5.9) [28].

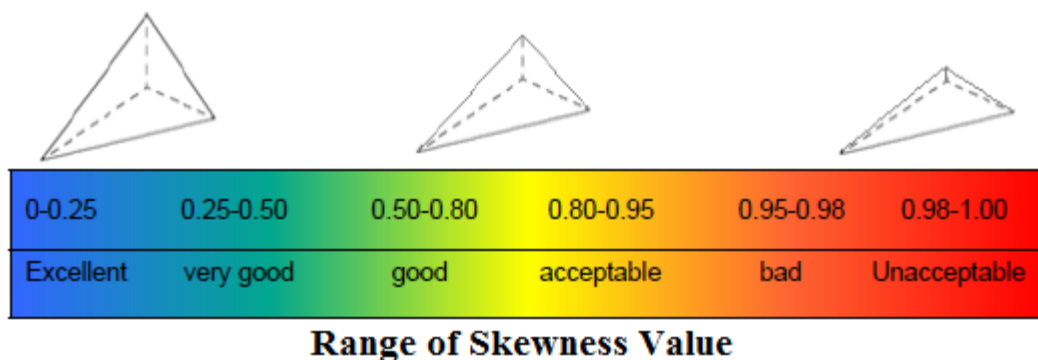


Figure 5.9. Quality scale of mesh [28]

In ANSYS, there are six different meshing systems in 3D bodies:

- i) Sweep Meshing (most common and useful)
- ii) Tetrahedrons
- iii) Automatic
- iv) MultiZone
- v) CFX-Mesh
- vi) Hex Dominant

Since sweep method is the most common and useful meshing method among all of them, it is widely utilized within this study. For the details of these methods, the reader is referred to “ANSYS Training Manual”.

In sweep method, hexes and/or prisms element shapes are produced (Figure 5.10) and body must be sweepable. In this thesis, the sweep method is used for the whole domain except near the bottom surface due to its unsweepable and rough shape. In order to overcome this problem, sediment body was sliced into two parts to separate smooth surface and rough surface. Thus, sweep method was applied in separated body having smooth surface and mesh quality was further enhanced (Figure 5.11).

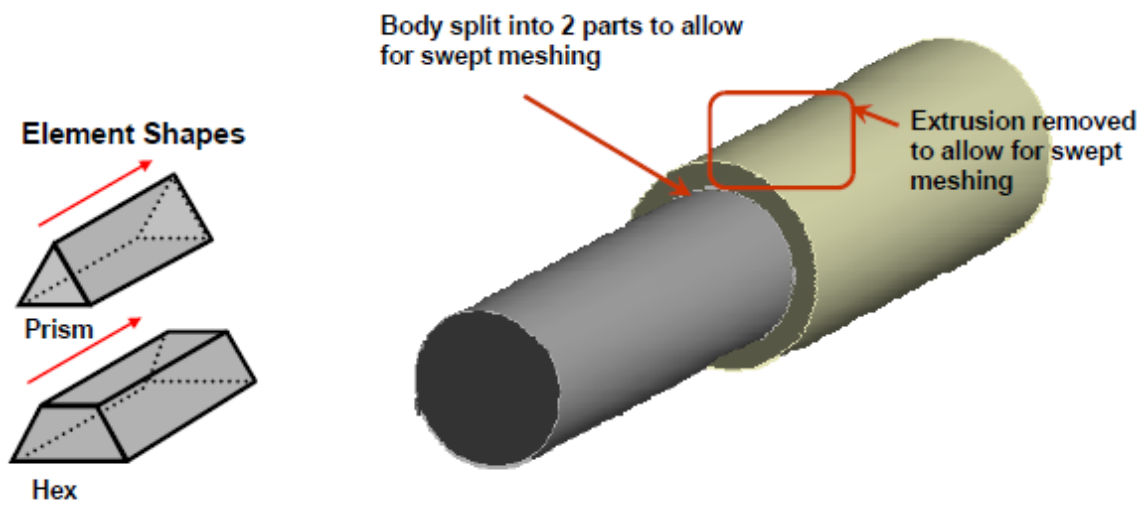


Figure 5.10. Prism / Hex Element shapes (left one) and a sweepable body (right one)

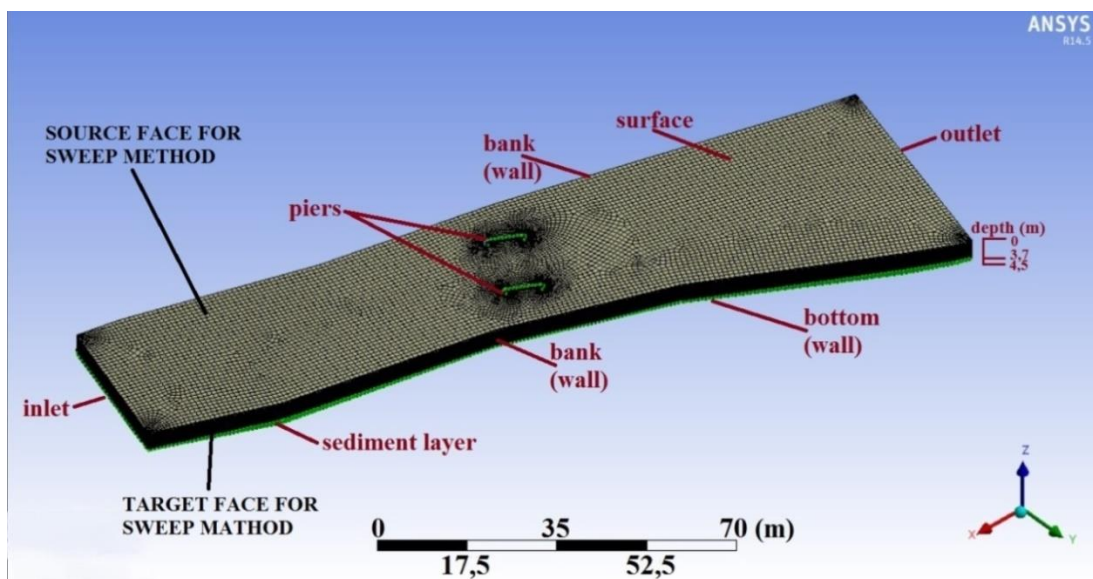


Figure 5.11. Source and target faces for sweep method in main geometry

On the other hand, “automatic method” was used for separated sediment body having rough surface (Figure 5.12).

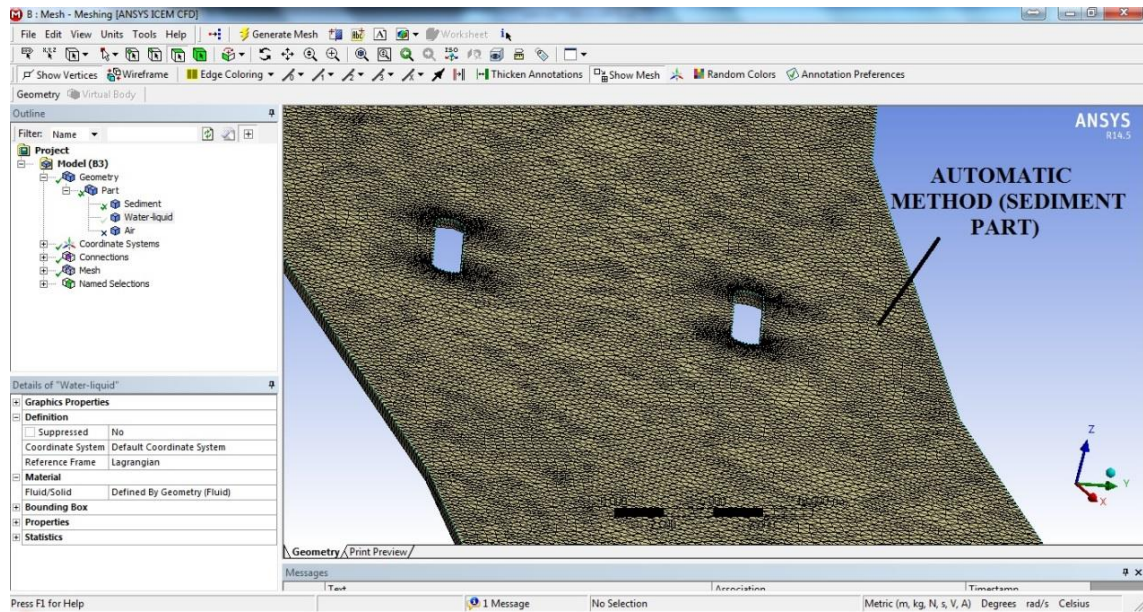


Figure 5.12. Automatic method for sediment layer

5.1.2.1. Mesh application on B. Menderes River geometry

After the body is transferred from “geometry” to “mesh”, it is necessary to describe the name of surfaces before transferring them to the Fluent solver. Side walls, sediment and water volumes, water surface and river bottom should be described before transferring them to the Fluent solver. While Figure 5.13 shows the described surfaces in mesh page, Figure 5.14 shows the main domain,

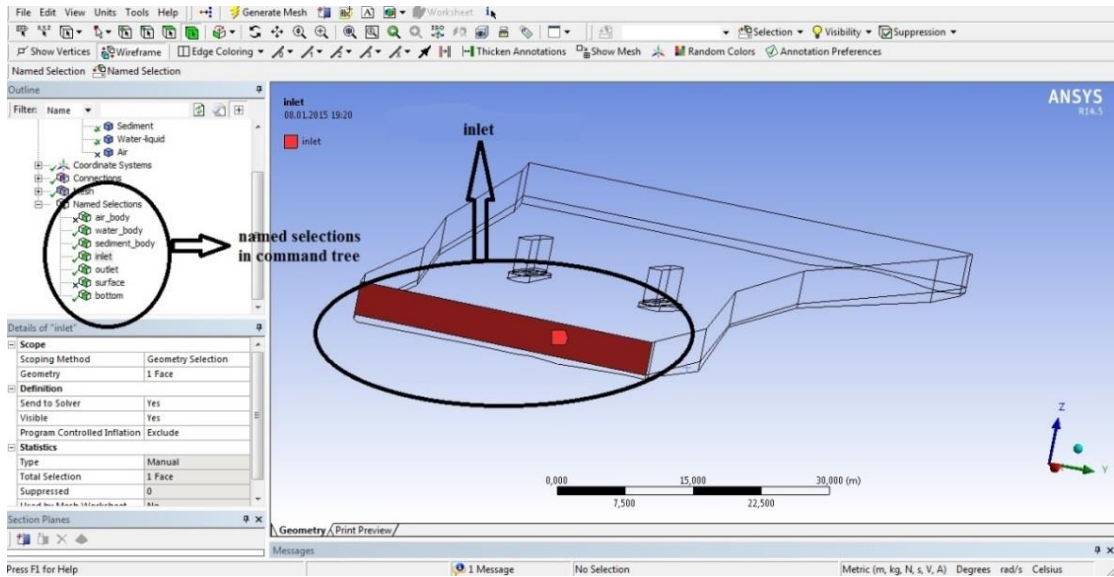


Figure 5.13. Named Selection for main geometry

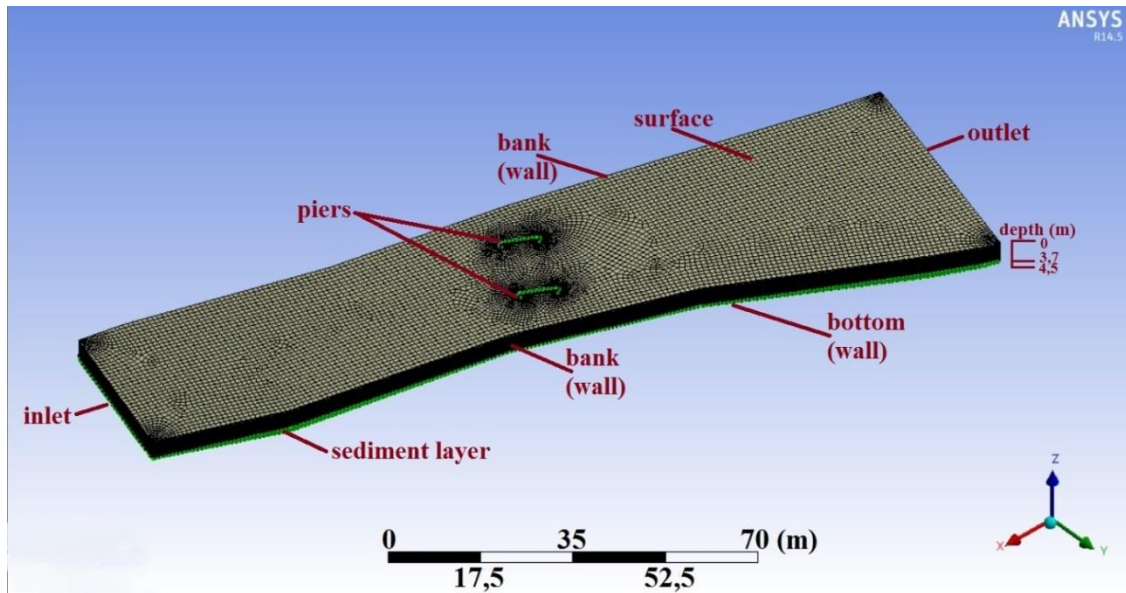


Figure 5.14. B. Menderes river domain in ANSYS

After the name selection, each edge was sized before meshing. In order to get adequate results, body is divided into smaller elements in $-z$ direction and near piers. It is impossible to choose inlet as a target face for sweep method due to uneven sides. Therefore, water surface is taken as a target face to mesh domain. This method follows linear way from target face to source face to sweep. Maximum cell size of unsweepable bottom body is chosen as 0,5 m for automatic method as well (Figure 5.15).

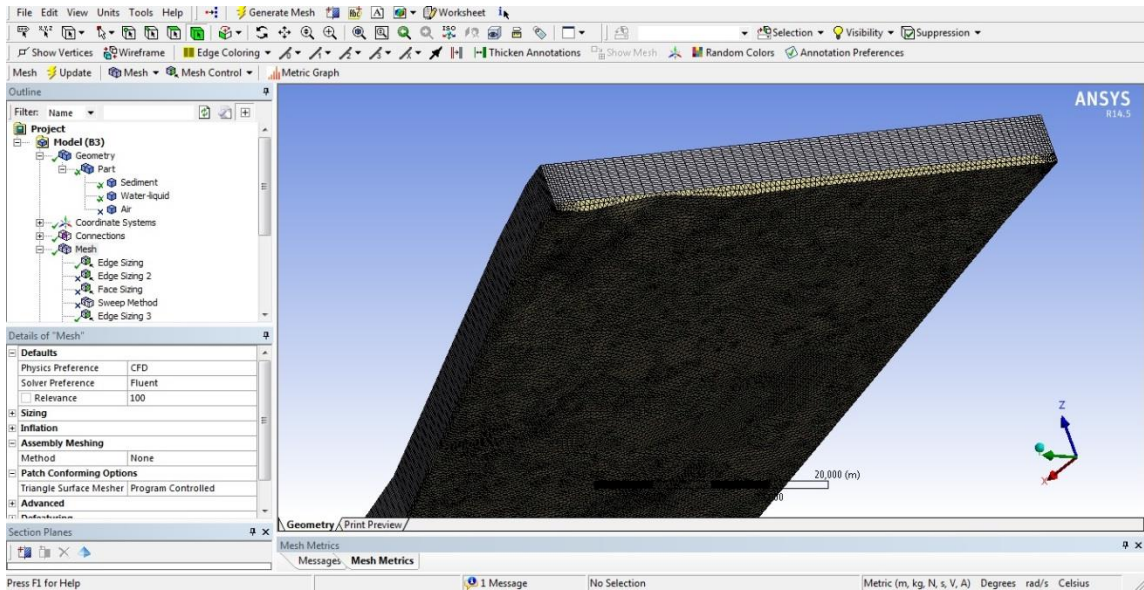


Figure 5.15. Water and sediment bodies

When mesh element quality is considered, maximum skewness value is obtained as 0,83 and maximum orthogonal quality is obtained as 0,22. These means that acceptable quality is provided to transfer Fluent solver to obtain good results (Figure 5.16). Not only plan view but also sectional view is necessary to understand and ensure mesh quality (Figure 5.17).

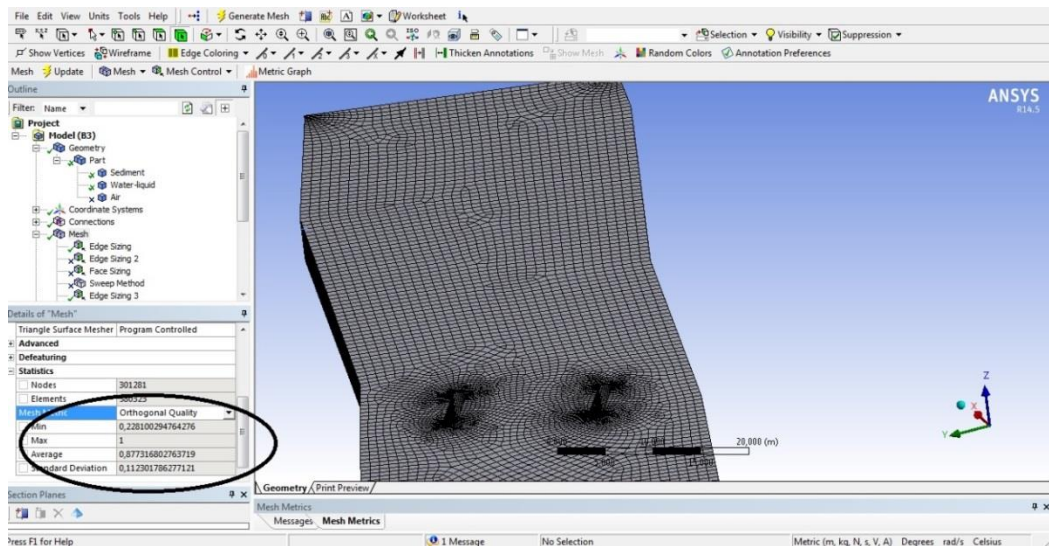


Figure 5.16. Mesh quality on main domain

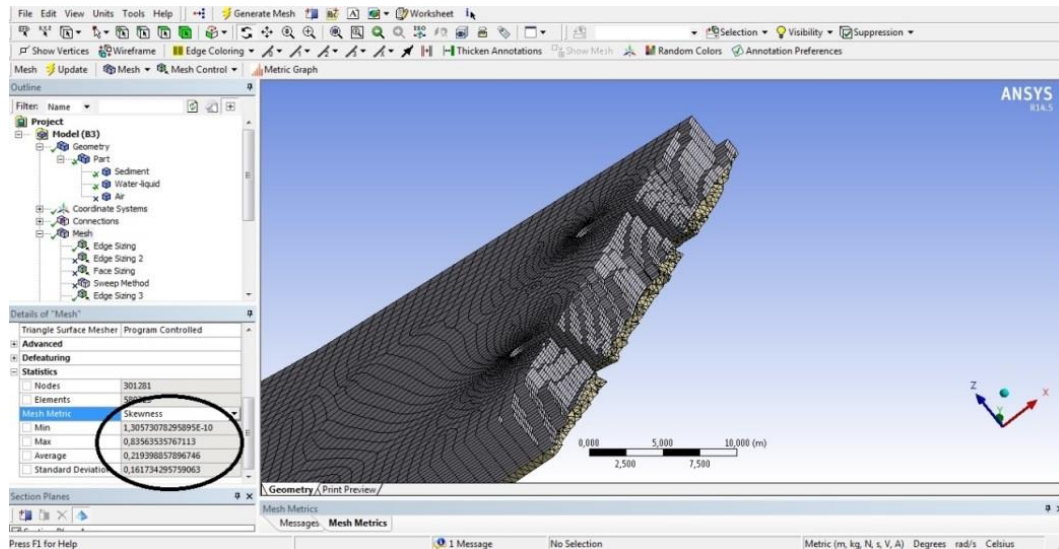


Figure 5.17. Sectional View of meshing

Consequently, the meshing was completed via sweep and automatic method and adequate nodes were obtained. In order to understand mesh conditions, Table 5.1 can be clarifying.

In contrast to main geometry, the sweep method was applied to both water and sediment bodies due to smooth geometry of simple domain. “Bias type” feature which is useful where nodes need to be clustered on an edge or group of edges was selected for in the sweep method since, near the side walls were not as important as middle of domain in our simulations

The mesh properties of the main and the simplified domains are provided by Table 5.1.

Table 5.1. Geometry and mesh properties for the main domain

	MAIN DOMAIN			SIMPLE DOMAIN		
	Water Body	Sediment Body	General	Water Body	Sediment Body	General
Total Length (m)	180	180	180	90	90	90
Total Width (m)	40	40	40	40	40	40
Total Depth (m)	3,7	0,8	4,5	3,7	0,8	4,5
Total Volume (m ³)	26640	5760	32400	13320	2880	16200
Method	Sweep	Automatic	-	Sweep	Sweep	-
Element Size (m) (width)	1	-	-	2,5	2,5	-
Element Size (m) (length)	-	-	-	2,25	2,25	-
Element Size (m) (depth)	0,2	-	-	0,53	0,4	-
Face Sizing (m)	1	-	-	-	-	-
Body Sizing (m)	-	0,5	-	-	-	-
Nodes	-	-	301281	-	-	8170
Elements	-	-	580323	-	-	6804
Min. Orthogonal Quality	-	-	0,228	-	-	1
Max. Orthogonal Quality	-	-	1	-	-	1
Min. Skewness Quality	-	-	1,31E-10	-	-	1,31E-10
Max. Skewness Quality	-	-	0,836	-	-	1,31E-10

5.2. Initial and Boundary Conditions

After mesh application, domains were transferred to Fluent solver to define conditions under different cases.

5.2.1. Simulation of a Simple Water Column without Sediment Layer in Order to Analyze Different Turbulent Models

Before simulation of the main domain and simple domain, the effects of applying different turbulence models were investigated in a simple water column. For these simulations $k-\epsilon$, $k-\omega$ and Reynolds turbulence models were utilized (Figure 5.18) [26].

The water column in front of the water intake was selected for the modeling purposes and initial/boundary conditions were selected based on measurements made in the Tahtalı Reservoir, İzmir. The geometry to be modeled was defined as 100 m by 200 m water column having 30 m depth. The intake structure was defined through a 2 m diameter fluid pipe and 9 m below the surface having a length of 200 m positioned at the middle of one side. Time step was taken as 0.005 s; number of time steps was selected as 14000 and maximum number of iterations was selected as 20 in the simulations. A view from the modeled site is given in Figure 5.19.

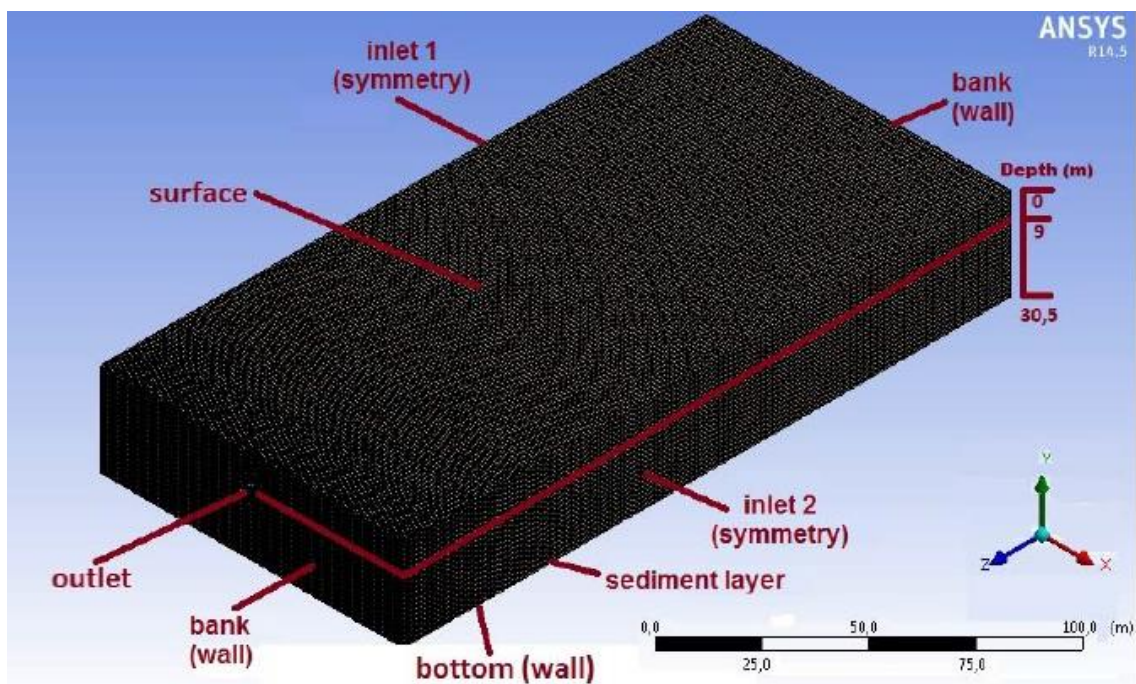


Figure 5.18. Tahtalı model domain utilized in ANSYS programme



Figure 5.19. A Google Earth view from the Tahtalı model domain selected

Side walls were defined as symmetry and velocity inlet (0,5 m/s and 1 m/s corresponding 1,5 and 3 m³/s of discharge) was applied to simulate the withdrawal in the model. Water density was assumed to depend only temperature, thus a formula describing the relationship between the water density and temperature is specified by a UDF in C language and this function is input into Fluent.

For simulations of maximum velocities, turbulence models performed pretty much the same as it is observed further away from the intake, when simulation of maximum velocity is concerned. At the intake, however, maximum withdrawal velocity for k- ω turbulence model was less than the other two turbulence models (k- ϵ and Reynolds) those gave the similar velocity values (Figure 5.20) (RMSE=0,03 m/s).

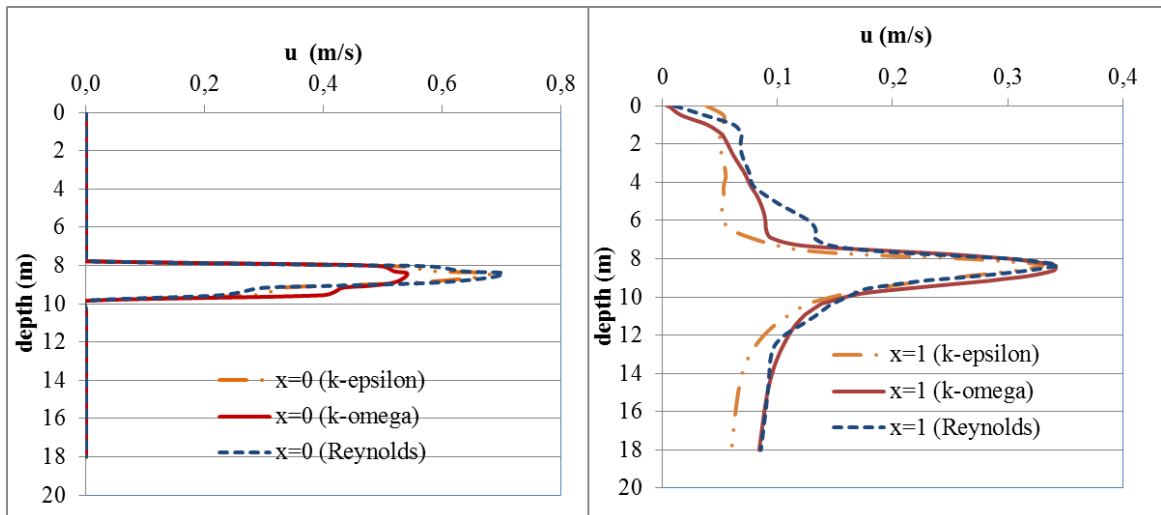


Figure 5.20. Comparison of velocities simulated using different turbulence models at the intake (at the left side) and 1 m far away from the intake (at the right side)

Velocities were also compared at different distances ($X= 0, 1, 2, 4, 10, 20$ and 30 m) from the intake (Figure 5.21 and Figure 5.22). Results of the simulations indicated a drawdown of the location of observed maximum velocities (from 6.9 to 8.8 m of depth measured from the surface) at all simulations. Drawdowns in each case were formulized through linear equations and the best match was obtained for the $k-\epsilon$ turbulence model ($R^2=0.97$).

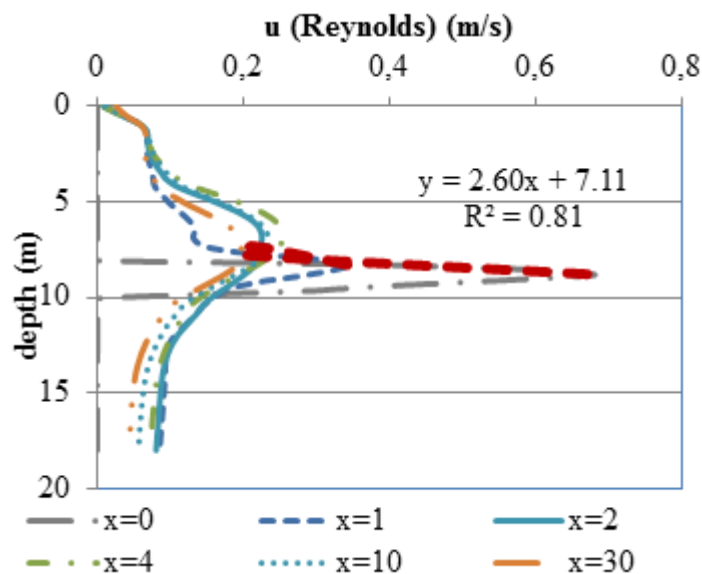


Figure 5.21. Velocities at different distances from the intake (Reynolds turbulence model).

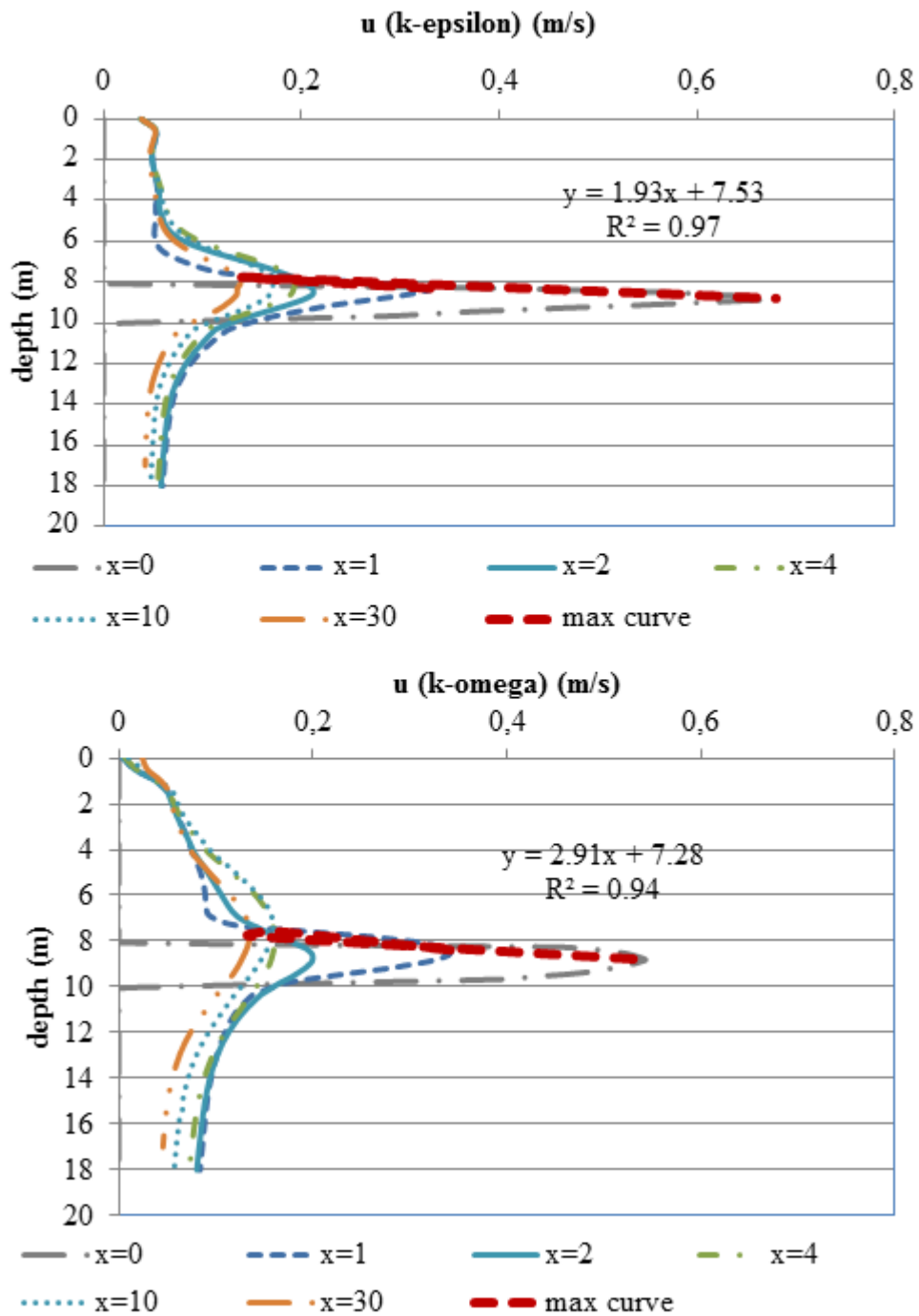


Figure 5.22. Velocities at different distances from the intake (k- ϵ and k- ω turbulence models).

In order to investigate the dynamics and reasons behind these results further, turbulent kinetic energy values nondimensionalized by maximum velocities were also calculated for the different turbulence models close to the intake structure. Calculated turbulent kinetic energy values at the intake were again slightly different for k- ϵ and

Reynolds turbulence models but were much less than turbulent kinetic energy values calculated by the $k-\omega$ model (Figure 5.23). Since $k-\omega$ turbulence model showed discrepancy from the other two models for prediction of flow velocity and turbulent kinetic energy at the intake, this discrepancy was attributed to the different wall treatments in the turbulence models. It is probably true to say that standard wall functions are generally applied for $k-\epsilon$ turbulence model and Reynolds stress models in these simulations, since these models are valid only far from solid boundaries. The $k-\omega$ model at the other hand solves the transport equations all the way to the wall through use of fine mesh.

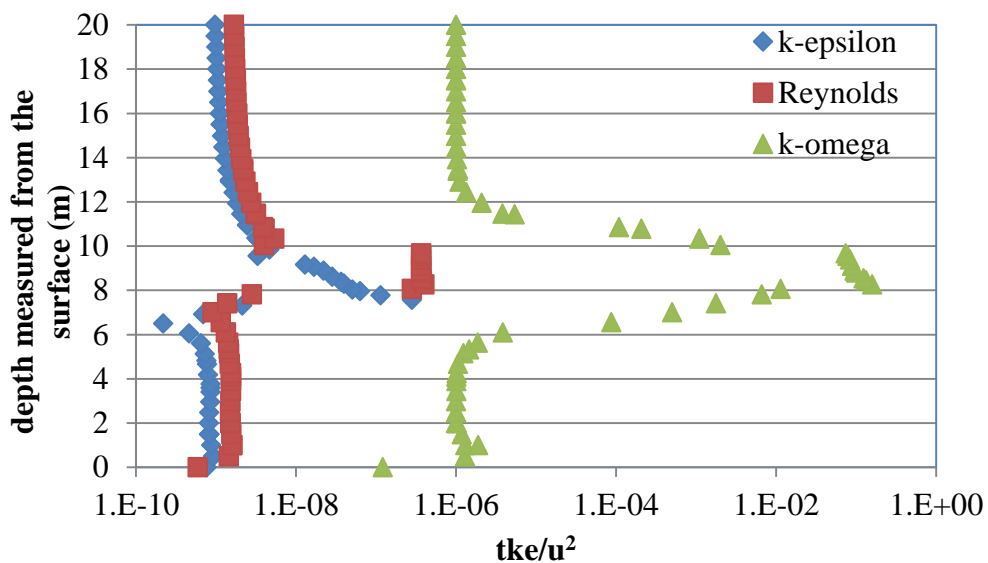


Figure 5.23. TKE/ u^2 values for $k-\epsilon$, $k-\omega$ and Reynolds turbulence models

Turbulent kinetic energy values are also plotted at the intake to include for the lateral distances ($Y = 47 - 53$ m). Figure 5.24 and Figure 5.25 show the difference of nondimensionalized turbulent kinetic energy values simulated by $k-\epsilon$ and Reynolds models and $k-\epsilon$ and $k-\omega$ models respectively. Figure 5.25 showed that turbulent kinetic energy values simulated by the $k-\omega$ model were much higher at the level of orifice. A pear shape difference was observed between the $k-\omega$ and $k-\epsilon$ models where the maximum difference was reached at 8.3 m depth measured from the surface. As it mentioned last paragraph, standard wall function is utilized for $k-\epsilon$ and Reynolds turbulence models.

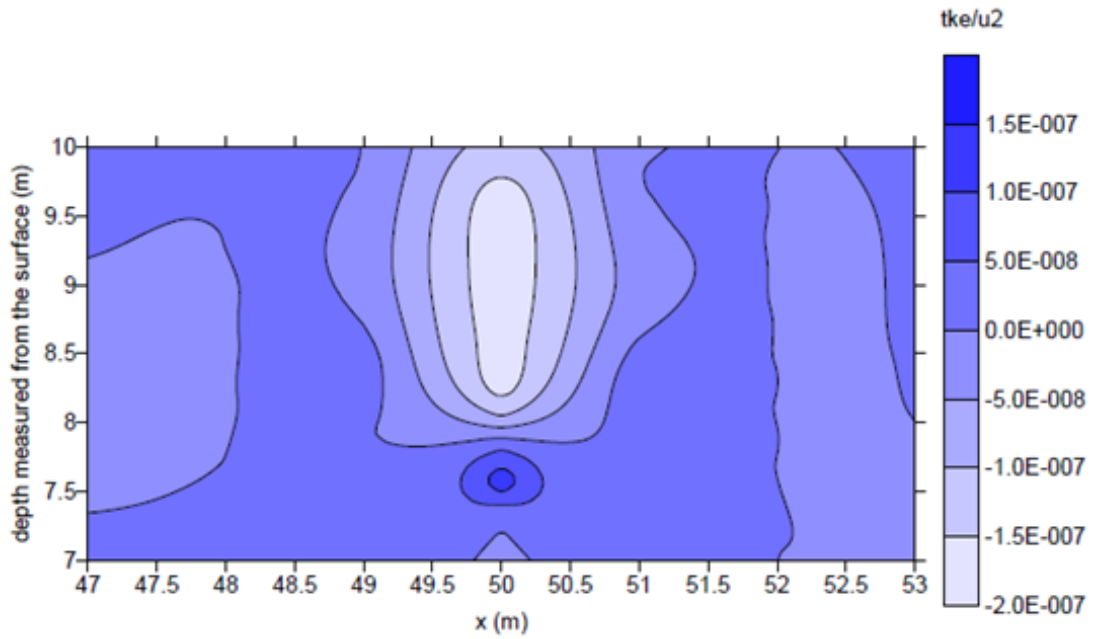


Figure 5.24. Difference of nondimensionalized turbulent kinetic energy values simulated by $k-\epsilon$ and Reynolds models (standard wall function) at the intake.

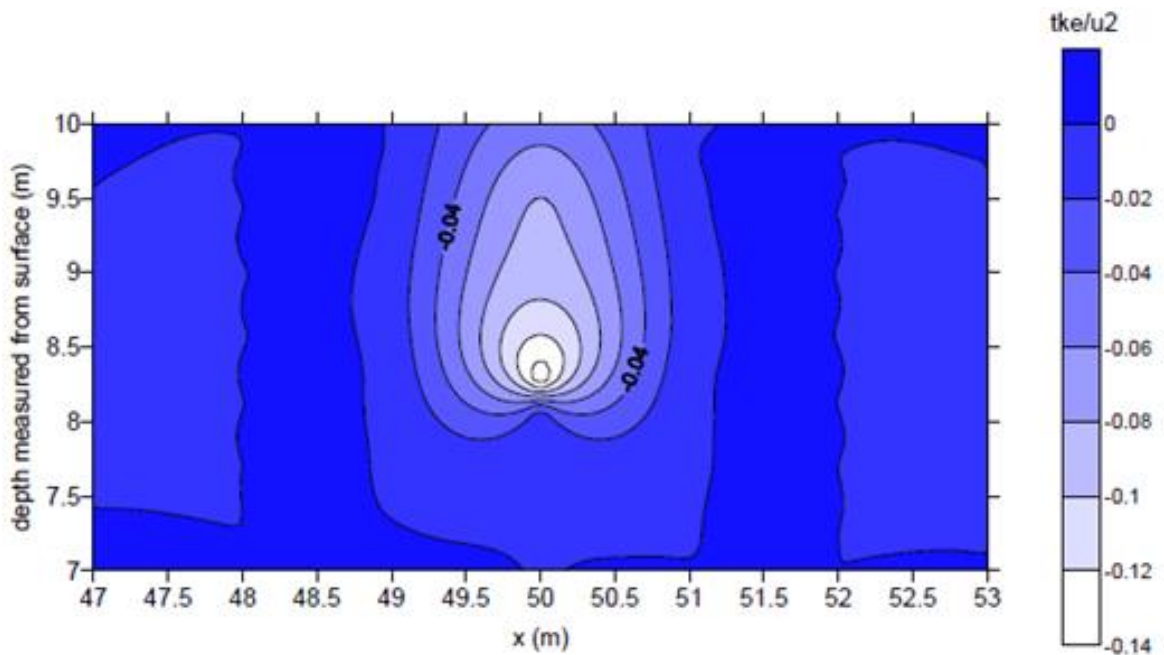


Figure 5.25. Difference of nondimensionalized turbulent kinetic energy values simulated by $k-\epsilon$ (standard wall function) and $k-\omega$ turbulence models at intake.

5.2.2. Simulation of Flow in B. Menderes River without Sediment Layer In Order To Analyze Different Turbulent Models

Based on the founding in the previous section, in this section, main domain (portion of B. Menderes River) was utilized to compare $k-\varepsilon$ and $k-\omega$ turbulence models. No sediment layer was considered and model was run with just one phase (water phase). Initial velocity was 0,257 m/s for constant discharge. Peak velocity was 1,1 m/s for hydrograph. In first 250 s, initial velocity was constant while initial velocity was rising in second 250 s. For hydrograph, an UDF (Appendix A) defining rising initial velocity after 250 s was interpreted.

In order to get adequate results, time step size should be less than ratio between minimum cell size and wavespeed [14]. Wavespeed can be assumed as 1,5 m/s and minimum cell size is 0,256. Considering this information Δt must be less than 0,17 s. Δt was assumed as 0,005 s for all simulations.

5.2.2.1. Results of Constant Flow Discharge

Figure 5.26 shows investigated point and line in main domain. Middle line located at the middle of water body from bottom to surface was investigated considering velocity magnitude. Then, point located at middle of water body was investigated considering velocity magnitude. Velocity inlet and pressure outlet were chosen as boundary conditions of inlet and outlet. Second Order (Momentum and Transient Formulation) was applied as solution method and time step of 0,005 s was used in all simulations.

Finally, graphical results were examined. Results showed that there were inconsiderable differences between $k-\varepsilon$ and $k-\omega$ in respect to velocities like investigation of Tahtalı Reservoir.

While longitudinal flow velocity was reached to 0,257 m/s for both $k-\varepsilon$ and $k-\omega$ turbulence models (Figure 5.27), vertical velocity showed discrepancy (Figure 5.28). Water was moving towards to surface with velocity being 0.015 cm/s at 150 cm below the surface. In contrast to it, vertical velocity was 0.015 cm/s at 400 cm below the surface. Profile of lateral velocity showed similarity with profile of longitudinal velocity at investigated line (Figure 5.29). It was 9 cm/s for both $k-\varepsilon$ and $k-\omega$ turbulence models.

Figure 5.30 shows velocity magnitude of water phase of investigated point for both $k-\epsilon$ and $k-\omega$ turbulence models.

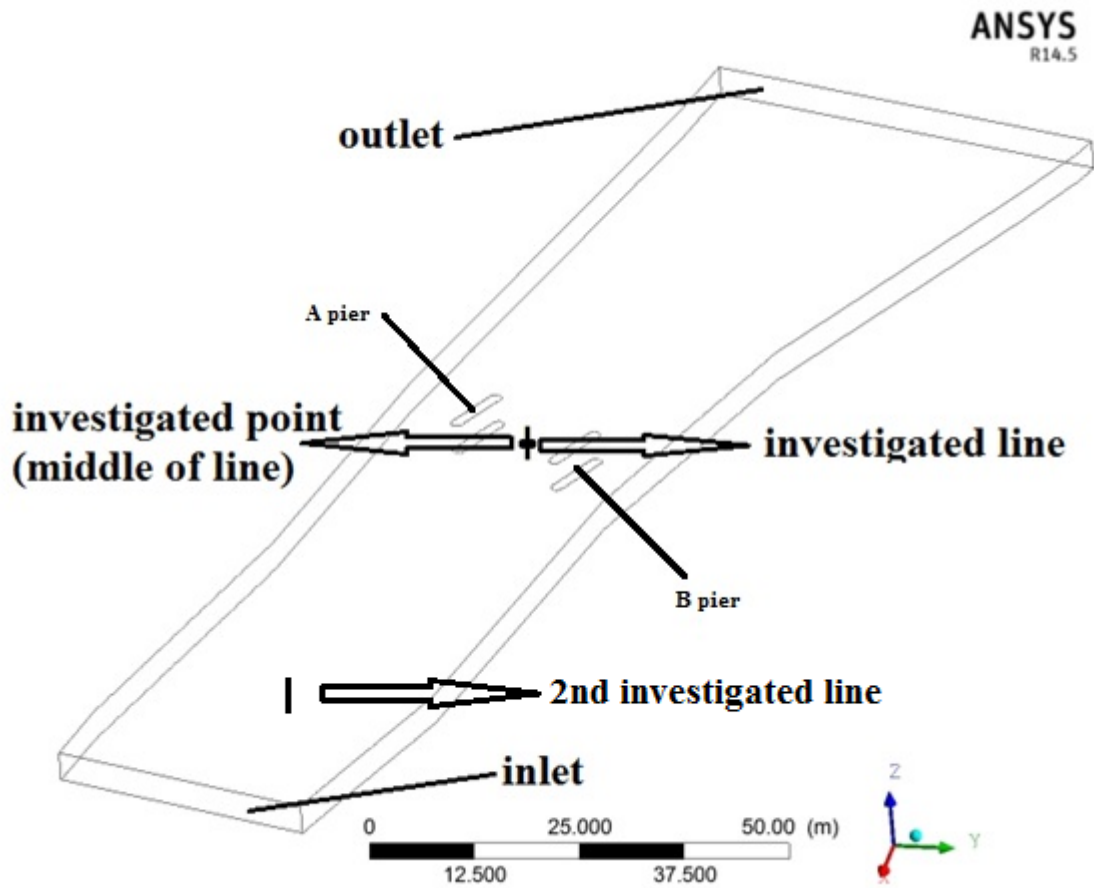


Figure 5.26. Investigated line and point on main domain

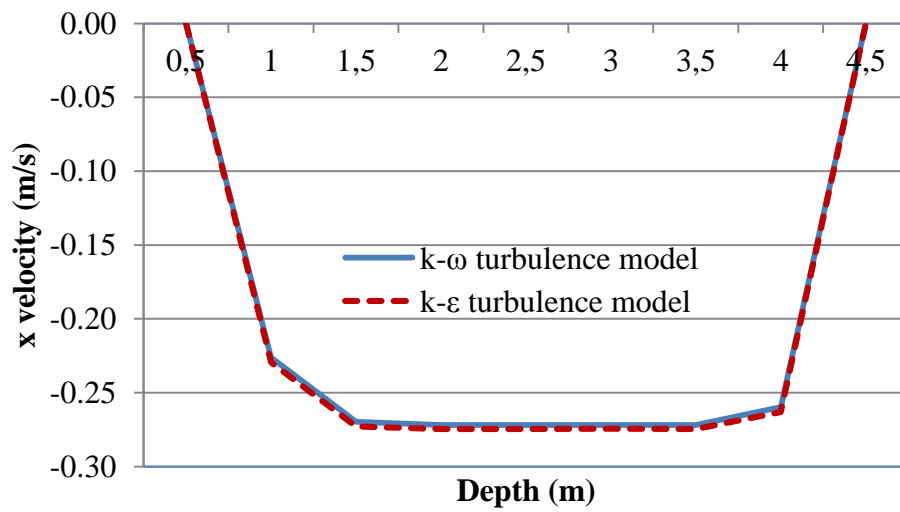


Figure 5.27. Longitudinal velocities on investigated line for both $k-\epsilon$ and $k-\omega$ turbulence models.

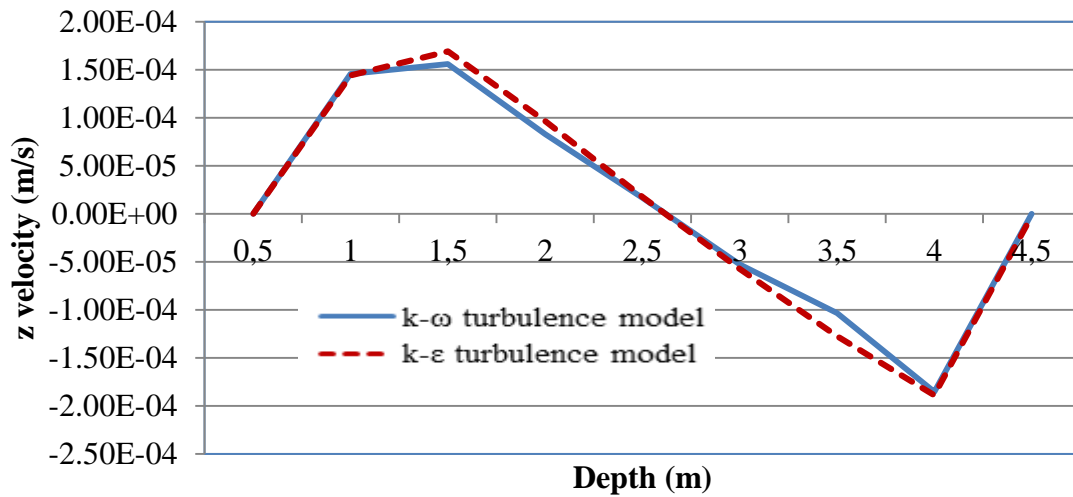


Figure 5.28. Depth-averaged velocities on investigated line for both k- ϵ and k- ω turbulence models.

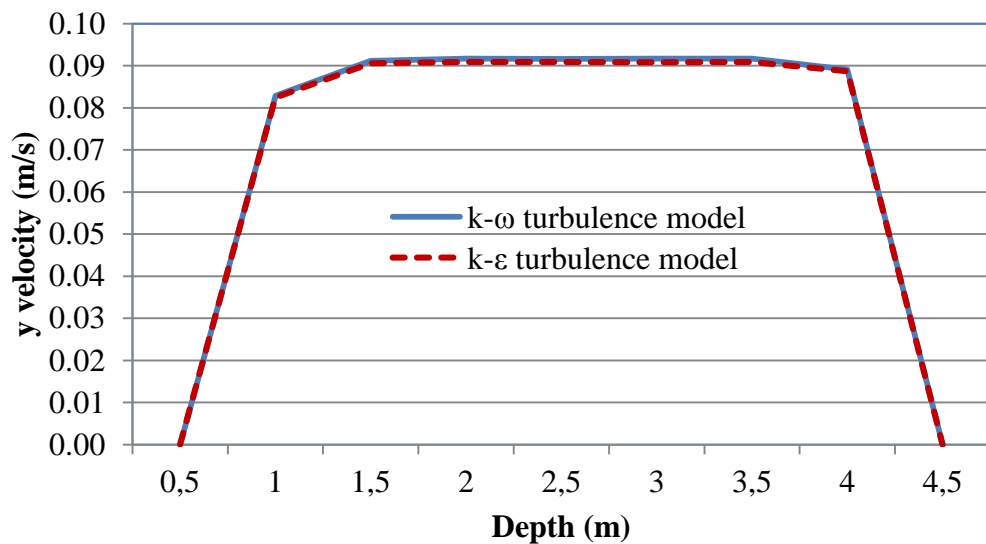


Figure 5.29. Lateral velocities on investigated line for both k- ϵ and k- ω turbulence models.

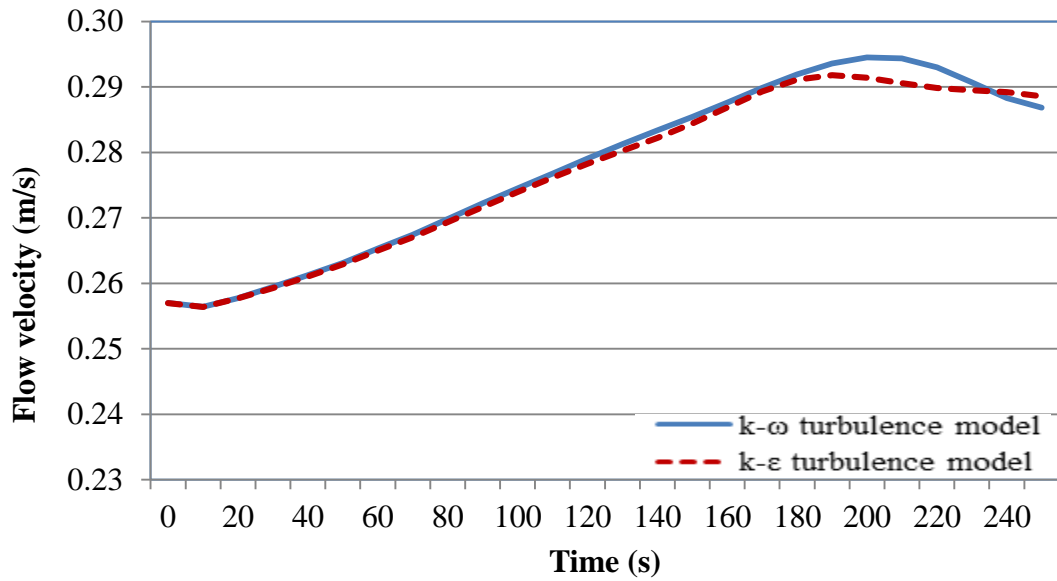


Figure 5.30. Velocity magnitude at investigated point for both k- ϵ and k- ω turbulence models.

Investigated contours considering flow velocities at $t=50$ s showed that effects of both k- ϵ and k- ω turbulence models were nearly same for 0,257 m/s initial flow velocity. Due to flow direction and meandering effect of the domain modeled, left of left pier was affected more than right of right pier. Maximum velocity reached to 0,298 m/s on the left side of middle plane, while it reached to nearly 0,266 m/s on the right side of middle plane (Figure 5.31).

When volume rendering was plotted for flow velocity, both k- ϵ and k- ω turbulence affected the flow in a similar way except a breakage after left pier of k- ω turbulence model was observed (Figure 5.32). As it mentioned before, k- ω turbulence model solves the equations of motion to the wall whereas the k- ϵ equation uses a wall function near the boundaries.

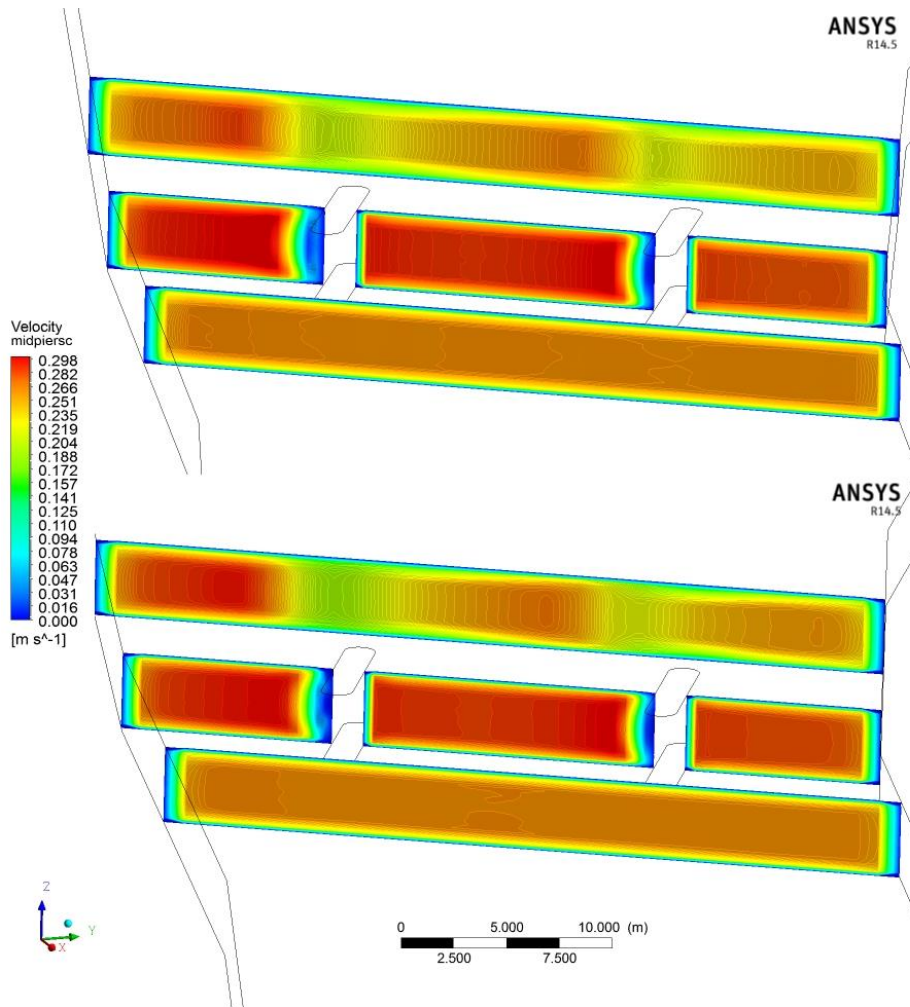


Figure 5.31. Longitudinal velocity contours on investigated planes for both $k-\epsilon$ (above) and $k-\omega$ (below) turbulence models.

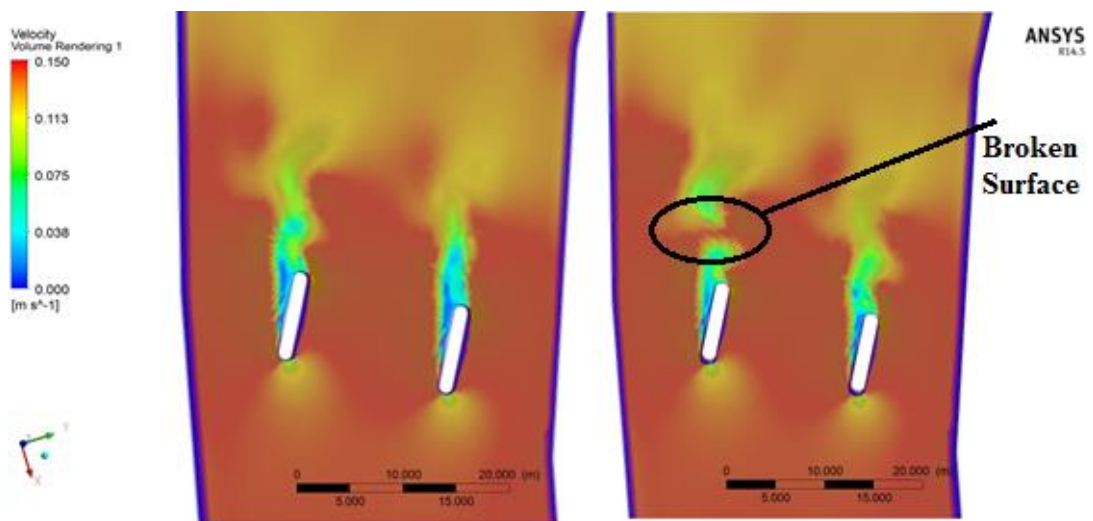


Figure 5.32. Volume rendering of Longitudinal velocities for both $k-\epsilon$ (left) and $k-\omega$ (right) turbulence models.

Investigated contours considering turbulence kinetic energies at $t= 50$ s showed that effects of both $k-\epsilon$ and $k-\omega$ turbulence models were different. It was shown that, simulated of turbulence kinetic energy near piers considering $k-\omega$ turbulence model was higher than the turbulence kinetic energy simulated by the $k-\epsilon$ turbulence model. While turbulence kinetic energy was approximately $0,002 \text{ j/kg (m}^2/\text{s}^2)$ near “pier B” for the simulation done by the $k-\omega$ turbulence model, TKE was approximately $0,001 \text{ j/kg}$ near “pier B” for the $k-\epsilon$ turbulence model (Figure 5.33).

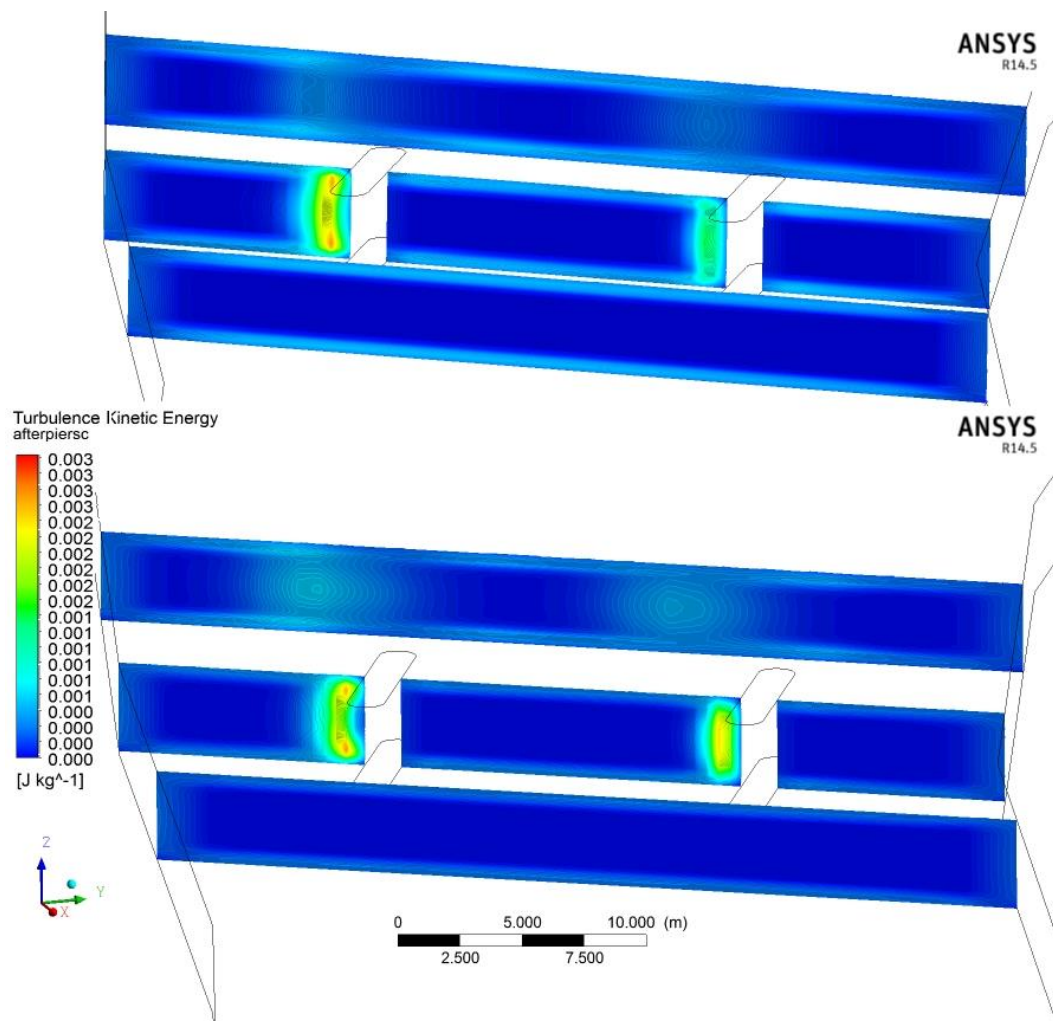


Figure 5.33. TKE contours on investigated planes for both $k-\epsilon$ (above) and $k-\omega$ (below) turbulence models.

When the results were also plotted via volume rendering of the turbulent kinetic energy, fluctuations near piers were more for the case of $k-\omega$ turbulence model than the $k-\epsilon$. Figure 5.34 shows a zoomed in view of showing the fluctuates near piers. Maximum observed TKE was nearly same both $k-\epsilon$ and $k-\omega$ turbulence models. A photo

taken at the field during the observations show an agreement between the simulated and observed turbulence effects downstream of the piers (Figure 5.35).

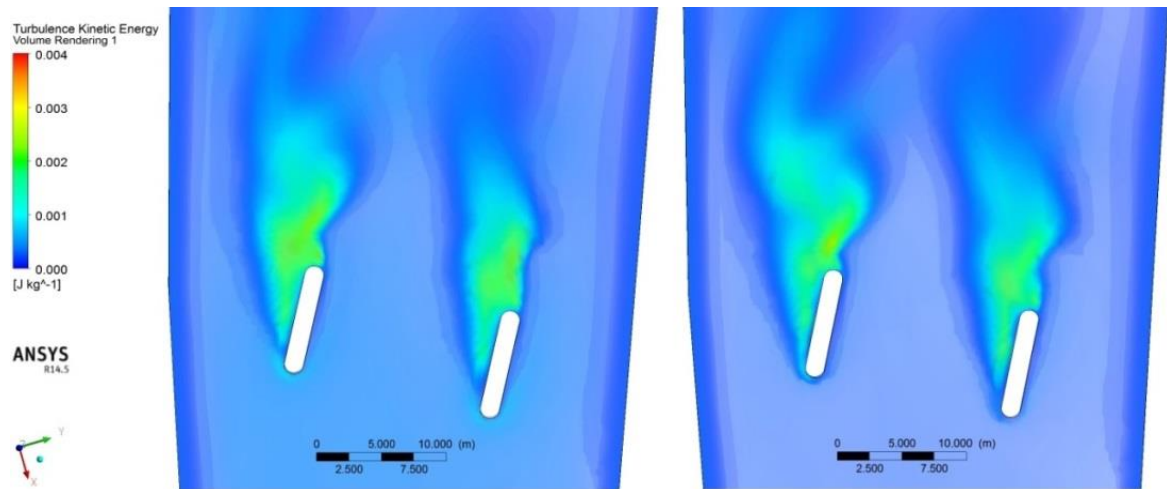


Figure 5.34. Volume rendering of TKE for both k- ϵ (left) and k- ω (right) turbulence models



Figure 5.35. A view of turbulence effect of piers on B. Menderes River

5.2.2.2. Results of Hydrograph

In this section, all initial and boundary conditions were kept the same except a hydrograph was simulated instead of a constant flow rate in this case. Again, initial water velocity was defined via UDF (Appendix A) where for the first 250 s, constant velocity was defined as initial boundary condition and then water velocity was raised to 1,1 m/s for the next 250 s at the inlet surface.

Results showed that there were again negligible differences between the simulations of longitudinal and transverse velocities for $k-\varepsilon$ and $k-\omega$ turbulence model simulations when a hydrograph was applied instead of a constant flow rate at the velocity inlet (Figure 5.36 and Figure 5.37).

Vertical velocity showed more discrepancy than the transverse and longitudinal velocities due to rising water velocity at the inlet. Water was moving towards to surface with velocity being 0,1 cm/s at 150 cm below the surface. In contrast to it, vertical velocity was 0,1 cm/s at 400 cm below the surface. Differences between result of $k-\omega$ and result of $k-\varepsilon$ were more than the differences observed for the constant flow rate. These differences reached 0,016 m/s at peak points (Figure 5.38). Profile of lateral velocity showed similarity with profile of longitudinal velocity at investigated line. It was 40 cm/s for both $k-\varepsilon$ and $k-\omega$ turbulence models and Figure 5.39 shows velocity magnitude for both $k-\varepsilon$ and $k-\omega$.

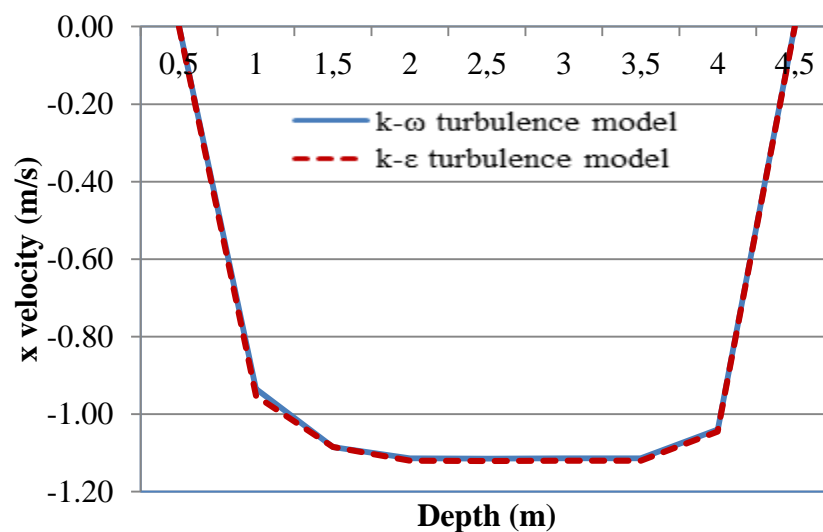


Figure 5.36. Longitudinal velocities on investigated line for both $k-\varepsilon$ and $k-\omega$ turbulence models (hydrograph)

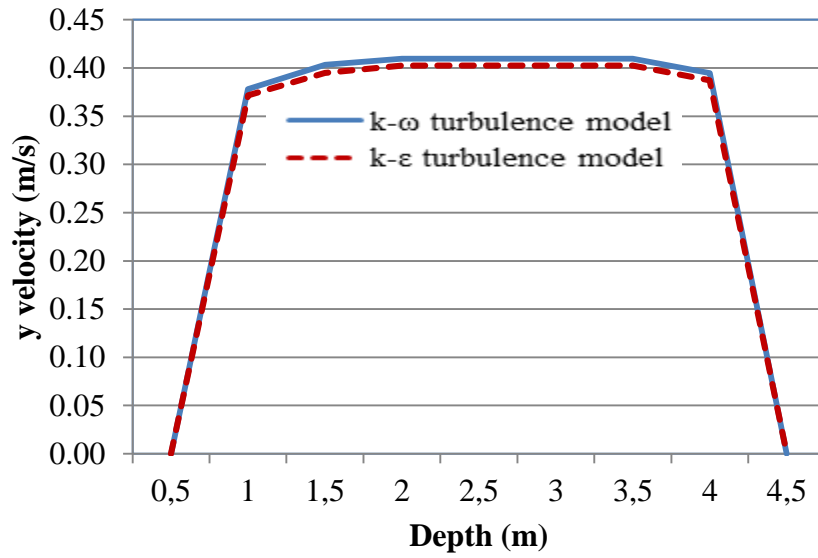


Figure 5.37. Lateral velocities on investigated line for both k- ϵ and k- ω turbulence models (hydrograph)

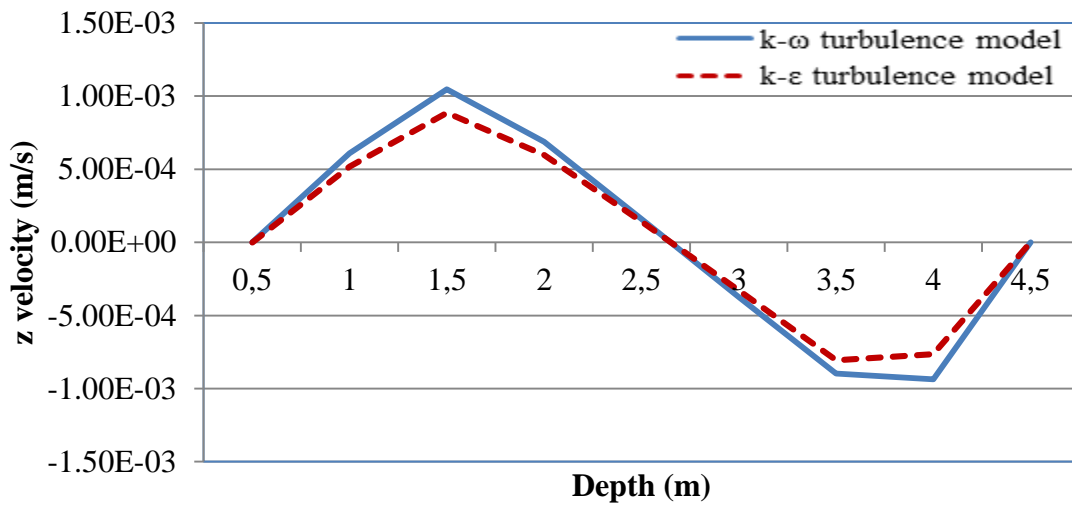


Figure 5.38. Depth-averaged velocities on investigated line for both k- ϵ and k- ω turbulence models (hydrograph)

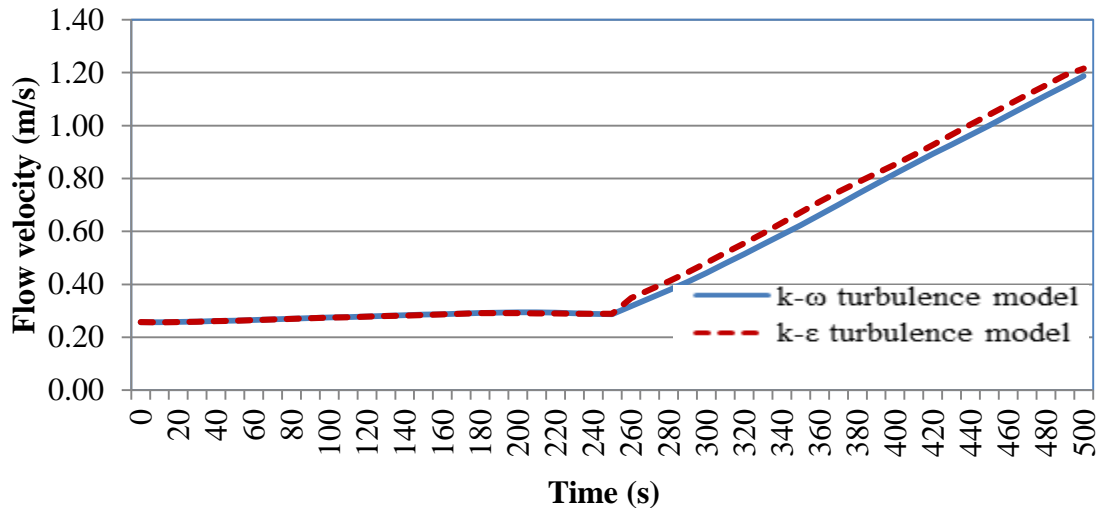


Figure 5.39. Velocity magnitude at investigated point for both k- ϵ and k- ω turbulence models (hydrograph)

Investigated contours considering turbulence kinetic energies at $t=50$ s showed that effects of k- ϵ and k- ω turbulence models were completely different near piers. Results indicated that, simulated turbulence kinetic energy near piers considering k- ω turbulence model was more than the turbulence kinetic energy simulated near piers considering k- ϵ turbulence model. In contrast to k- ϵ , effect of turbulence was observable at third plane located after piers in k- ω turbulence model. While turbulence kinetic energy was rising until 0.063 j/kg near “pier A” in k- ω turbulence model, TKE was going up until 0.031 j/kg near “pier A” in k- ϵ turbulence model. Therefore, it can be said that the TKE simulated by the k- ω turbulence model was twice the TKE simulated by the k- ϵ turbulence model near pier A (Figure 5.40).

When volume rendering was plotted again, effects of both k- ϵ and k- ω were different. In k- ω turbulence model, influenced area near piers was more than other model (Figure 5.41 and Figure 5.42). TKE reached nearly 0.016 j/kg near piers in both k- ω and k- ϵ models

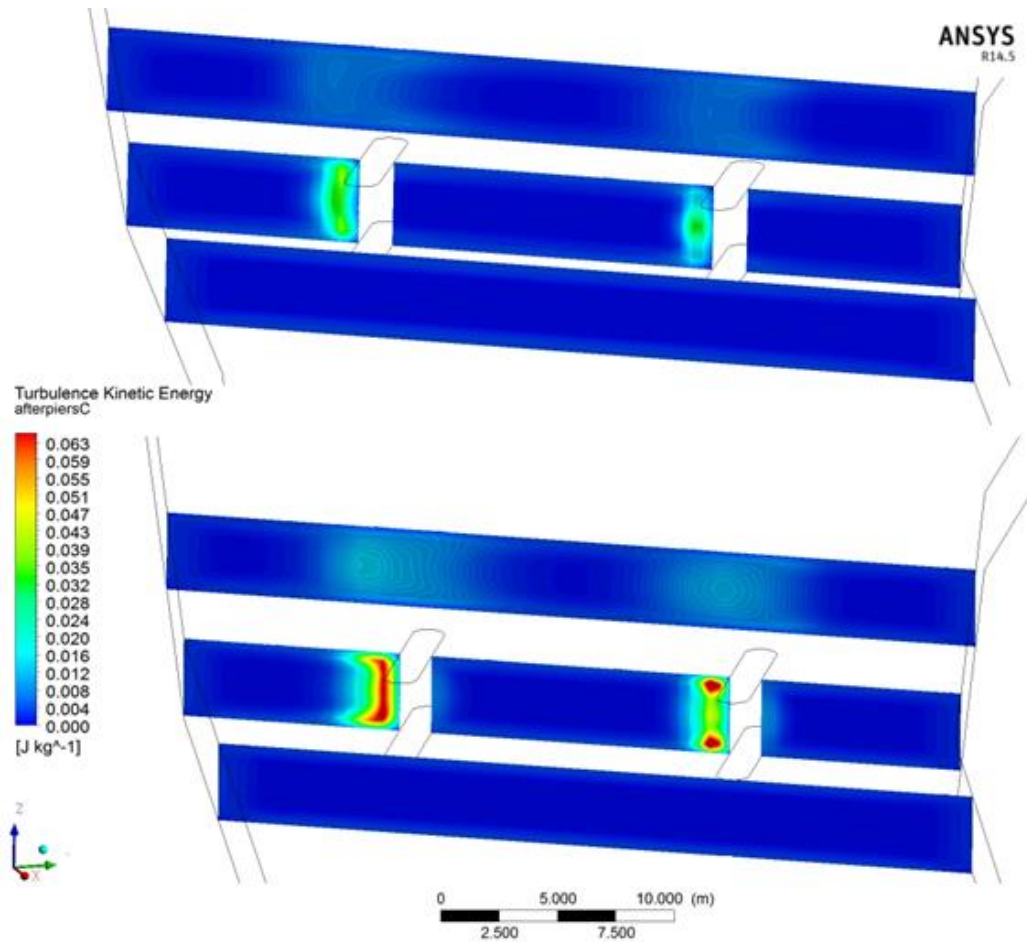


Figure 5.40. TKE contours on investigated planes for both $k-\epsilon$ (above) and $k-\omega$ (below) turbulence models.

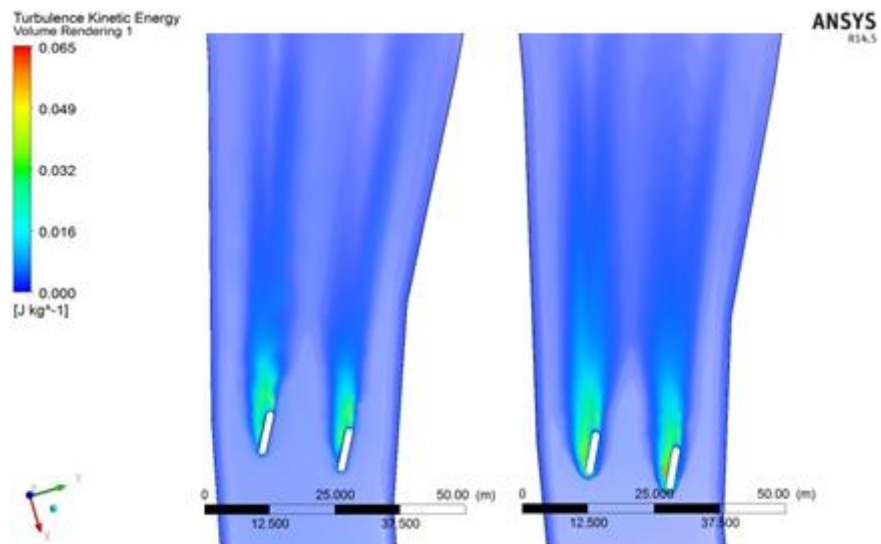


Figure 5.41. Volume rendering of TKE for both $k-\epsilon$ (left) and $k-\omega$ (right) turbulence models.

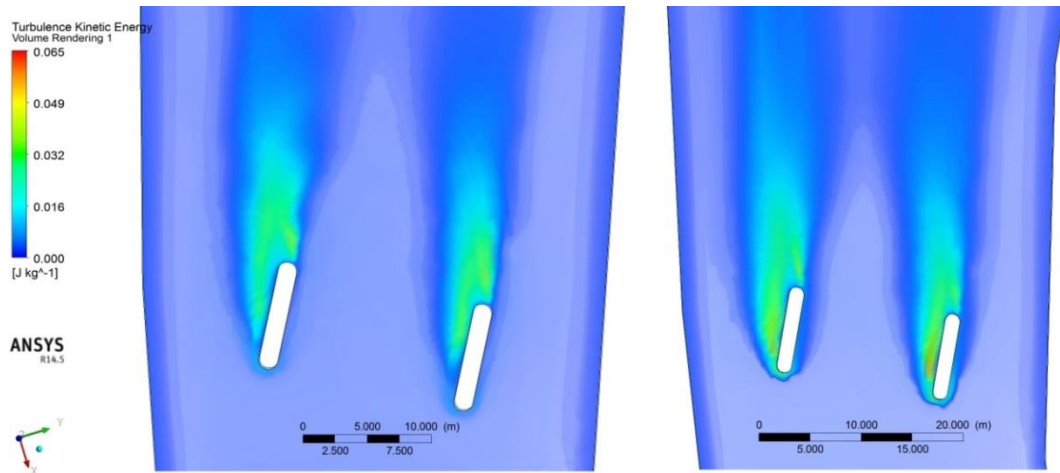


Figure 5.42. Volume rendering of TKE for both k- ϵ (left) and k- ω (right) turbulence models.

Plots of volume rendering (Figure 5.43) and longitudinal velocities in both contour (Figure 5.44) formats at time $t=50$ s indicated that k- ϵ and k- ω turbulence models had different effects on the velocities simulated near the piers. While shape of velocity contour near piers was concave in k- ϵ model, shape of velocity contour near piers was convex in k- ω model (Figure 5.44). In both models, maximum velocities were approximately 1,164 m/s. As mentioned before, in k- ω model, effects of turbulence was more significant than k- ϵ model.

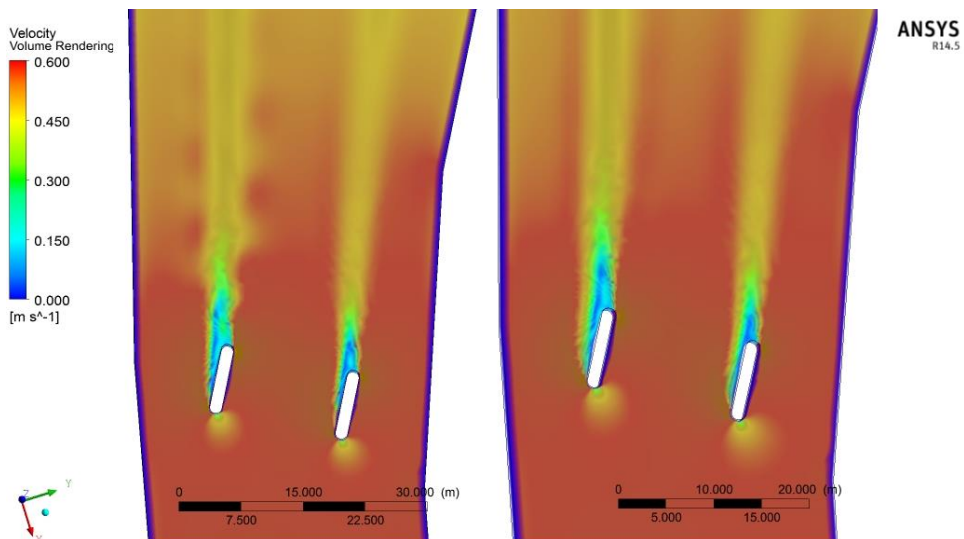


Figure 5.43. Volume rendering of Longitudinal velocities for both k- ϵ (left) and k- ω (right) turbulence models.

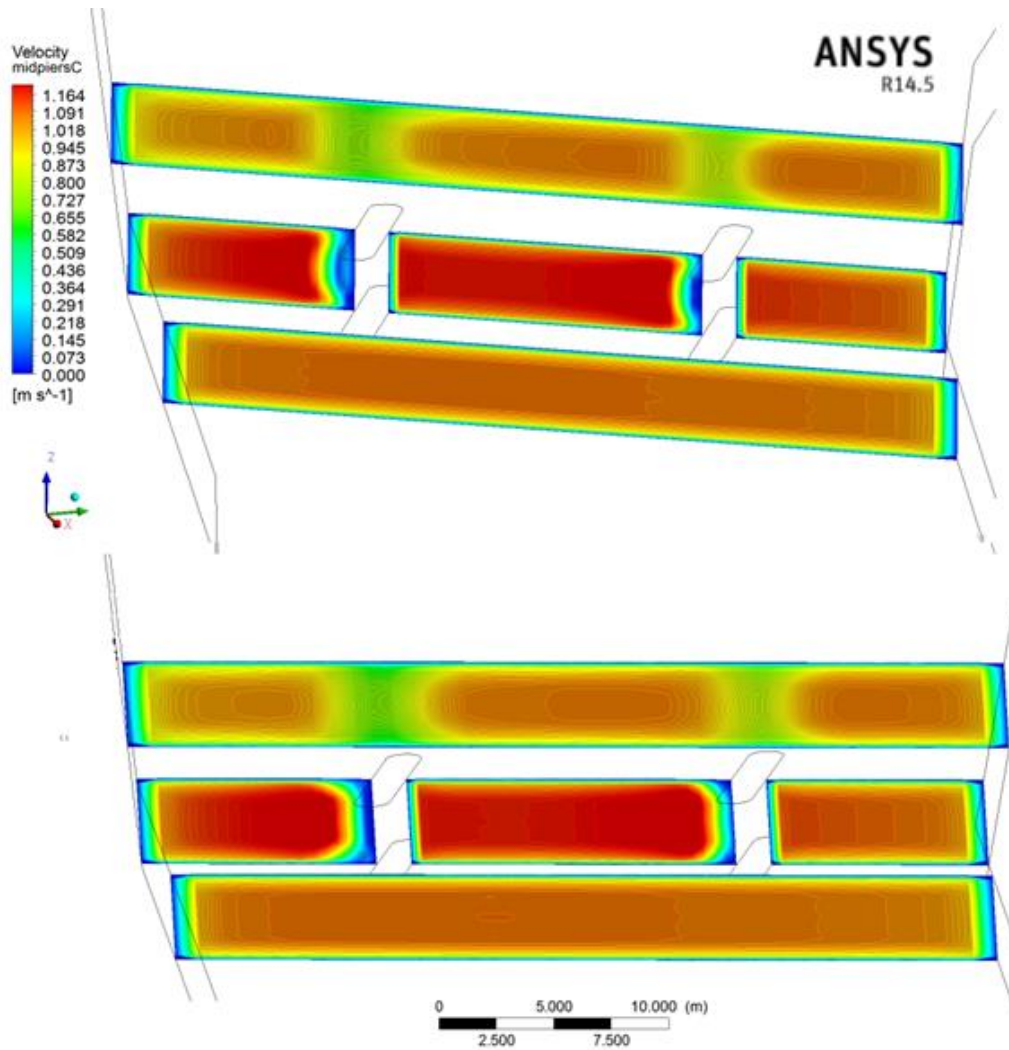


Figure 5.44. Longitudinal velocity contours on investigated planes for both $k-\epsilon$ (above) and $k-\omega$ (below) turbulence models.

5.2.3. Modeling of Particle Motion in a Simplified Model Domain

In this section, a simplified geometry was used to compare $k-\epsilon$ and $k-\omega$ turbulence models to investigate particle motions. Eulerian-Lagrangian method was used for this simulation. In order to simulate suspended sediment load, “Discrete Phase Method (DPM)” was used while “Eulerian Multiphase Method” was been used to simulate bed sediment load. Initial magnitude velocity was 1,4 m/s for inlet boundary condition and total simulation time was 70 s.

When general and boundary conditions were considered, inlet boundary condition was chosen as “velocity inlet” and 1,4 m/s. In contrast to it, outlet boundary condition was defined as “pressure outlet” and it was set to atmospheric pressure (0 pa).

Turbulence models $k-\epsilon$ with standard wall function and $k-\omega$ with standard wall function were utilized for comparison. Second order solution method was used for momentum and transient formulation. Time step size was taken as 0,005s as well.

5.2.3.1. Particle Motions Considering Uniform Diameter Distribution $k-\epsilon$ Turbulence Model with Standard Wall Function vs. $k-\omega$ Turbulence Model with Standard Wall Function)

In this section effects of sediment diameter and total mass of suspended sediment on sediment transport were investigated via simulations with three different particle diameters (0,001 mm, 0.003 mm and 0.005 mm) corresponding to the size of fine sediments observed at the study site and two different total mass ($C=11,31$ kg and 22,63 kg) selected based on the measurements. First model run with 0.001 mm median diameter for suspended sediment injected via DPM. “Two-way turbulence coupling” and “discrete random wall model” was activated to simulate interaction between water and injected particles better. Drag law was chosen as “spherical” used when particle shape is assumed spherical. Area-weighted average settling velocities of injected particles were investigated at plane located on 14 m far away from inlet surface (Figure 5.45). Then, time it takes to deposit was investigated considering different median diameters. At the beginning of simulation, all sediment particles were unsettled but then particles started to settle down within seconds.

The settling procedure at different times for particle diameter of 0,003 mm is given at Figure 5.46 for 22,62 kg total mass and at Figure 5.47 for 11,31 kg total mass respectively. Initial particle velocity and initial water velocity were 1,4 m/s. Under these conditions, large amount of particles arrived nearly middle of water body and small amount of particles settled down after 25 s. After 70 s, some of the particles were escaped from outlet surface and rest of them settled down. Owing to “reflect boundary condition” in DPM, some particles rolled away on the bottom surface after settling. “Reflect boundary condition” lead to that particle rebounds the off the boundary in question with a change in its momentum. Owing to it, there was not any settled sediment particle in the middle of first meters of bottom surface.

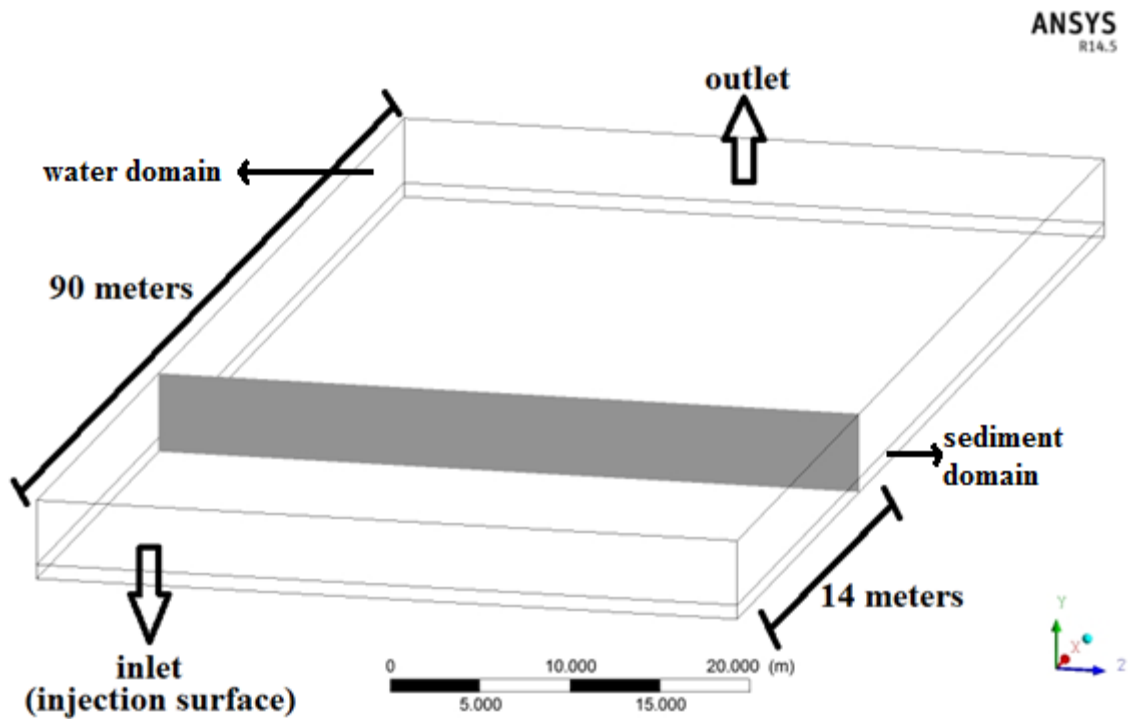


Figure 5.45. Investigated plane in the simplified domain

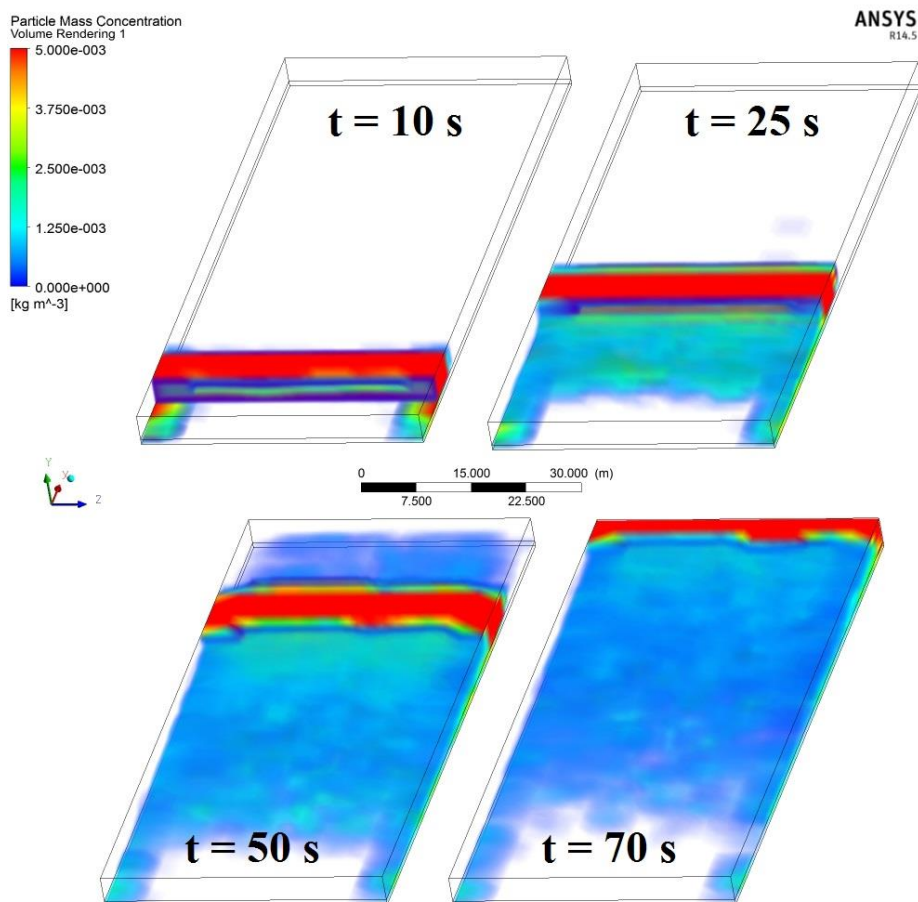


Figure 5.46. Particle motion (median diameter: 0,003 mm; total mass 22,62 kg)

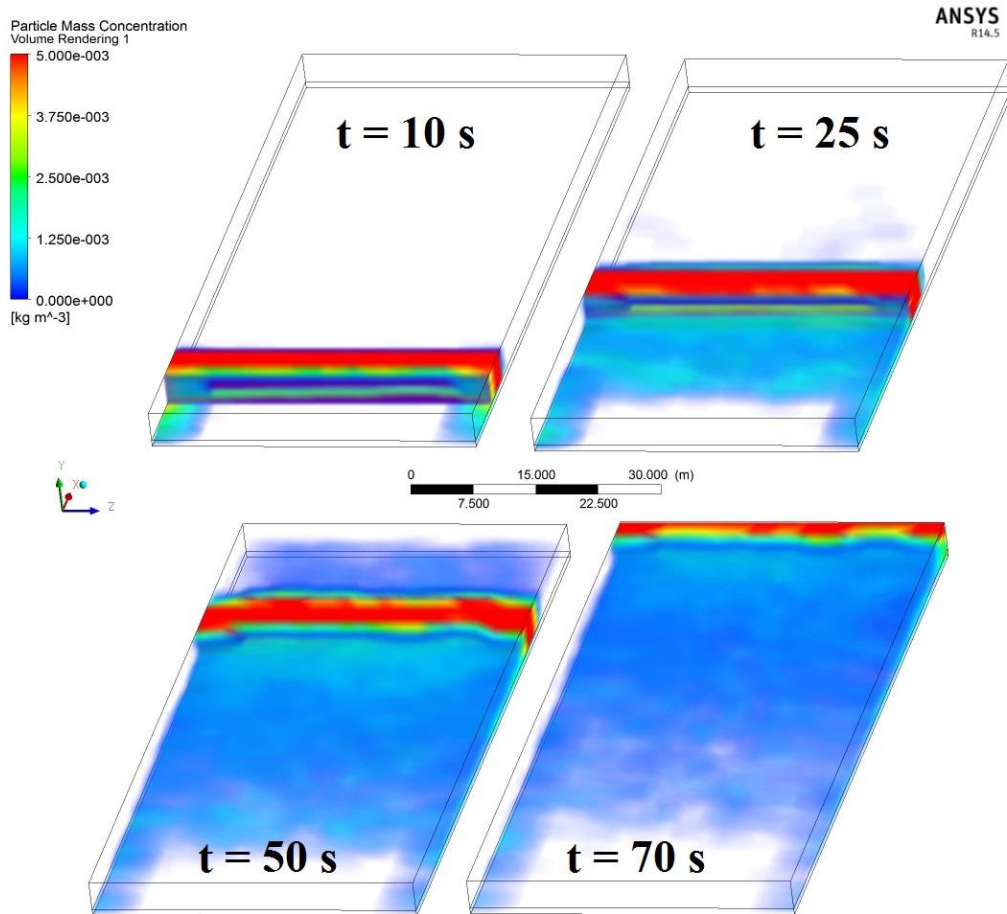


Figure 5.47. Particle motion (median diameter : 0,003 mm ; total mass 11,31 kg)

Figure 5.48 shows settling velocities of suspended sediments on investigated planes in terms of area-weighted average velocity using $k-\epsilon$ turbulence model. Simulation with 0,005 mm median diameter showed maximum settling velocity as expected. Settling particle velocity reached to the maximum value of 1,5 cm/s after 10 s corresponding to the arrival time of sediments to the observation plane. There was a little difference between the maximum settling velocity of the larger particles ($d=0,005$ mm) and the smaller ones ($d=0,003$ mm and $d=0,001$ mm). The maximum absolute settling velocity value was predicted as 1,1 cm/s for suspended sediment having 0,003 mm particle diameter and 0,9 cm/s for suspended sediment having 0,001 mm particle diameter. It can be concluded that median diameter of particle has effective on settling velocity than effect of particle density.

Figure 5.49 shows particle settling velocity on the investigated plane in terms of area-weighted average using $k-\omega$ turbulence model. After 10 s, settling velocities followed a similar trend with the results of $k-\epsilon$ turbulence model. Particle having 0,005

mm median diameter again had maximum settling velocity. The only difference was that maximum settling velocities were greater than settling velocities of k- ϵ turbulence model. Settling particle velocity reached 2,4 cm/s after 10 s for maximum median diameter. This value was obtained as 1,5 cm/s for suspended sediment having 0,003 mm and 0,6 cm/s for suspended sediment having 0,001 mm. It can be concluded that k- ω turbulence model simulated larger settling velocities for the same conditions.

When time it takes to deposit was considered, all diameters gave nearly same results in both k- ϵ (Figure 5.50) and k- ω turbulence models (Figure 5.51). Time it takes to deposit was increasing in negligible quantities when particle diameter was decreasing. The only considerable difference was that suspended sediments having 0,001 mm particle diameter were reached to the end of channel earliest and escaped from outlet surface in k- ω turbulence model. While others reached in 60 s, these smallest particles reached there within 50 s. Figure 5.52 and Figure 5.53 shows the comparison between k- ϵ and k- ω respect to time it takes to deposit.

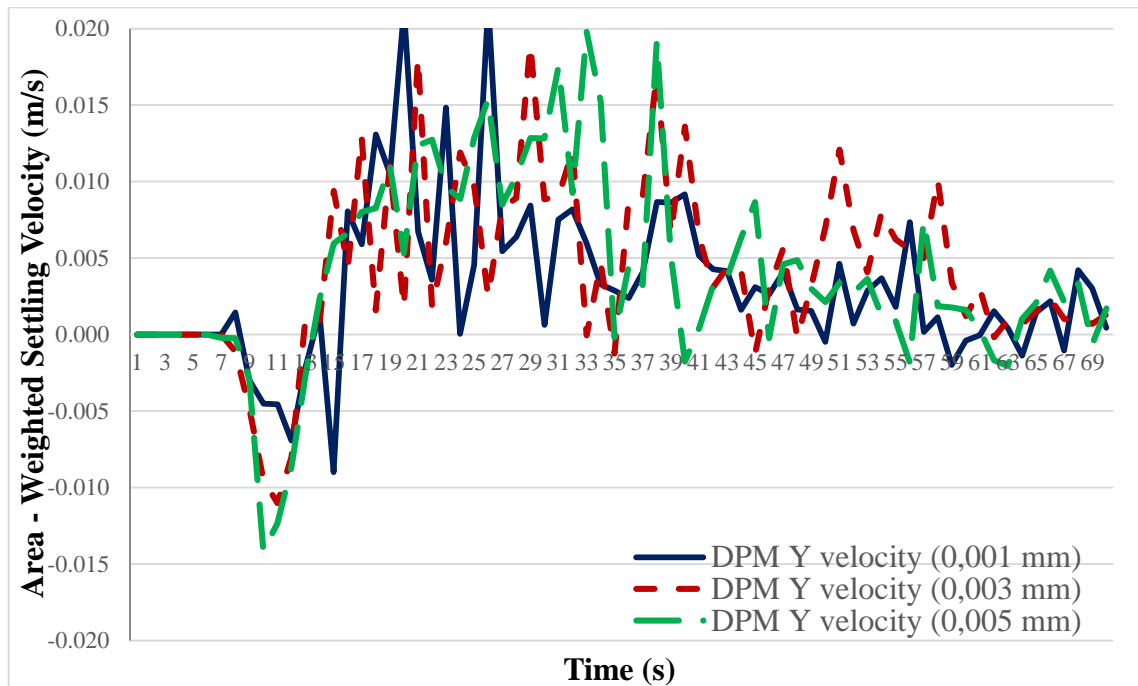


Figure 5.48. Area weighted settling velocity simulated using k- ϵ turbulence model at the selected plane given in Figure 5.45

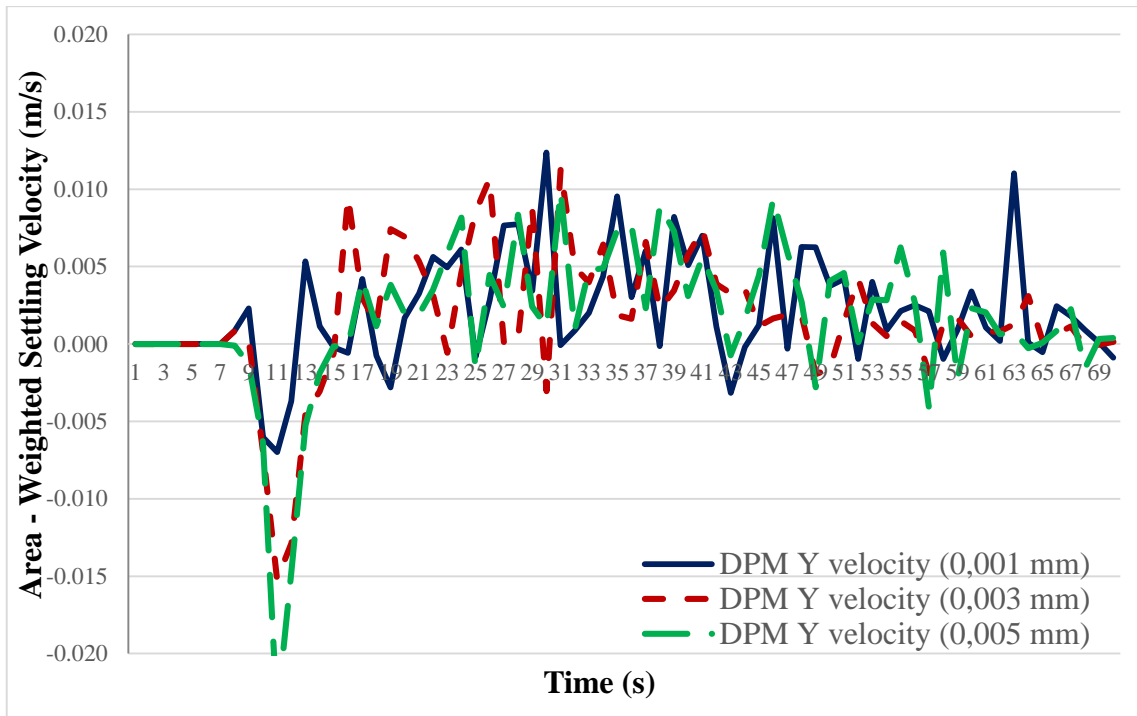


Figure 5.49. Area weighted settling velocity simulated using $k-\omega$ turbulence model at the selected plane given in Figure 5.45

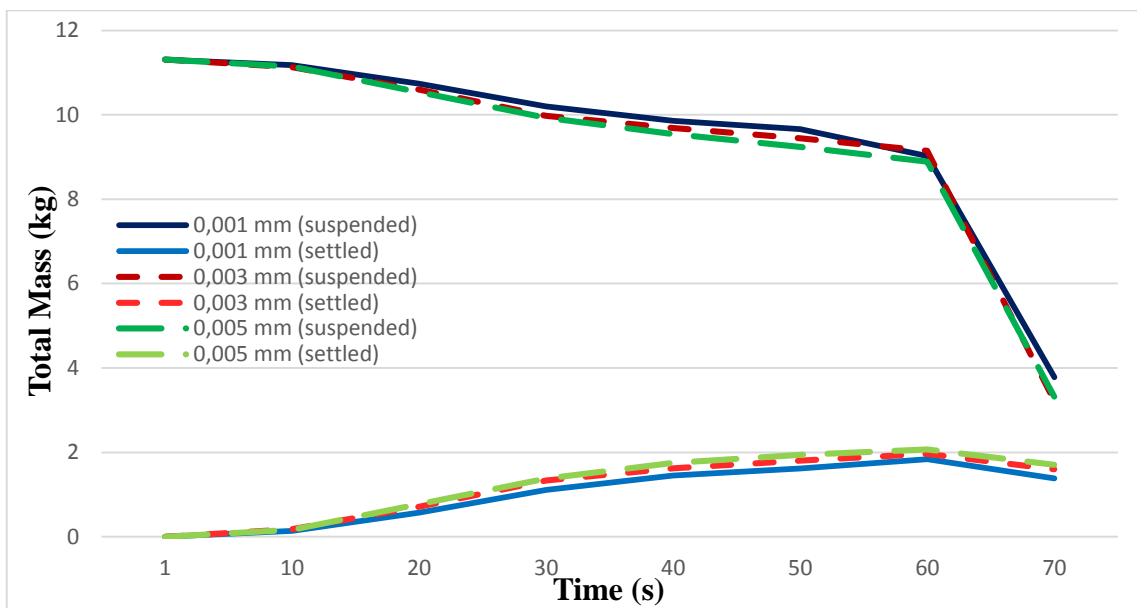


Figure 5.50. Particle settling time simulated using $k-\epsilon$ turbulence model at the all body

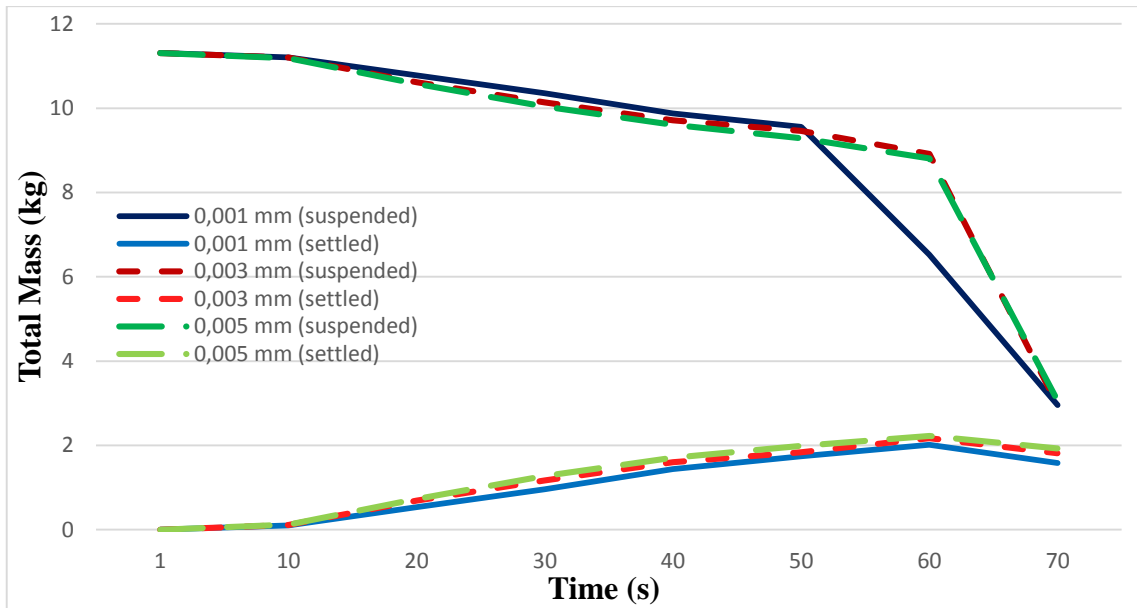


Figure 5.51. Particle settling time simulated using $k-\omega$ turbulence model at the all body

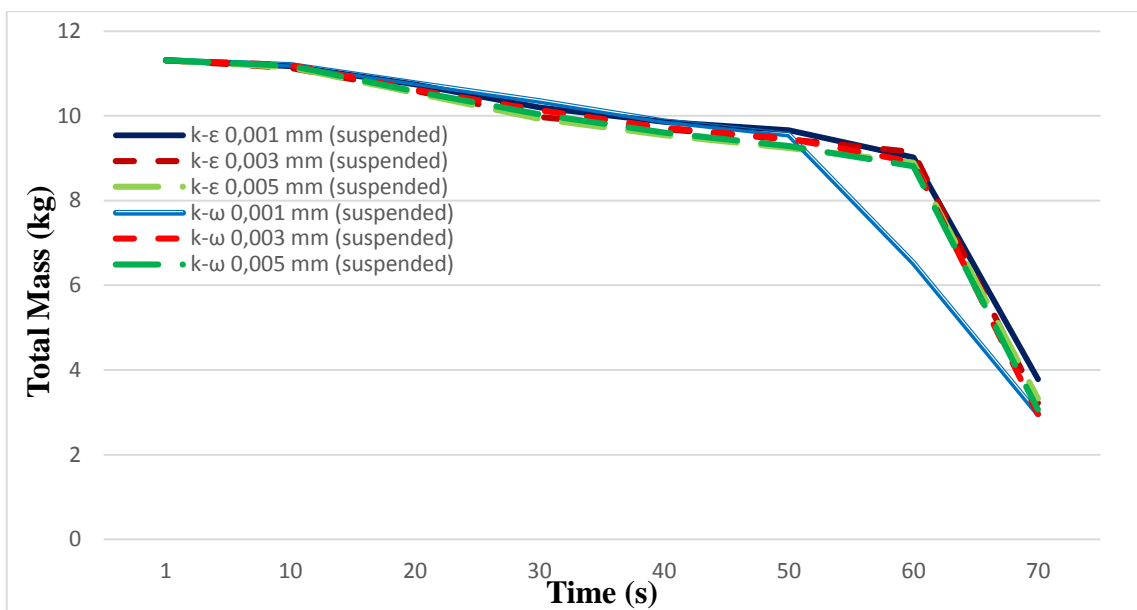


Figure 5.52. Total particle mass settled down respect to time for both $k-\epsilon$ and $k-\omega$ turbulence models

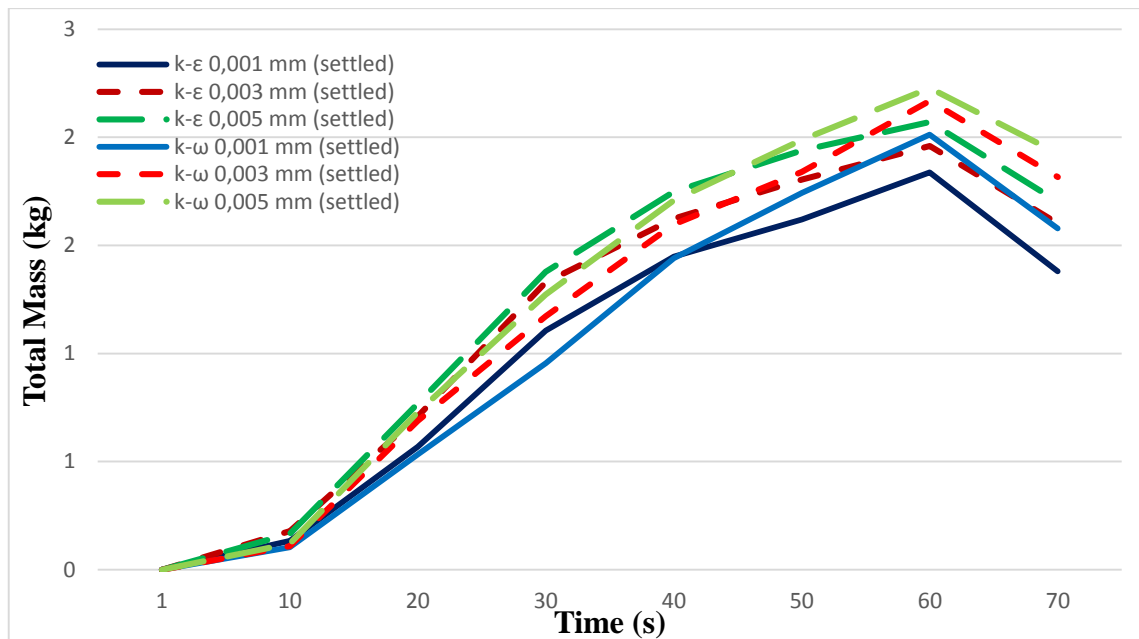


Figure 5.53. Total particle mass accumulated on bottom surface respect to time for both k-ε and k-ω turbulence models

The other comparison was related to the total mass of suspended sediment load. In the first phase, particles having 22,62 kg total mass were injected. Than amount of particles were cut in half in second case. Median diameter was 0,003 mm for both cases and k-ω turbulence model was applied. Figure 5.54 shows settling velocities for both cases on the investigated plane. Results showed that the particles behaved in a similar manner in both cases considering fluctuations and settling velocities. Maximum settling velocity was again 1,5 m/s for particles having 0,003 mm in k-ω turbulence model like previous simulation. Figure 5.55 shows time it takes to deposit for two cases. Suspended sediment particles reached to outlet surface after 60 s in both cases. It can be concluded that sediment concentration does not affect particle motions considerably under the same conditions.

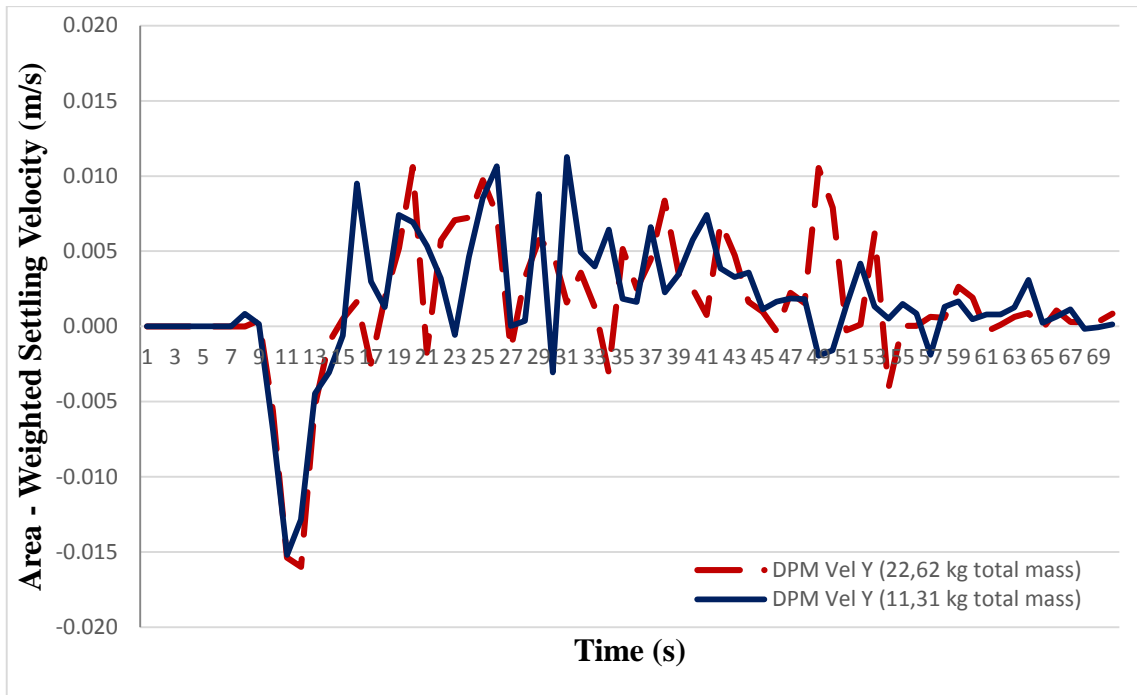


Figure 5.54. Area weighted settling velocity ($d=0.003$ mm) simulated using $k-\omega$ turbulence model at the selected plane given in Figure 5.45 with respect to different concentrations

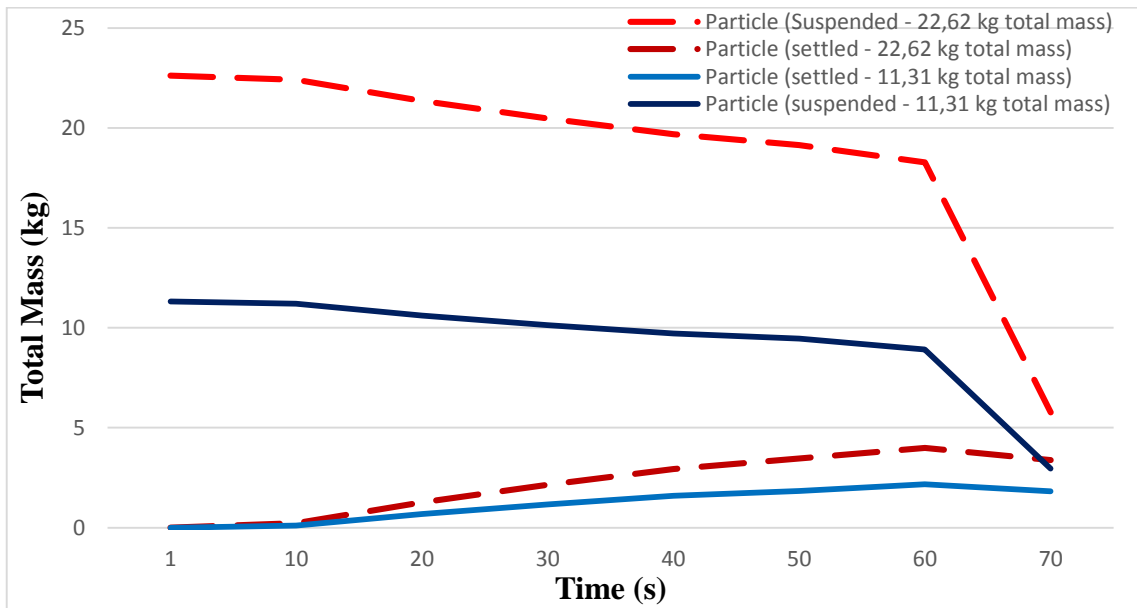


Figure 5.55. Particle settling time ($d=0.003$ mm) simulated using $k-\omega$ turbulence model at the selected plane given in Figure 5.45 with respect to different concentration

5.2.3.2. Particle Motions Considering Eulerian Multiphase DPM Injection with Rossin Rammler Logarithmic distribution vs. Eulerian Multiphase DPM Injection with Uniform Diameter Having 0.003 mm

This section compares the results of DPM injection in a single phase with Rossin Rammler Logarithmic Distribution (RRLD) and DPM injection with Eulerian multiphase with uniform distribution. In the first case, particles having 11,31 kg total mass were injected. Particle distribution for this case is RRLD with 0.003 mm median diameter. For definition of RRLD distribution maximum diameter was selected as 0,005 mm, and minimum diameter was selected as 0.001 mm and the results were compared with the results of uniform distribution having 0.003 mm median diameter. Value of spread parameter used for defining curvature of logarithmic distribution was chosen as 1 and k- ω SST turbulence model was applied.

Figure 5.56 shows the comparison between uniform and RRLD both having 0,003 mm median diameter. Particles spread on bottom surface more regularly with RRLD than uniform distribution. The reason for this was attributed to RRLD having logarithmic distribution with smaller and larger particles than uniform distribution. Smaller particles filled the gaps during the simulation at the bottom surface. For this reason particles can spread more uniformly with RRLD.

Figure 5.57 shows area-weighted vertical velocities on investigated planes for both cases. It was observed that while fluctuations were nearly same, maximum vertical velocities were slightly different. Maximum absolute area-weighted vertical velocity was nearly 1,75 cm/s for RRLD whereas maximum vertical velocity was nearly 1,5 cm/s for the uniform distribution,. It can be concluded that uniform distribution has more particles having small diameters owing to measured field data and value of spread parameter, therefore its maximum absolute area-weighted vertical velocity was less than the other.

Next the comparison on the time it takes to deposit was investigated (Figure 5.58). It was observed that values were nearly same for both as expected. There was a little difference considering time it takes to deposit. Suspended sediment particles having uniform diameter distribution settled down a bit earlier than RRLD.

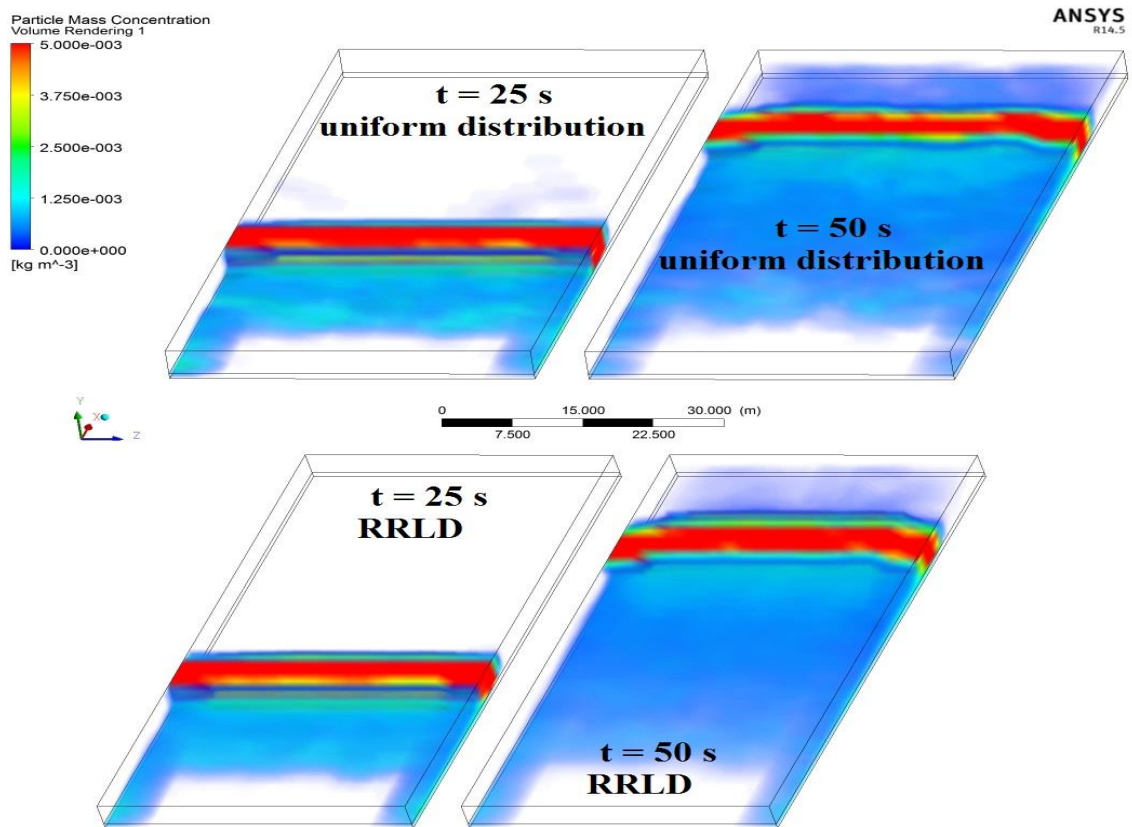


Figure 5.56. Comparison of volume renderings plots of uniform ($d=0.003$ mm) and RRLD applied sediment distributions

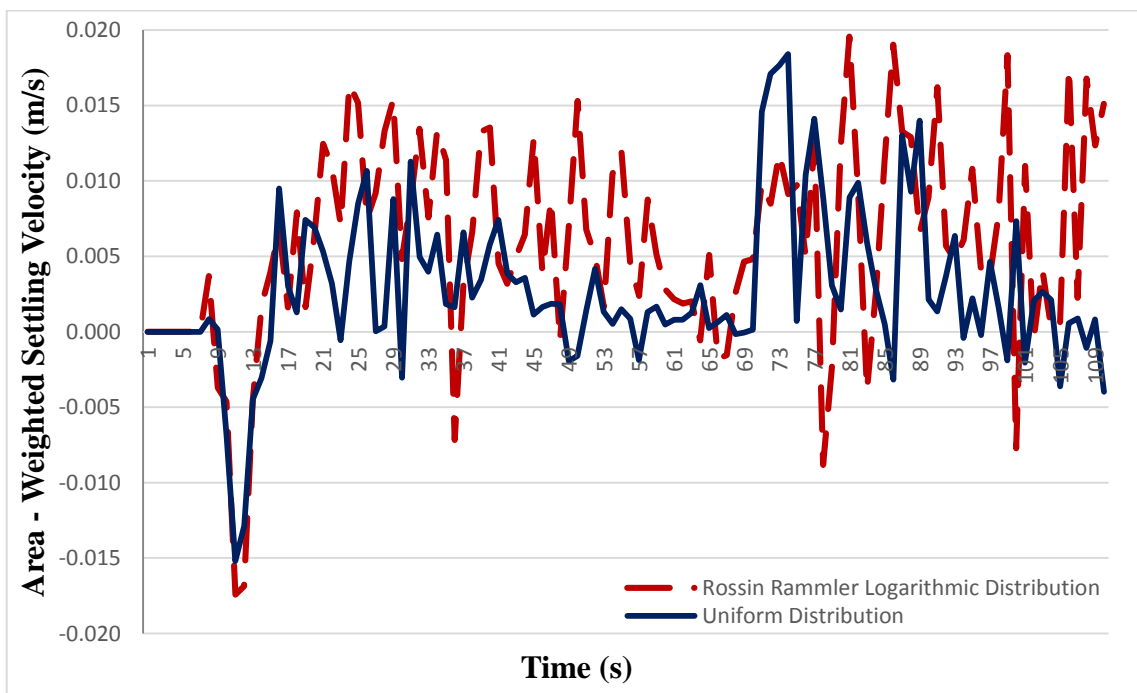


Figure 5.57. Comparison of area-weighted settling velocities for uniform ($d=0,003$ mm) and RRLD distributions at the selected plane given in Figure 5.45

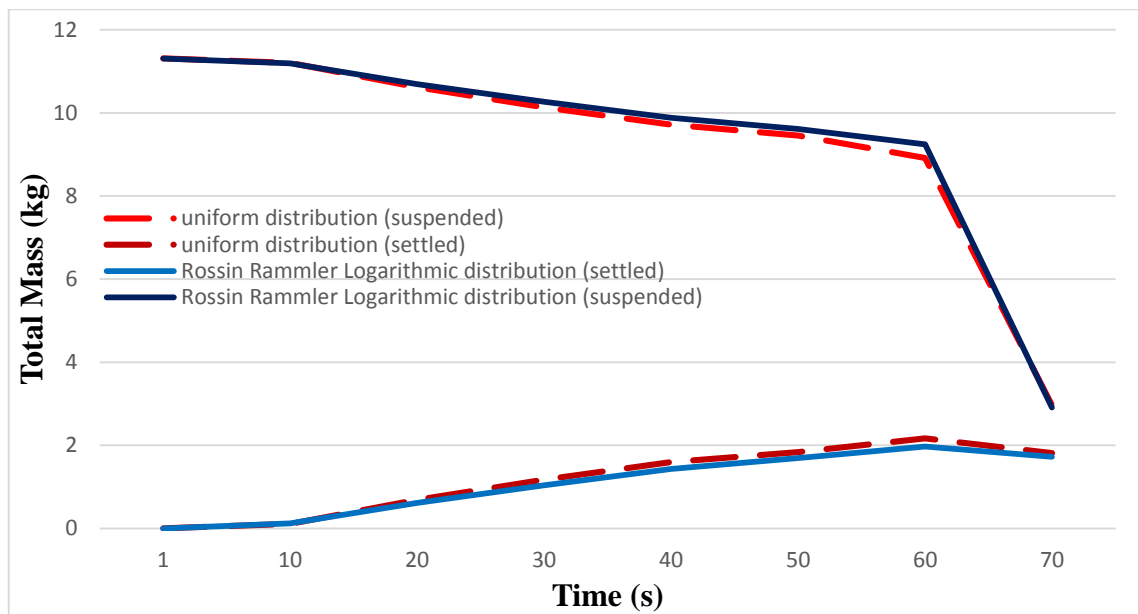


Figure 5.58. Comparison of sedimentation times for uniform ($d=0,003$ mm) and RRLD distributions at the selected plane given in Figure 5.45

5.2.3.3. DPM Injection with Rossin Rammler Logarithmic Distribution Using Eulerian Multiphase versus Single Phase

For the final analysis in this chapter comparison between DPM injection in a single phase with RRLD and DPM injection with multiphase with RRLD was performed. These two cases had same conditions except for the number of phases. Single phase consisted of water only whereas in the multiphase model bed load and water phase were considered via Eulerian approach. Both cases applied RRLD for particle distribution and maximum diameter was selected as 0,005 mm, minimum diameter was selected as 0,001 mm and median diameter was selected as 0,003 mm. Value of spread parameter was again selected as 1.

Figure 5.59 shows volume rendering of suspended sediment transport respect to time. While particles were spreading to all bottom surface with multiphase modeling, all settled particles on bottom surface moved to downstream with single phase modeling within 50 s. There were not any particles left near the inlet surface within 50 s in the case of single phase modeling.

When area-weighted settling velocities were considered, Figure 5.60 showed that values were completely different. Settling velocity became 0 m/s for single phase

modeling after 30 s because particles did not exist near inlet surface. Maximum absolute settling velocity was nearly same and 2 cm/s for both cases.

Figure 5.61 showed that time it takes less time deposit for single phase modeling than for multiphase modeling. While settling of particles were continuing for multiphase modeling within 70 s, this situation did not seem for single phase modeling. Settling of suspended sediments finished and all suspended particles equilibrated after 20 s when single phase modeling was utilized.

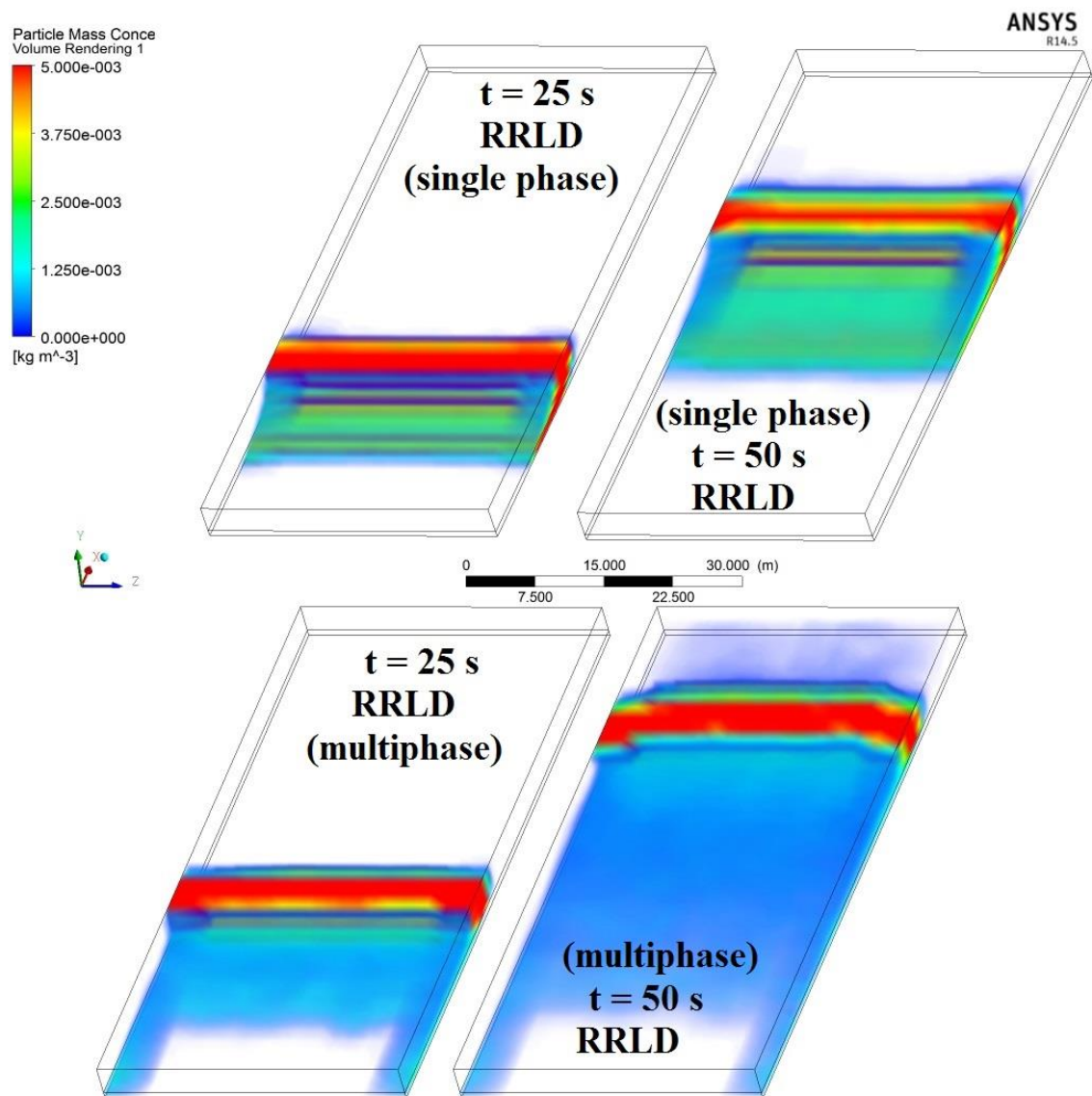


Figure 5.59. Comparison of particle mass concentrations for RRLD sediment distribution considering single and multiphase cases

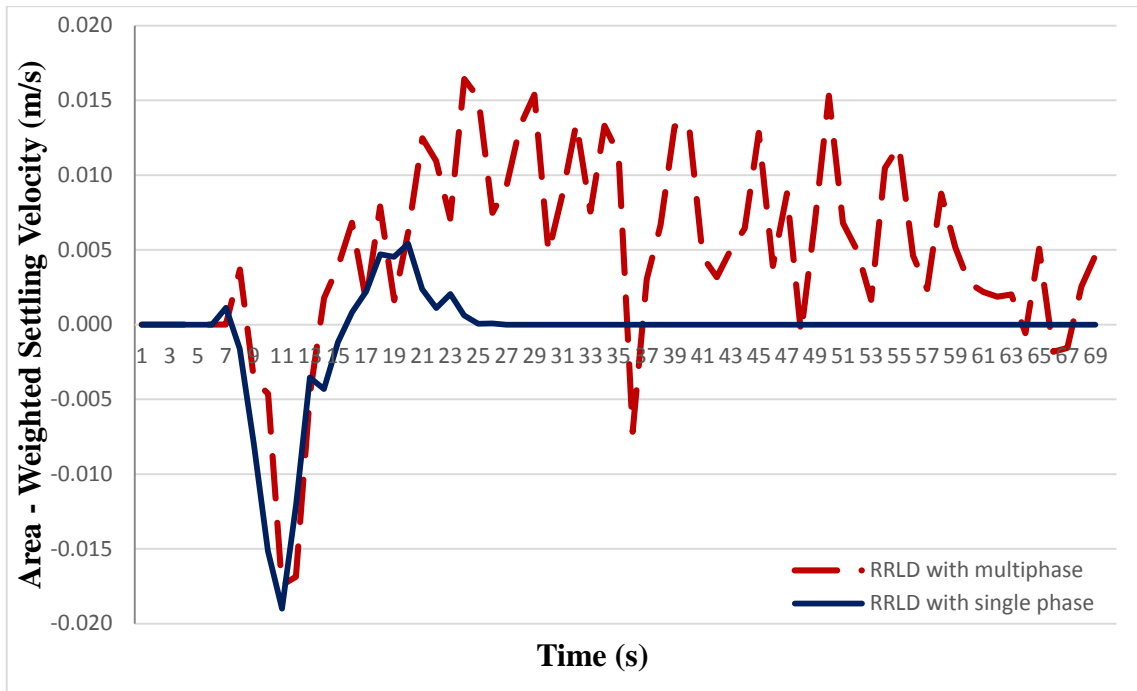


Figure 5.60. Comparison area-weighted settling velocities for RRLD sediment distributions considering single and multiphase cases at the investigated plane.

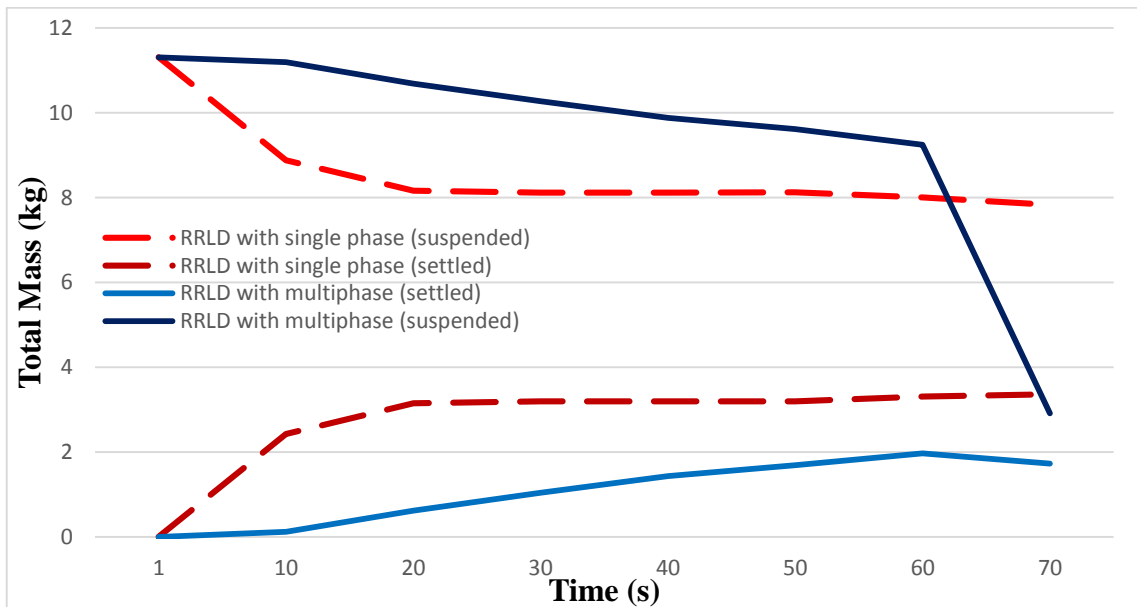


Figure 5.61. Comparison sedimentation times between RRLD with single and multiphase.

CHAPTER 6

MODIFICATION OF RIVER FLOW AND SEDIMENT TRANSPORT MODELING IN CFD

In this chapter, an approach was developed to modify settling velocities in modeling of sediment transport in a river using Stochastic Draw Law under the Fluent solver. For this purpose, “user defined function” was utilized and Drag Force defined in the model was modified accordingly (see Appendix B). There are two methods to define an UDF within the Fluent solver: “Interpreted” and “compile” methods. In this study “compile” method was preferred owing to its beneficial properties. “Interpreted” method remained incapable to define the required modifications

6.1. How to Compile a User Define Function Consisting of Modified Drag Law Codes

To add the “user defined function” created via C language into Fluent solver, “Compiled” method is used. In order to invoke the system C compiler, a Makefile script is activated to build an object code library. The inject code library consists of the native machine language translation of higher-level C source code. Then the shared library has to be loaded into Fluent solver during the runs by a process called “dynamic loading”. This action is initiated by clicking load in the Compiled UDFs dialog box. To summarize, UDFs are compiled from source files using the graphical user interface, in a two-step process. First it is compiled using UDFs dialog box, where a shared library object file from a source file is built. Second, the shared library that was just built into Fluent solver is called [14].

In order to succeed with the solution, Microsoft Visual Studio 2010 Express Edition, Microsoft Windows SDK for Windows 7.1 and .NET Framework 4 must be installed before the process. After installation, “.cas” file involving geometry and mesh of B. Menderes River computation domain was opened via “SDK command prompt” (Figure 6.1). It should be noted that UDF file must be in the same folder with solution

files (.cas). Then 3D as dimension and double precision option were selected in Fluent Launcher page (Figure 6.2).

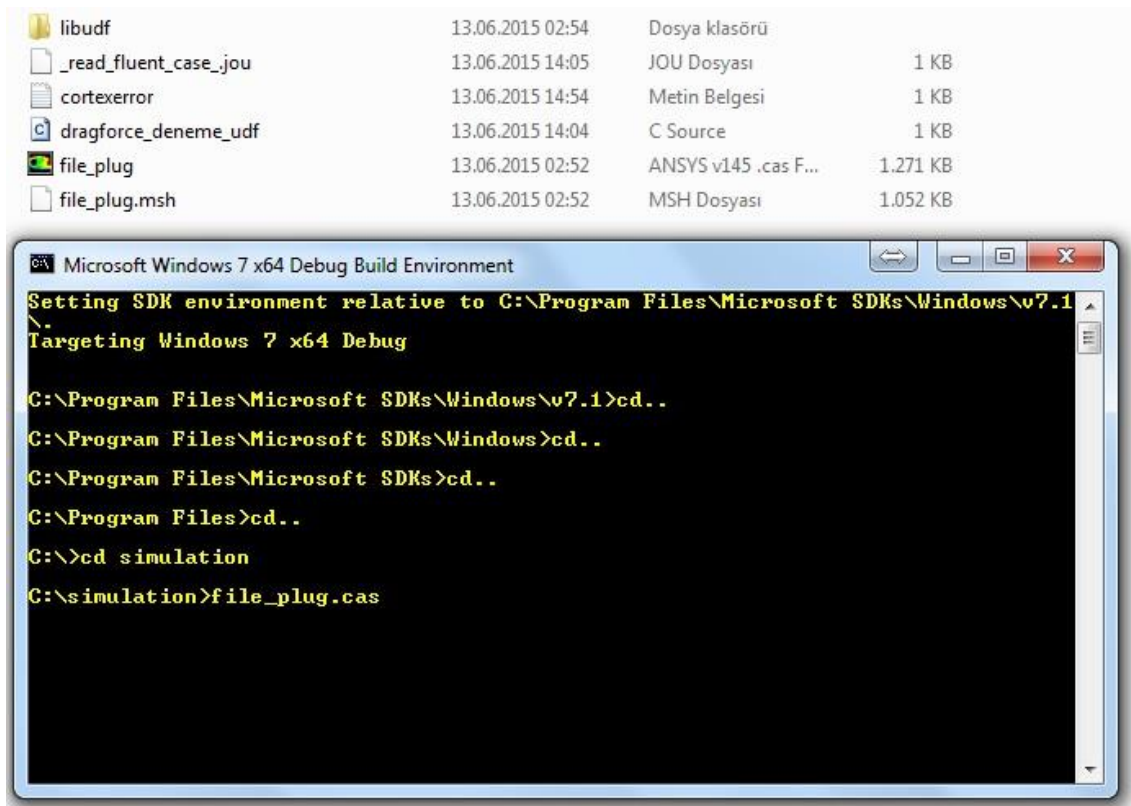


Figure 6.1. SDK Comment prompt page and solution files

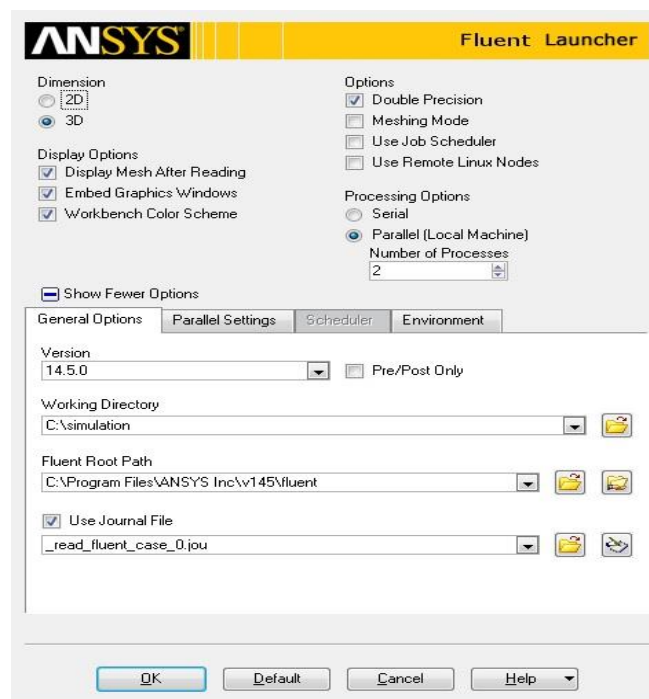


Figure 6.2. Fluent Launcher window

Finally, define / user defined / functions / compiled was clicked. Modified UDF was chosen from “compiled UDFs” page and was built. Library was created automatically and library was loaded. After all these processes, added UDF file defining modified drag law was chosen from main Discrete Phase Model window (Figure 6.3). This provided Fluent to solve fluid (water) and particle (sediment) interaction via modified drag law. After these steps it was possible to compare the settling velocity monitored in the field with the modified settling velocity simulated by the numerical model.

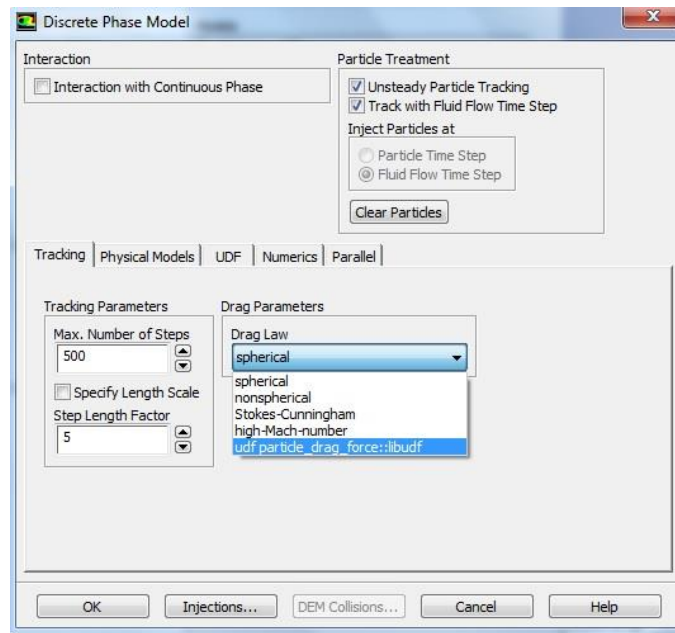


Figure 6.3. Main Discrete Phase Model window

In order to modify UDF file, a sample script defining default drag force obtained from ANSYS Help document. was utilized Default Drag force equation is provided in the manual as;

$$F_D(u - u_p) = \frac{\mu}{\rho_p d_p^2} \times \frac{18C_D Re}{24} (u - u_p) \quad (6.1)$$

Where μ is viscosity of fluid (water), ρ_p is particle density, D_p is particle diameter, C_D is drag coefficient and Re is Reynolds number. In equation (6.1), $[18C_D Re/24]$ was modified (multiplied by the nondimensionalized turbulent kinetic energy (TKE/w^2)) to account for the interaction between particle and fluid. To apply this

modification, macros for particle cell were used and defined. Cell variables were added into UDF file such as flow velocity and turbulence kinetic energy. After general specifications, turbulence characteristics were inserted in drag force equation as a multiplier considering Reynolds number at that time.

6.2. Comparison of Sediments Motions Simulated By Eulerian DPM Method via Modified Drag Law Versus via Non-Modified Drag Law

To investigate the difference in the sediments transport simulated using original drag law versus the modified drag law by the turbulence intensity; the main computation domain defined for the B. Menderes River is utilized. As discussed earlier, the main domain has a total length of 180 m and piers were located in the middle of the water body. K- ω SST is applied as turbulence model and total run time was 110 s for the simulations. Rossin Rammler Logarithmic distribution for sediment size was used for the simulations. Maximum particle diameter was selected as 0,005 mm while minimum and median particle diameters were selected as 0,001 mm and 0,003 mm respectively. Spread parameter was selected as 1 as previously. While one simulation used non-modified drag law to solve particle and fluid interaction, the other used modified drag law to simulate settling velocity considering the turbulence characteristics.

Figure 6.4 and Figure 6.5 show comparison for distribution of particle concentration for two cases. There are some differences between two cases. In modified one, particles were spreading to bottom more uniformly after 110 s. However, in nonmodified model, there was accumulation near right pier (Pier B) at the end of the simulation. This situation can be concluded that the added parameter for drag force affected particle motion during the simulation and increasing turbulence effects near piers led to sediment particle accumulation.

Figure 6.6 shows time it takes to deposit for non-modified and modified simulations. It showed that particles settled down later in the simulation conducted using modified Drag Force than the other simulation. It can be concluded that turbulence intensity added settling velocity rose particle settling time.

Figure 6.7 shows investigated planes. Sediment fall velocities on investigated planes were given for both nonmodified and modified simulations in Figure 6.8 and Figure 6.9. It was shown that distribution of settling velocity was more irregular on plane-73 and plane-130 than settling velocity on plane-180 for both cases. It could be concluded that effects of turbulence generated by piers could cause this irregularity on planes located after piers. On the other hand, in nonmodified system, wave length of fluctuation was wider than other ones. The reason why particles settled down later in the simulation conducted using modified drag law than the other simulation is different wave lengths.

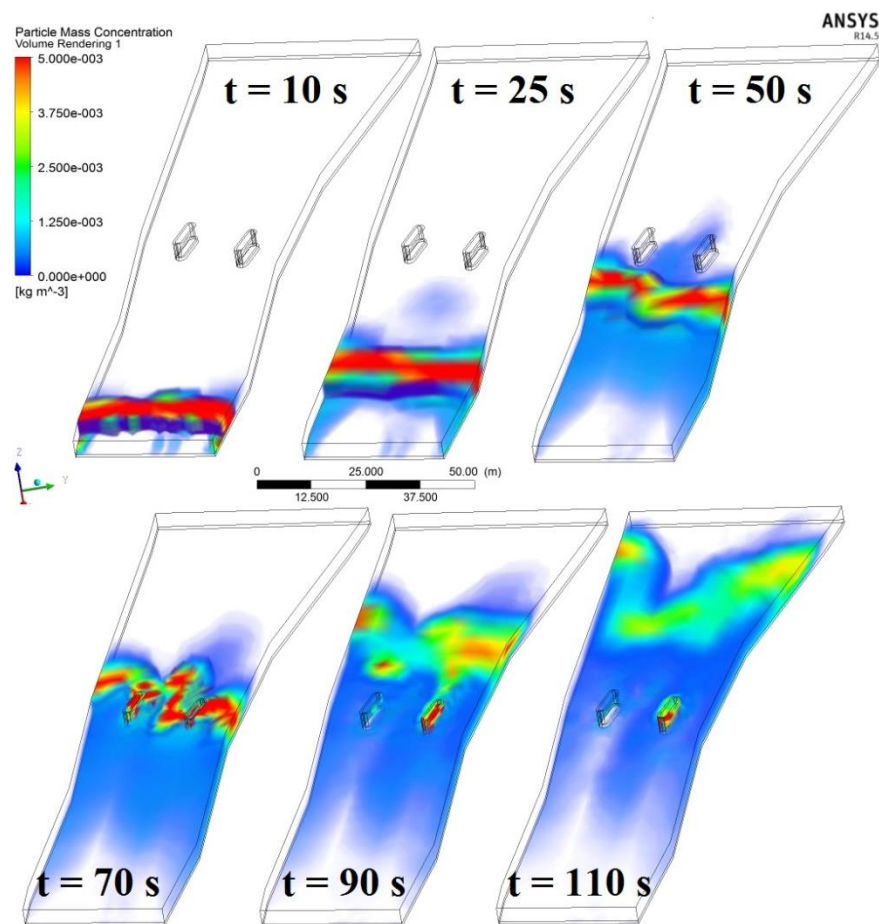


Figure 6.4. Particle mass concentrations simulated using the original drag forces

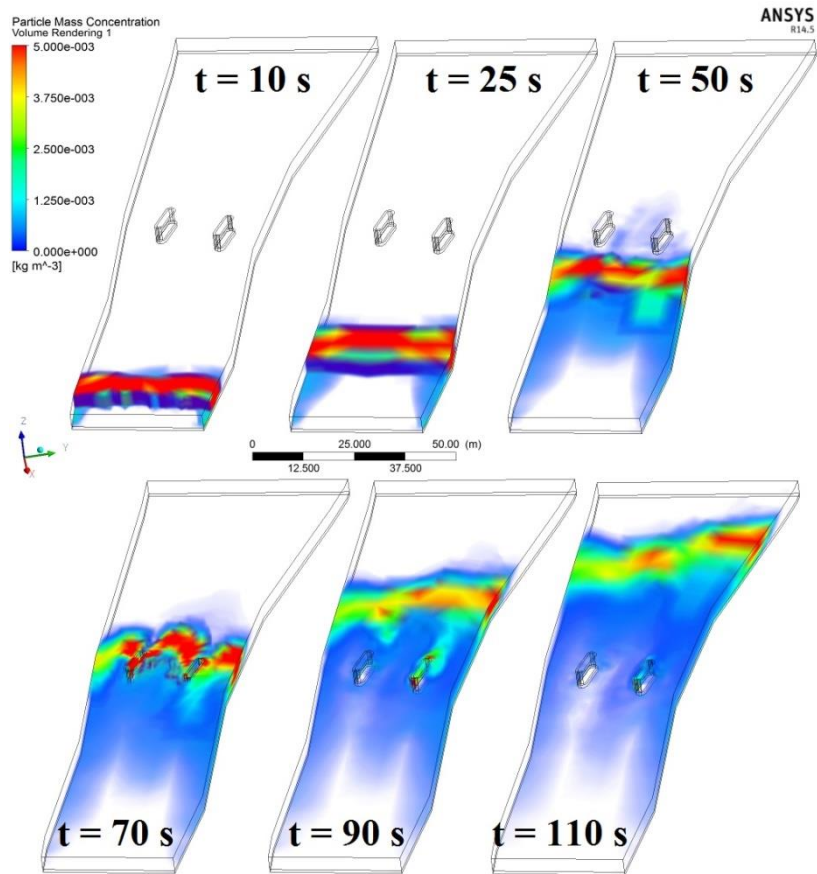


Figure 6.5. Particle mass concentrations simulated using the modified drag forces

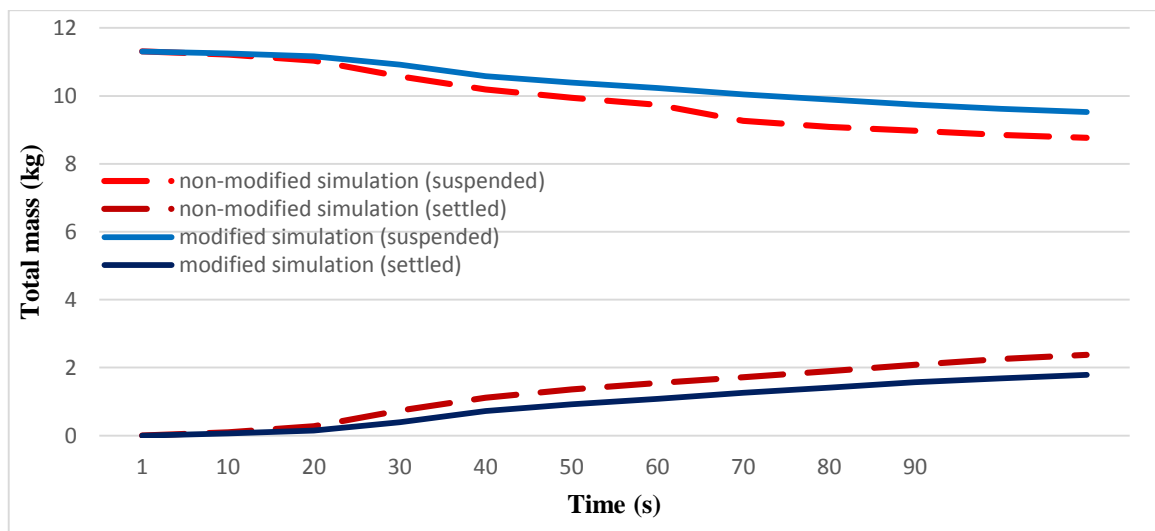


Figure 6.6. Comparison of sedimentation times simulated using the original and modified drag forces.

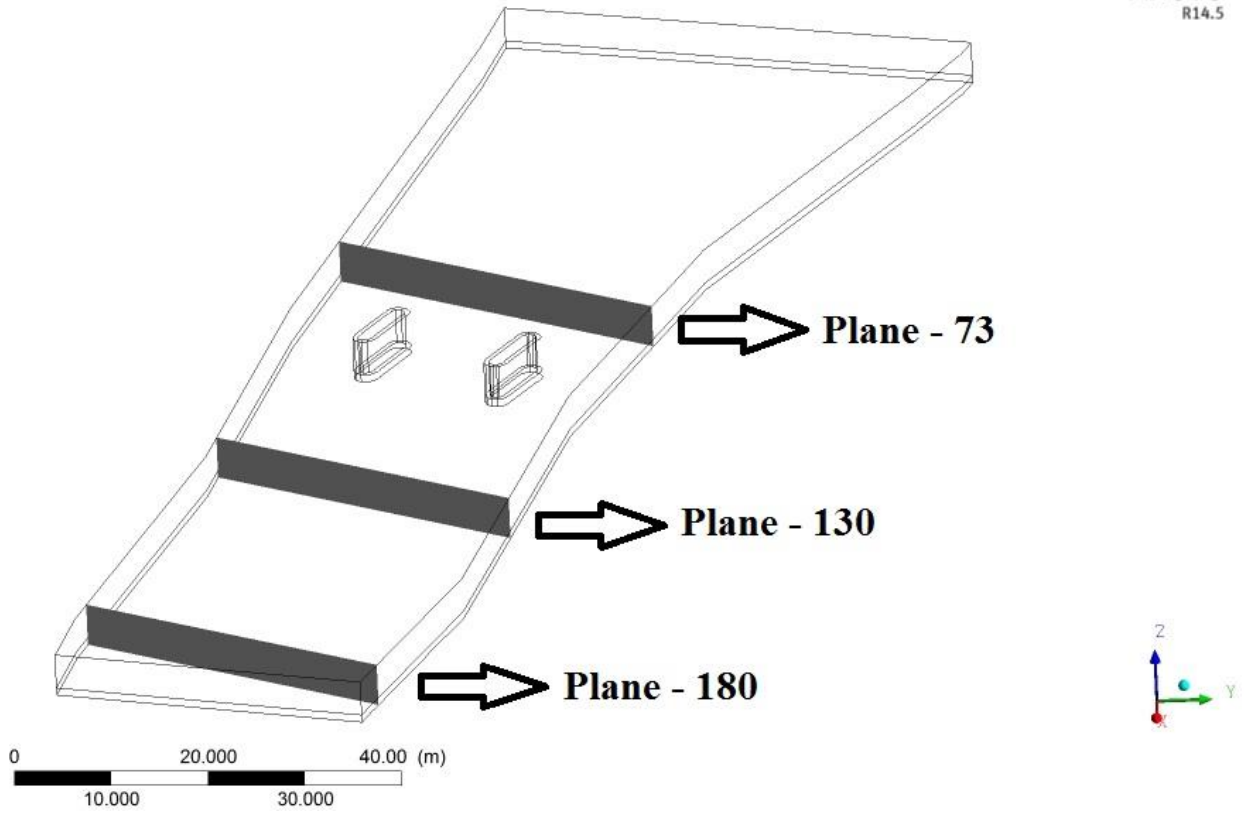


Figure 6.7. Investigated planes for Figure 6.8 and Figure 6.9

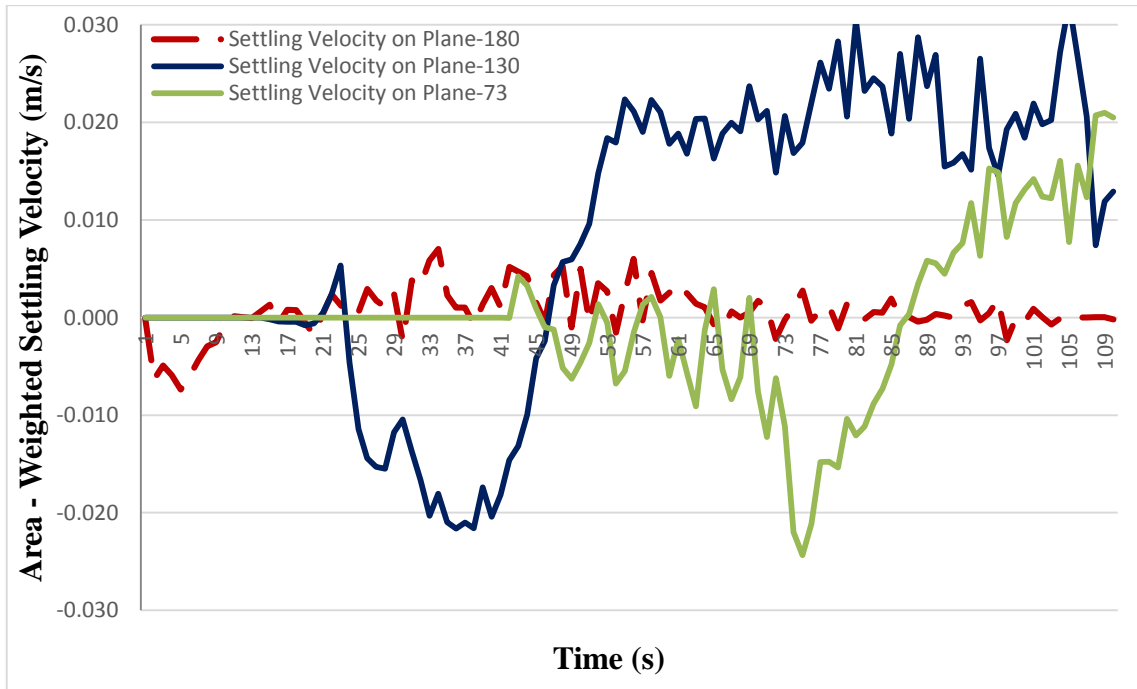


Figure 6.8. Settling Velocities of injected particles on different planes (nonmodified simulation).

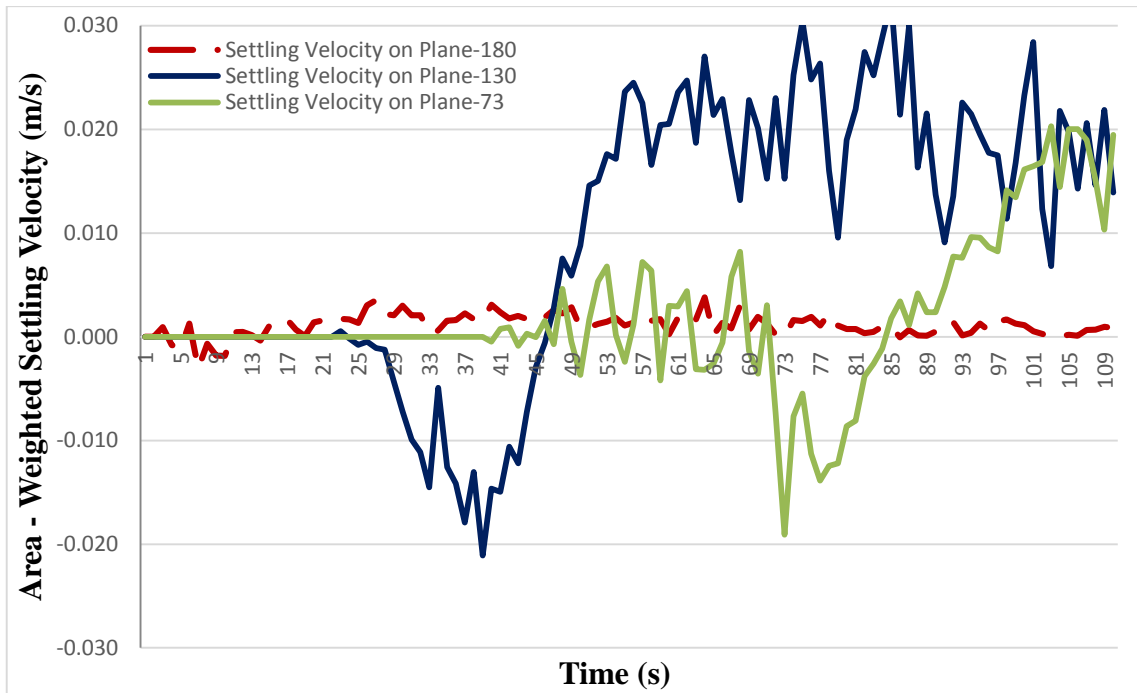


Figure 6.9. Settling Velocities of injected particles on different planes (modified simulation).

CHAPTER 7

DISCUSSION AND CONCLUSIONS

In this study, the turbulence was quantified from direct measurements and an approach for modification of an existing CFD Model for sediment transport in turbulent flow based on these measurements was presented. A novel application of acoustic Doppler instruments for measurement of settling velocities was presented. In the literature, the common approach is estimation of the settling velocities indirectly from the balance of settling and diffusive gradients. This might be true for laminar flow, but field observations indicated that for turbulent flows equation based on this balance is not applicable. For this purpose an approach for modification of particle – fluid interaction in turbulent flow to simulate sediment transport via ANSYS Fluent programme was presented.

Flow and sediment transport in the selected part of B. Menderes River was simulated by a CFD Model – Fluent in this study. In order to understand turbulence effects better, near the region of Old Aydın Bridge was selected as a field site. Under different conditions, nonmodified and modified particle – fluid interactions were investigated. Numerical modeling was conducted at various computational domains to investigate various parameters in detail without spending the extensive computation time (several weeks) required for modeling of the main domain. In order to obtain these goals, field data collected from B. Menderes River was used to investigate and to quantify flow turbulence characteristics. It is possible to predict particle settling velocity by measuring vertical flow velocity via Acoustic Doppler Profiler with the assumption of vertical velocity monitored is equal to the particle velocity (as defined by the operational principle of the ADCP). By utilizing this information, hydrometer analysis obtained from an earlier study was used to define suspended sedimentation.

In the first stage of the numerical modeling, the effects of applying different turbulence models were investigated in a simple water column. For these simulations $k-\epsilon$, $k-\omega$ and Reynolds turbulence models were utilized. The model was applied to the water column in front of the water intake and initial/boundary conditions were selected based on measurements made in the Tahtalı Reservoir, İzmir. Results showed that $k-\omega$ had greater turbulence kinetic energy because $k-\omega$ does not use wall function during

simulation. Although different wall treatment functions did not have significant effects on the flow velocities, nonequilibrium wall treatment gave lower turbulent kinetic energy values than standard and two layer wall treatments outside the intake region. More dissipation in turbulent kinetic energy predicted by the nonequilibrium wall functions was related to the logarithmic velocity profile modified to include pressure gradient. After all, $k-\omega$ was used in main geometry to understand effect of turbulence better and it was understood that $k-\omega$ and $k-\varepsilon$ could be best models to simulate a model for this purpose.

In the second step, the main domain of B. Menderes River was simulated with only water phase to understand effects of turbulence models. Results were discussed for near the piers of Old Aydın Bridge. $k-\omega$ was again found to be a better choice to simulate near piers in turbulence flow and high turbulence intensity.

In the third step, the simplified geometry of the main domain was used to simulate interaction between particles and water. Different conditions were analyzed in this part. Firstly, 11,31 kg particles injected from inlet surface at the beginning of simulation for $k-\varepsilon$ and $k-\omega$ turbulence models to understand particle motions. Results showed that particle having maximum diameter settled down a bit earlier for both cases ($k-\varepsilon$ and $k-\omega$) and particle having minimum diameter settled down later and reached outlet surface and escaped earlier for both cases. Moreover, although particles had same diameter, $k-\omega$ provided particle to settle down a bit later than $k-\varepsilon$. Next, the effect of injection of different concentration to the model was investigated. 22,62 kg and 11,31 kg were injected under same conditions for this purpose and results showed that particles settled in a similar way at both cases. All these simulations were conducted considering uniform particle distributions having $d=0.001$ mm, $d=0.003$ mm and $d=0.005$ mm as median diameters. Following this section, particle distribution was defined by a logarithmic distribution: Rosin Rammler Logarithmic Distribution (RRLD) was used. In this distribution median diameter was chosen as 0,003 mm to simulate suspended sediment load in B. Menderes River better considering sediment properties collected from the site [25]. The results were compared with uniform distribution having 0.003 mm particle diameter. Results showed that particle motion was nearly same for both cases as expected. The only difference was that fluctuation on bottom surface was diminished for RRLD. Particles spread better on the bottom surface when RRLD was considered.

In the fourth step, multiphase and single phase conditions were compared considering RRLD. Results showed that while particles were spreading to all bottom surface with multiphase modeling, all settled particles on bottom surface moved to downstream with single phase modeling after 50 s later from the beginning. There was not any particle near inlet surface after 50 s for single phase modeling. Also it was seen that particle settling velocity was greater in single phase. Multiphase model gave truer and more realistic results than other model since it has the capability of a wider range of suspended sediment distribution. Therefore multiphase model was used to simulate main geometry for accuracy.

In the fifth and last step, drag force on particle was modified via “user defined function”. In order to define modified UDF “compile” method was used instead of “interpreted” method to define correctly “thread*t” line taking part in modified UDF code. After modifying and defining UDF, modified and non-modified cases were simulated and compared. While particles were spreading to bottom nonuniformly with non-modified drag force, particles were spreading more uniformly with modified drag force. Owing to modification of drag force and defining increased turbulence effects near piers better, there was less sediment accumulation near Pier B in modified simulation as well.

To sum up, turbulent flow is a really complex natural event and it may cause different results on particle motion. The methodology needs to be further improved for different turbulent conditions to understand interaction between particle and flow. However this study presents researchers a way to change particle – fluid interaction by modifying drag law and this can be useful for further studies.

REFERENCES

1. Kesteren, W.A.V., Introduction To The Physics Of Cohesive Sediment In The Marine Environment. 2004.
2. Mantovanelli, A. and Ridd, P.V. Devices to measure settling velocities of cohesive sediment aggregates: A review of the in situ technology. *Journal of Sea Research*, 2006. **56**(3): p. 199-226.
3. Guo, L., et al., An experimental study of low concentration sludge settling velocity under turbulent condition. *Water Res*, 2009. **43**(9): p. 2383-90.
4. Noguchi, K. and I. Nezu, Particle–turbulence interaction and local particle concentration in sediment-laden open-channel flows. *Journal of Hydro-environment Research*, 2009. **3**(2): p. 54-68.
5. Ha, H.K. and Maa, J.P.-Y. Effects of suspended sediment concentration and turbulence on settling velocity of cohesive sediment. *Geosciences Journal*, 2010. **14**(2): p. 163-171.
6. Thinglas, T. and. Kaushal, D.R Comparison of two- and three-dimensional modeling of invert trap for sewer solid management. *Particuology*, 2008. **6**(3): p. 176-184.
7. Tarpagkou, R. and Pantokratoras, A. CFD methodology for sedimentation tanks: The effect of secondary phase on fluid phase using DPM coupled calculations. *Applied Mathematical Modelling*, 2013. **37**(5): p. 3478-3494.
8. Yan, H., et al., Computational fluid dynamics modelling of flow and particulate contaminants sedimentation in an urban stormwater detention and settling basin. *Environ Sci Pollut Res Int*, 2014. **21**(8): p. 5347-56.
9. Graf, W.H. and M.S. Altınakar, *Transport of Sediment*.
10. Bombar, G. and Albayrak, İ., *Investigation Of Turbulent Flow Properties And Coherent Flow Structures*. 2008.

11. Gruber, K., Sediment transport in open channel flows - Experimental investigation and numerical simulation of local scour development downstream of a weir. 2012, Institute for Theoretical Physics.
12. ANSYS, Introduction to ANSYS FLUENT Customer Training Material Lecture 6. 2010.
13. Gürdamar, E., Adaptation Of Turbulence Models. 2005, Middle East Technical University.
14. ANSYS, ANSYS v14.5 Help. 2012.
15. Çelik, İ., Introductory Turbulence Modeling, in Mechanical & Aerospace Engineering Dept. 1999, West Virginia University.
16. Spalart, P.R. and Almaras, S.R., A One-Equation Turbulence Model for Aerodynamic Flows. 1992. AIAA Paper 92-0439.
17. Wilcox, D.C., Turbulence Modeling for CFD. 1993.
18. Wilcox, D.C., Turbulence Modeling for CFD. 2006, DCW Industries, Inc.
19. Menter, F.R., Two-equation eddy-viscosity turbulence models for engineering applications. AIAA Journal, 1994. **32**(8): p. 1598-1605.
20. Launder, B.E., Reece, G. J. and Rodi, W., Progress in the Development of a Reynolds-Stress Turbulent Closure. Journal of Fluid Mechanics, 1975. **68**(3): p. 537-566.
21. You, D. and Moin, P., A Dynamic Global-Coefficient Subgrid-Scale Eddy-Viscosity Model For Large-Eddy Simulation In Complex Geometries. Physics of Fluids, 2007. **19**(6)(065110, 2007).
22. Zhao, B., C. Chen, and A.C.K. Lai, Lagrangian Stochastic Particle Tracking: Further Discussion. Aerosol Science and Technology, 2011. **45**(8): p. 901-902.
23. Fluent, Applied Computational Fluid Dynamics (multiphase flow). 2002, Fluent Inc.

24. Wikipedia. Büyük Menderes River. Available from: http://en.wikipedia.org/wiki/Büyük_Menderes_River.
25. Elci, S., R. Aydin, and P.A. Work, Estimation of suspended sediment concentration in rivers using acoustic methods. Environ Monit Assess, 2009. **159**(1-4): p. 255-65.
26. Elci.S., An Approach for Estimating Settling Velocity in Turbulent Flows. Proceedings of the 36th IAHR World Congress, The Hague, 2015.
27. Epler, J., Tidal Resource Characterization from Acoustic Doppler Current Profilers, in Mechanical Engineering. 2010, University of Washington.
28. ANSYS, Tutorial Guide. 2012.

APPENDIX A

UDF (HYDROGRAPH)

```
#include "udf.h"

real Dt1=249.99;
real Dt2=250.01;
real Tevapfz1=0.257;
real Tevapfz2=0.257;
real Tevapfz3=1.0474;
real A=249.99;
real B=0.257;
real c_time=0.0;
real aralik=0.0;

DEFINE_EXECUTE_AT_END(my_execute_at_end)

{
c_time=CURRENT_TIME;
    if(c_time<Dt1)
    {
        A=0;
        B=Tevapfz1;
        aralik=1.0;
    }
if((c_time<(Dt1+Dt2))&&(c_time>=Dt1))
{
    A=(Tevapfz2-Tevapfz3)/(-Dt2);
    B=(Tevapfz3*Dt1-Tevapfz2*(Dt1+Dt2))/(-Dt2);
    aralik=2.0;
}

printf("VELOCITY=%f\n\n", (A*CURRENT_TIME+B));
```



```
        printf("ARALIK=%f\n\n", aralik);
    }
DEFINE_PROFILE(vel_triangular_aydin, thread, index)
{
    real x[ND_ND];
    real y;
    face_t f;
        begin_f_loop(f, thread)
            {
                F_CENTROID(x,f,thread);
                F_PROFILE(f, thread, index) = A*c_time+B;
            }
        end_f_loop(f, thread)
    }
}
```

APPENDIX B

UDF (DEFINED DRAG FORCE)

```
#include "udf.h"
DEFINE_DPM_DRAG(particle_drag_force, Re, p)
{
    real drag_force, u, v, w, TKE;
    Thread*t = P_CELL_THREAD(p);
    cell_t c = P_CELL(p);
    u = C_U(c, t);
    v = C_V(c, t);
    w = C_W(c, t);
    TKE = C_K(c,t);
    if (Re < 0.01)
    {
        drag_force=18.0+(TKE/(0.00000001+w*w));
        return (drag_force);
    }
    else if (Re < 20.0)
    {
        w = log10(Re);
        drag_force = 18.0 + (TKE/(0.00000001+w*w))*2.367*pow(Re,0.82-0.05*w);
        return (drag_force);
    }
    else
    /* Note: suggested valid range 20 < Re < 260 */
    {
        drag_force = 18.0 + (TKE/(0.00000001+w*w))*3.483*pow(Re,0.6305);
        return (drag_force);
    }
}
```